



A novel approach for generation of power by harvesting microwave from the ambient environment

B. Paulchamy, J. Jaya & A. Venkatesh

To cite this article: B. Paulchamy, J. Jaya & A. Venkatesh (2016) A novel approach for generation of power by harvesting microwave from the ambient environment, Journal of Microwave Power and Electromagnetic Energy, 50:1, 19-34

To link to this article: <http://dx.doi.org/10.1080/08327823.2016.1157311>



Published online: 03 May 2016.



Submit your article to this journal [↗](#)



Article views: 15



View related articles [↗](#)



RESEARCH ARTICLE

A novel approach for generation of power by harvesting microwave from the ambient environment

B. Paulchamy^a, J. Jaya^b and A. Venkatesh^a

^aECE, Hindustan Institute of Technology, Coimbatore, India; ^bPrincipal, Akshaya College of Engineering & Technology, Coimbatore, India

ABSTRACT

To generate power by harvesting microwave from the ambient environment, this paper demonstrates the harvester operation and microwave signal strength analysis. The survey of signal was undertaken in urban and semi-urban regions, and the microwave signals available in space are digital television (DTV), GSM900, GSM1800 and 3G. Using the result of the survey, the harvester circuit was designed; the harvester circuit comprised mainly four parts, namely antenna, matching network, rectification and storage element. These four harvesters are generally known as rectenna. In order to capture the signal, at first, antenna was designed at printed circuit board (PCB) where the efficiency is low; therefore, the next method designed was patch-type antenna, which gives the efficiency greater than the PCB-type antenna. Finally, we got 3.3 V output voltage, which helps to charge the mobile phones without the need of wired process.

ARTICLE HISTORY

Received 27 April 2015
Accepted 30 July 2015

KEYWORDS

Antenna; matching network; rectification; storage element; PMM (power management module); MPPT (maximum power point tracking system)

1. Introduction

Wireless multimedia systems are receiving increasing research and application interests. But improvements are still required to provide higher data-rate links, for instance, the transmission of video signals. Therefore, ultra-wideband (UWB) communication systems are currently under investigation and the design of a compact wideband antenna is very essential (Pinuela et al. 2013). To overcome the inherently narrow bandwidth of microstrip antennas, various techniques have been developed to cover the entire UWB bandwidth, such as L-/F-shaped probe to feed the patch, triangular patch, U-/V-slot monopoles, among others. The use of antenna to collect the energy that is being radiated at several frequencies which is much more effective to harvest the energy of several services at the same time than collecting only one service at a time, so the idea of an UWB antenna for harvesting energy is entirely feasible. Energy harvesting is the process by which energy from different sources is captured and stored. The focus is mainly based on incident low-power density designing, measuring and testing. A rectenna is used to harvest electric energy from the radiofrequency (RF) signals that have been radiated by public communications

systems. For almost 50 years, far-field RF technology has been used to remotely power systems from relatively large unmanned helicopters to very small smart dust sensors and contact lenses that measure eye pressure (Pi & Khan 2011; Rappaport et al. 2011; Yang et al. 2011). With all these systems, a dedicated RF source is used, where the operator may have control over the effective isotropically radiated power (i.e. both transmit power and antenna characteristics), beam pointing and polarization of the RF source, ensuring optimal line-of-sight operation between the source transmitter and harvesting receiver.

Wong et al. (2001) proposed novel compact microstrip antenna designs with a slotted ground plane. By embedding meandering slots or some suitable narrow slots in the antenna ground plane, it is observed that the resonant frequency of the microstrip antenna is significantly lowered, which can lead to a large antenna size reduction for a fixed frequency operation. In addition, enhanced impedance bandwidth and antenna gain are also observed for the proposed antenna, compared to corresponding regular microstrip antennas.

Chen et al. (2003) proposed the design of a novel dual-polarized stacked microstrip antenna fed by microstrip line that operates within ISM-band (2.402–2.4835 GHz) for Bluetooth applications. The design was carried out using a square patch which was fed diagonally by a microstrip line. Another square patch with a substrate was stacked above the corner-fed patch. The input impedance was measured by HP8753D network analyser.

Monti and Congedo (2012) proposed a device that has T-shaped monopole with a coplanar waveguide feeding line as receiving antenna and a five-stage voltage multiplier as rectifier. Experimental results demonstrate an RF to direct current conversion efficiency about 54% with an input power density of $80 \mu\text{W}/\text{cm}^2$, and the efficiency is lower compared to patch antenna.

2. Proposed methodology

2.1. Signal survey

In order to quantify input RF power density levels present in a typical urban and a semi-urban environment, a city-wide RF spectral survey within the ultrahigh-frequency (0.3–3 GHz) part of the frequency spectrum was conducted within India. A number of city-wide RF spectral surveys have previously been conducted, but, in general, only a few samples were taken, giving little insight into semi-urban environments.

Other surveys compare their measurements relative to the distance from the nearest transmission (Salter et al. 2009). In a semi-urban environment, this may not provide enough information about the RF spectrum since there is likely to be local geographical variations in base-station density and propagation characteristics (e.g. multipath effects and diffraction around and attenuation through buildings).

Each station on the Indian underground network was used as a survey point to provide a robust data-set for representing India in terms of geographical distribution and population density, having a combination of urban and semi-urban characteristics.

2.2. Methodology

Mobile phone usage varies during the daytime, and hence ambient RF energy in their bands is expected to be time dependent, with more energy available during the daytime

than at night time. Therefore, in order to be able to make fair comparisons between locations, measurements were taken between 10:00 am and 3:00 pm on weekdays over a period of one month. Electric field strength was measured between 0.3 and 2.5 GHz using an Agilent N9912A Field Fox RF analyser with a calibrated omnidirectional antenna. It is important to note that the spectral measurements were undertaken during the analogue to digital switch-over period in the UK, and so the measurements for digital television (DTV) may represent an underestimate of the present RF power levels are measured and the switch-over is complete (Angelopoulos et al. 2006; Sadasiva Rao & Raju 2011).

2.3. Spectrum analysis

The input RF power density is then calculated from the electric field strength measurement. The input RF power density is measured outside the underground station, where the spectral bands for DTV, GSM900, GSM1800, 3G and Wi-Fi can be clearly identified. A well-designed rectenna should ideally be capable of harvesting energy across an entire band, and thus it is important to calculate the total band power. The banded input RF power density is calculated by summing up all the spectral peaks across the band. These levels provide a snapshot of source availability at the time and location of the measurement. Moreover, they are used as a harvester design starting point since the power density at each band defines the input impedance of a rectenna. The survey is shown in Figure 1.

The RF power levels across all Indian underground stations for the banded input RF power density measurements. It can be seen that all base-station transmit levels are between one and three orders of magnitude greater than the associated maximum transmission levels. For this reason, and the fact that the population of transmitting mobile phones is in close proximity of the harvester and is highly variable, only base station. Transmission will be considered further. From RF survey, DTV, GSM900, GSM1800, 3G and Wi-Fi, shown in Figure 1, were identified as potentially useful ambient RF energy harvesting sources, although DTV appears to be heavily dependent on line-of-sight and

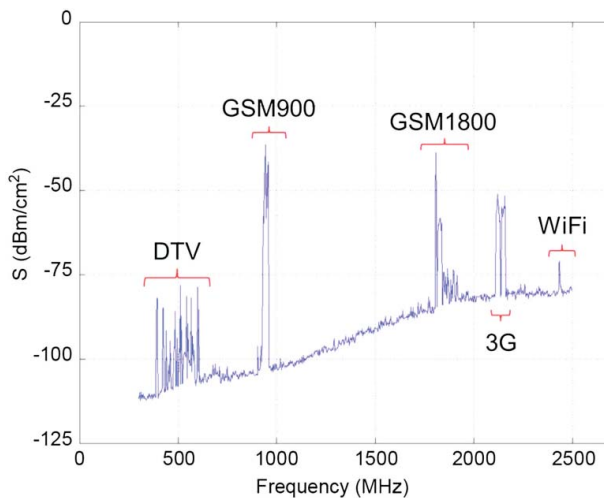


Figure 1. Survey of signal in India.

Table 1. Frequency bands.

Band	Frequencies (MHz)	Average S_{ba} (nW/cm ²)	Maximum S_{ba} (nW/cm ²)
DTV	470–610	0.89	460
GSM900 (MTx)	880–915	0.45	39
GSM900 (BTx)	925–960	36	1930
GSM1800(MTx)	1710–1785	0.5	20
GSM1800 (BTx)	1805–1880	84	6390
3G (MTx)	1920–19,980	0.46	66
3G (BTx)	2110–2170	12	240
Wi-Fi	2400–2500	0.18	6

Table 2. Survey in no. of stations.

Band	S_{ba} threshold	Number of stations	
		Urban	Semi-urban
DTV	40	10	0
GSM900	230	8	2
GSM1800	450	7	3
3G	62	6	4

Table 3. S_{ba} of signal.

Band	DTV	GSM1900 (BTx)	GSM1800 (BTx)	3G (BTx)
S_{ba} (nW/cm ²)	18	48	50	3

sudden changes in atmospheric conditions (e.g. temperature inversion), and Wi-Fi is very dependent on user traffic. It should be noted that the mobile phone base-station transmission employs vertically polarized antennas, placing a constraint on harvester orientation in deployment (Kurup et al. 2003; Kalzar & Prokopec 2011; Didarul & Razaul 2013). With DTV, shown in Table 1, within India, the main transmission has horizontally polarized antennas and repeater transmission has vertically polarized antennas, which record measurements that are found within the urban environment.

This paper demonstrates the analysis of microwave signal strength by designing the antenna in such way that to pick up the signal. In this process, the printed circuit board (PCB) antenna, such as rectangular type and triangular type antennae, was first designed to get GSM900 and GSM1800 as shown in Tables 2 and 3.

2.4. Patch antenna

2.4.1. Open stub antenna

The whip can be made as a trace on a PCB. This is very practical at frequencies over 800 MHz. At lower frequencies, a full-size whip may be too long, even when wrapped around a few corners. The length of the whip should be 10%–20% shorter than the calculation, depending on the dielectric and the thickness of the board. In most cases, 15% shorter is close enough. If the unit is to be handheld, the antenna can be made a little shorter, to compensate the effect of the hand. At 916 MHz, a trace that is 2.25 inches (57 mm) long will provide a reasonable impedance when hand effects are included. Keep the antenna trace away from other circuitry and ground, a quarter of an inch (6 mm), or more. Non-ground circuit traces may be seen by the antenna as part of the ground system, and RF voltages can be induced on nearby traces.

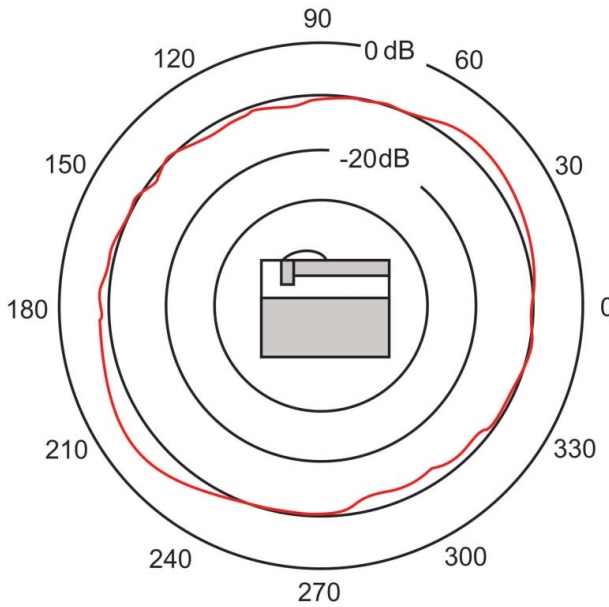


Figure 2. Design of rectangular patch antenna.

The overall size of the board and ground is not critical. The radiation pattern is omnidirectional as shown in Figure 2, with a gain of -8 to -12 dB, when the board is horizontal. Polarization is horizontal. If the whip did not run parallel to the ground, the gain would be higher; however, two sharp nulls would be present. If the board were oriented vertically, with the antenna above the ground plane, the polarization would be vertical. The antenna would have an omnidirectional pattern with -8 dBd of gain. Radiation pattern of design 1 antenna is shown in Figure 3.

2.4.2. Short whip antenna

A simple alternative to the whip is to make it shorter than a quarter wave length and add an inductor near the base of the whip to compensate for the resulting capacitive reactance. The inductor can be made by coiling up the part of the whip itself. This type of antenna can have performance nearly equal to that of a full-sized whip. When tested on the edge of a small board, gain was only 3–4 dB less than a full-sized whip, and the ground plane is shown in Figure 4.

2.4.3. Rectangular and trapezoidal patch antenna

The patch antenna is a very low-profile design, which consists of a round or rectangular patch of metal very close to a ground plane. The patch is usually printed on a circuit board and can be made as part of the enclosure. Antenna coverage is in any direction above the ground plane, or a hemispherical area. The patch antenna does require a substantial amount of area on a PCB, which makes it more practical above 800 MHz. It has a narrow bandwidth; therefore, care must be taken to tune the size of the patch. A practical example for 916 MHz can fit into an area only of 30 cm \times 40 mm. The patch size is 27 mm (wide) \times 38 mm (long) for a board thickness of 0.060 inch. A thinner board or higher dielectric

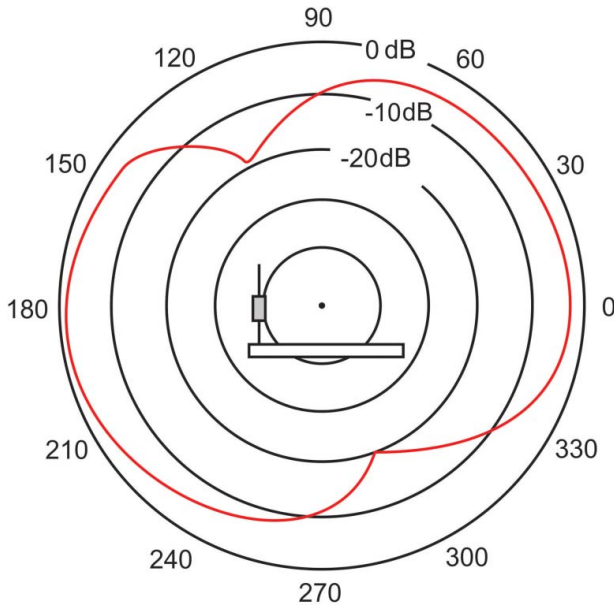


Figure 3. Radiation pattern of design 1 antenna (916.5 MHz).

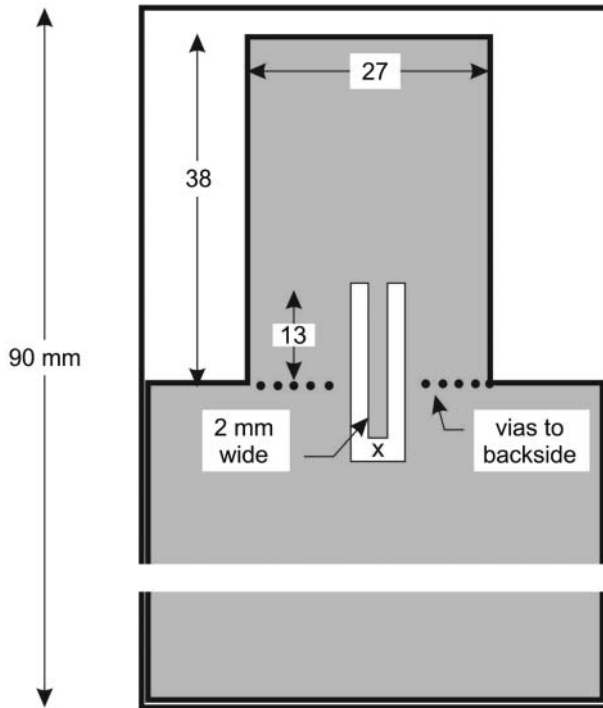


Figure 4. Radiation pattern of short whip antenna.

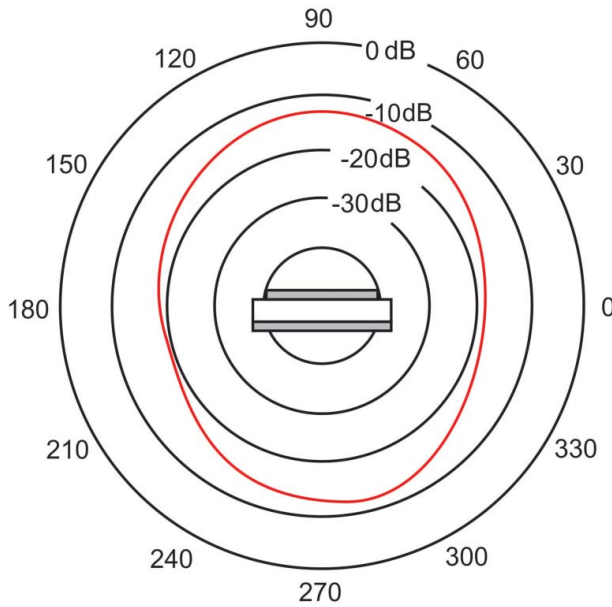


Figure 5. Radiation pattern of trapezoidal patch antenna.

can require cutting the antenna a little shorter. About one-tenth of the antenna is fed with a line crossing through the grounded edge to the 50-ohm point on the patch, or by a transmission line coming up through the bottom of the PCB. The 50-ohm point is about 13 mm away from the ground. The 50-ohm point for any design can be found by moving away from the grounded edge (Thuroczy et al. 2006; Elliott et al. 2010; Ren 2010; Marian et al. 2012). This type of patch is not a full-sized, half-wavelength patch; therefore, performance is quite low when compared to the larger size patch. A full-sized patch has no grounded edge, so via are not required. The example of a rectangular patch has a gain of -8 dB. Placing the board against a larger sheet of metal will improve the gain by another 4 dB. If the antenna is made wider than one inch, up to about three inches wide, a few more dB can be gained (Wei et al. 2013). Polarization is perpendicular to the grounded edge. Gain is good in almost any direction where the patch can be seen, but drops rapidly when looking at the edge of the board. The trapezoidal version allows for less length so that it can fit into smaller spaces. Patterns and behaviour are the same, but the gain is a little lower. We measured about -12 dB maximum as shown in Figure 5, on a $40\text{ mm} \times 90\text{ mm}$ board.

2.5. Antenna configuration

The design of the antenna is based on a planar substrate that has a dielectric constant of 2.2 and a thickness of 10 mils (0.254 mm). The planar antenna consists of S-strip and T-strip which are printed on the two sides (i.e. the front side for T-strip and the back side for the S-strip) of the substrate, respectively. There is no direct electrical connection (e.g. by a shorting via) between the frontside and the backside. The T-strip (its strip width) is

fed by a 50- Ω microstrip line, while the S-strip (its strip width) is terminated at a ground plane (its length).

The upper section (its width) of the T-strip is fitted (leaving a space of) into an area surrounded by the upper section of the S-strip while the lower section of the T-strip overlaps with the lower section of the S-strip, forming a two-strip line (Park et al. 2004; Shinohara 2011). The height (H) of the planar antenna can be adjusted for an optimal performance. The compactness of the planar antenna is attributed to the folded configuration of the S-strip and T-strip (specifically, the folded two-strip line), while the broadband performance is a result of the mutual coupling between the S-strip and the T-strip. The feeding point is set up at the centre of the upper half section of the ground plane. This set-up is completely for the purpose of accurate measurement. The 50- Ω microstrip line was excited at the feeding point by a wire-port as shown in Figure 6, instead of a microstrip port (i.e. a wave-port).

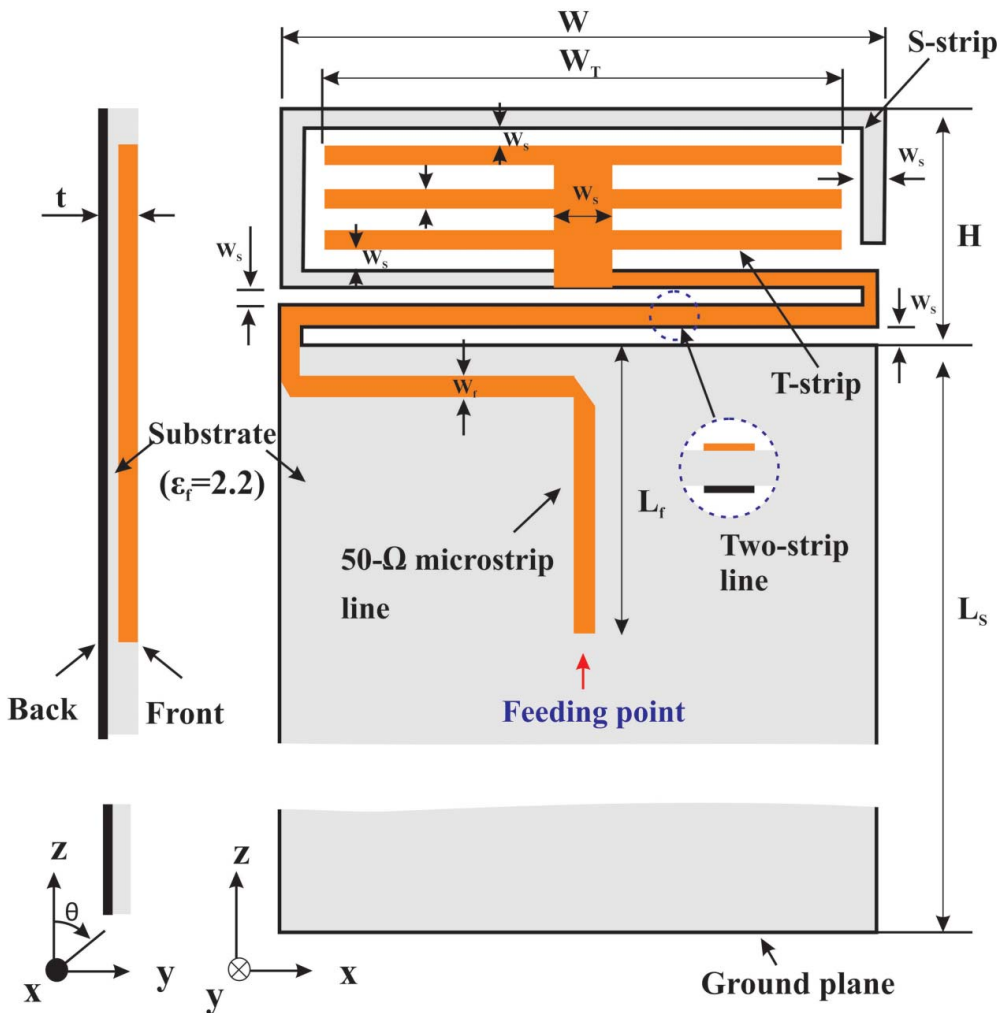


Figure 6. 50 Ω microstrip lines antenna.

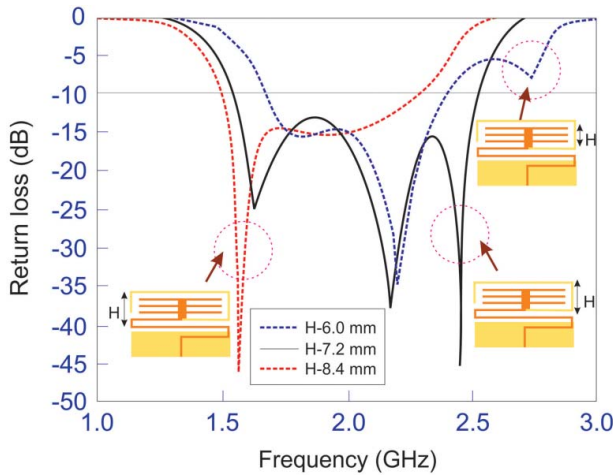


Figure 7. Characteristics of antenna height configuration.

The height H is adjusted by changing the number of the equidistant crossbars of the T-strip, e.g. 2, 3 and 4 crossbars for 6.0, 7.2 and 8.4 mm, respectively, as shown in Figure 6. The planar antenna has a maximum bandwidth at 7.2 mm. The maximum bandwidth is close to 50%. The total size of the planar antenna is $18\text{ mm} \times 7.2\text{ mm} \times 0.254\text{ mm}$, which is more compact than the previously published antennas, e.g. $30\text{ mm} \times 10\text{ mm} \times 2\text{ mm}$, $62\text{ mm} \times 10\text{ mm} \times 6\text{ mm}$, $27\text{ mm} \times 12.5\text{ mm} \times 3.5\text{ mm}$, $22\text{ mm} \times 5\text{ mm} \times 5\text{ mm}$, and $20\text{ mm} \times 17\text{ mm} \times 4.7\text{ mm}$ shown in Figure 7.

The effect of the length of the ground plane on the return loss of the planar antenna is exhibited is shown in Figure 8. There is an optimum value for where the planar antenna has the best performance for return loss. The reason for the length dependence is that the ground plane also serves as a radiating element. The optimum value is found to be around

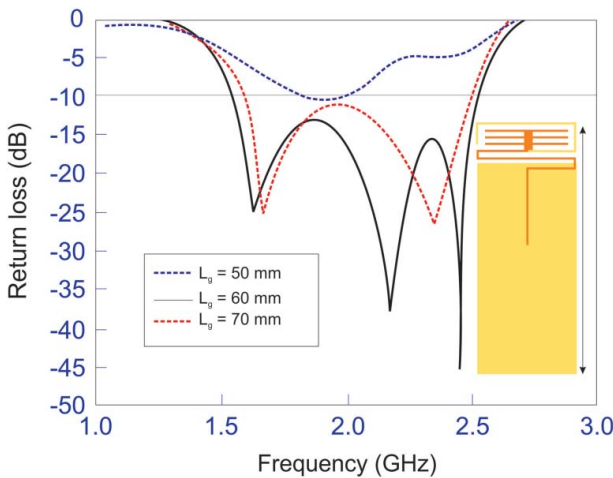


Figure 8. Characteristics of antenna length configuration.

60 mm. (Probably, around 60 mm, the ground plane, the S-strip and the T-strip form a resonant radiator.) Therefore, the planar antenna is suitable for compact mobile handsets.

2.6. Matching network

The optimal load was found; further, broadband optimization was performed to the matching network and the load to ensure good impedance matching throughout the target frequency range and is measured for each band. As with the antenna analysis, and unlike conventional RF circuits that adopt the more traditional half-power bandwidth definition, the rectifier should be within the 10 dB input return loss bandwidth (Dengyo rectennas 2012). The reason for ambient RF energy harvesting applications is that the input RF power is at a premium and so that little energy available should not be wasted by being reflected back from avoidable impedance mismatches at either the antenna or rectifier. Since the input RF power from ambient sources can be represented as a multi-tone source, with power levels fluctuating across the target frequency range, the output impedance of the rectifier is time varying.

2.7. Schottky diode rectification

A Schottky rectifier is formed by making an electrically nonlinear contact between a metal and the semiconductor drift region. The Schottky rectifier is an attractive unipolar device for power electronics applications since it has a relatively low on-state voltage drop and its quality of fast switching. It has been widely used in power supply circuits with low operating voltages due to the availability of excellent devices based upon silicon technology. In the case of silicon, the maximum breakdown voltage of Schottky rectifiers has been limited by the increase in the resistance of the drift region. Commercially available devices are generally rated at breakdown voltages of less than 100 V. The much lower resistance of the drift region for silicon carbide enables development of such Schottky rectifiers with very high breakdown voltages. These devices not only offer fast switching speed but also eliminate the large reverse recovery current observed in high-voltage silicon P-i-N rectifiers. This reduces switching losses not only in the rectifier but also in the insulated-gate bipolar transistors (IGBTs) used within the power circuits. In this paper, the basic structure of the power Schottky rectifier is first introduced to define its constituent elements. The current transport mechanisms that are pertinent to power devices are elucidated for both the forward and reverse modes of operation. In the first quadrant of operation, the thermionic emission process is dominant for power Schottky rectifiers. In the third quadrant of operation, the influence of Schottky barrier lowering has a strong impact on the leakage current for silicon devices. In the case of silicon carbide devices, the influence of tunnelling current must also be taken into account when performing the analysis of the reverse leakage current (Le et al. 2008; Khidre et al. 2013). The basic one-dimensional structure of the metal semiconductor or Schottky rectifier structure is together with electric field profile under reverse bias operation. The applied voltage is supported by the drift region with a triangular electric field distribution if the drift region doping is uniform. The maximum electric field occurs at the metal contact. The device undergoes breakdown when this field becomes equal to the critical electric field for the semiconductor. When a negative bias is applied to the cathode, current flow occurs in the Schottky rectifier

by the transport of electrons over the metal semiconductor contact and through the drift region as well as the substrate. The on-state voltage drop is determined by the voltage drop across the metal–semiconductor interface and the ohmic voltage drop in the resistance of the drift region, the substrate and its ohmic contact. At typical on-state operating current density levels, the current transport is dominated by majority carriers. Consequently, there is insignificant minority carrier stored charge within the drift region in the power Schottky rectifier. This enables switching the Schottky rectifier from the on-state to the reverse blocking off-state in a rapid manner by establishing a depletion region within the drift region (Li et al. 2002; Lee et al. 2008; Mikeka et al. 2011). The fast switching capability of the Schottky rectifier enables operation at high frequencies with low power losses making this device popular for high-frequency switch-mode power supply applications. With the advent of commercially available high-voltage Schottky rectifiers based upon silicon carbide, they are expected to be utilized in motor control applications as well.

3. Results and discussion

Distinct effects have been identified from the analysis of the measured data. The received signals with increasing distance and number of trees obstructing the signal path is decayed at a considerably slow rate at the trunk, fruits and leaves for 0.9 and 1.8 GHz as shown in Figures 9 and 10. But, for frequency at 2.3 GHz, the signal strength decreases at a nearly

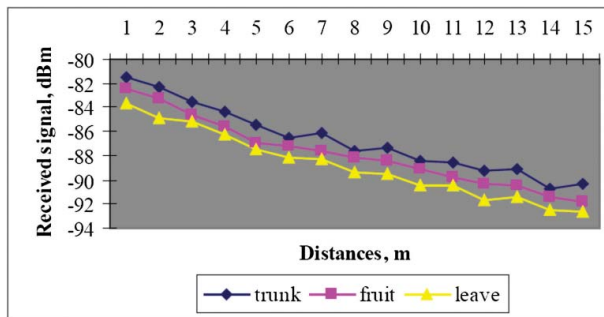


Figure 9. Received signal for different distance at frequency of 0.9 GHz.

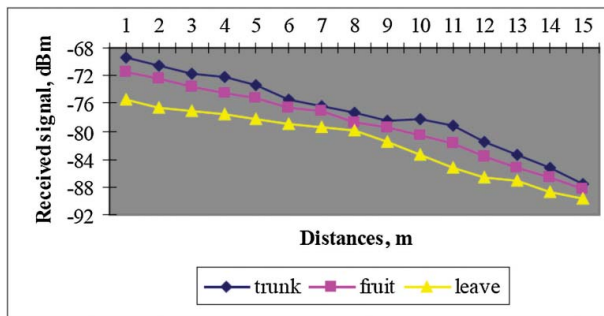


Figure 10. Received signal for different distance at frequency of 1.8 GHz.

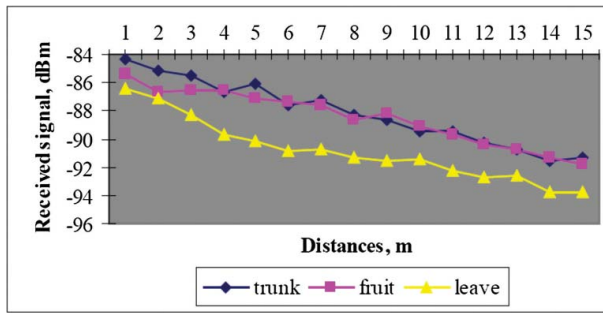


Figure 11. Received signal for different distances at frequency of 2.3 GHz.

constant and smooth rate. The values of the received signal for the trunk and fruit are almost the same when measurement is done at the second row of trees. It seems that the received signal at 0.9 GHz is better and stronger when compared with the propagation measurements at 1.8 and 2.3 GHz.

The range of received signals for both frequencies at 1.8 and 2.3 GHz is almost the same. The received signal with a small number of trees obstructing the signal path decayed at a considerably faster rate relative to that measured when more trees obstructed the path. The change in attenuation rate occurs because, at small foliage depth, propagation between the transmitter and the receiver is primarily by a strongly attenuated line-of-sight component, while at relatively large distances inside the estate, multiple scattering of radio waves by the various constituent parts of the trees becomes the major contributor to the received signals.

Received signal for different distance at a frequency of 2.3 GHz is shown in Figure 11. As the frequency increases, the number of fruits and leaves has a greater effect upon the signal received as their physical size approximates to the wavelength of the transmitted signal, leading to a higher probability of signal blockage.

The PMM is fully integrated into the rectifier; it helps to manage the power produced. Power Module is required for performing maximum power point tracking (MPPT). The BQ25504 has a built-in battery management module, which is used to control the duty cycle of the output power to the load. The programmed PMM continuously charges the storage capacitor and the load was automatically connected to the storage capacitor when the capacitor voltage reaches an upper limit and automatically gets disconnected when it reaches the lower limit

Figure 12 represents the hardware component of harvesting microwave signal to generate power. Figure 12(a) shows the PCB antenna, the red wire shown in the figure represents the feed point. Figure 12(b) shows the charging of mobile phone battery. This output is taken in the feed point, and from the feed point it is given to the battery of 12 V, where the output of the battery is given to regulator. Figure 12(c) shows the output voltage taken in the multimeter.

4. Conclusion

Thus the paper puts forth the connection that the low-power energy harvesting has become a new trend and being accepted all over. This new kind of 'alternative energy' with the use

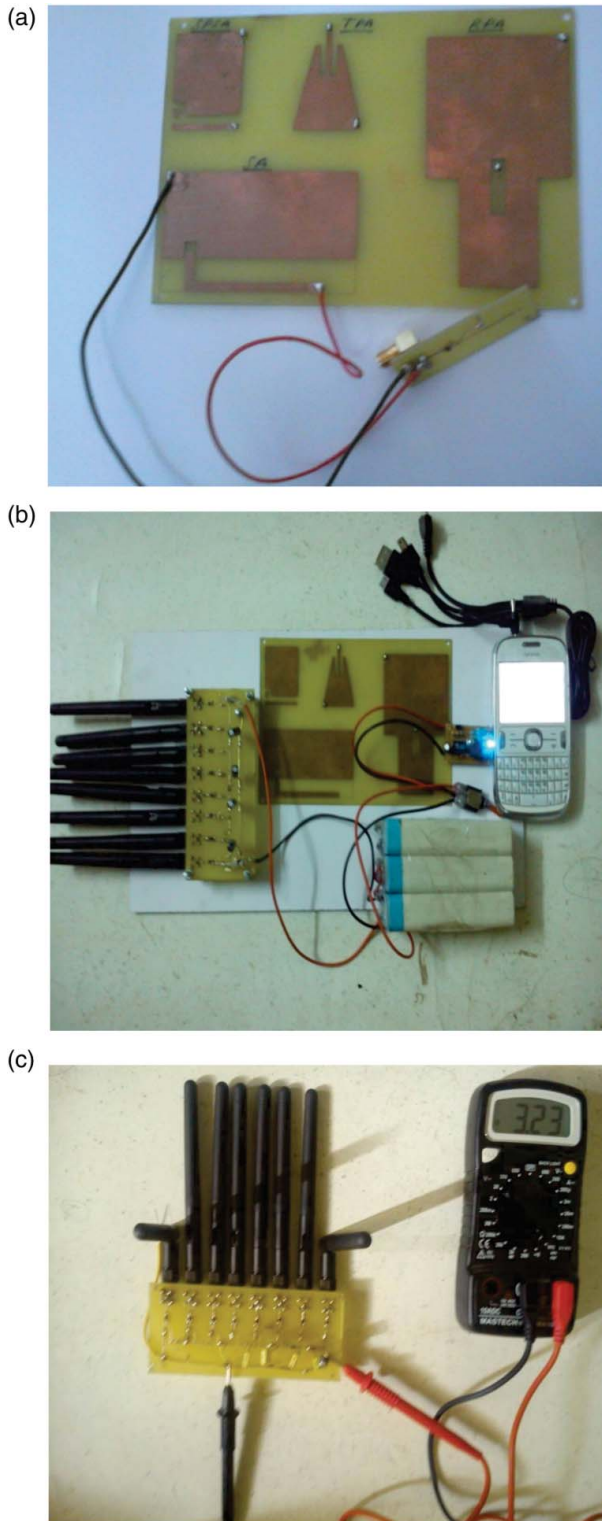


Figure 12. Hardware component of harvesting microwave signals to generate power: (a) printed circuit board; (b) charging of mobile phone; (c) measurement of voltage.

of a rectenna puts forth a high efficiency, and also this energy can be stored, which has an analogous application in the solar energy, where sometimes photovoltaic modules are used to charge batteries that subsequently supply power to other devices. A thorough investigation was made and it was found that it is quite cheaper and a more flexible material. With respect to the antenna, it is concluded that the dimensions can be reduced by analysing the current distribution on the conductors of the surface. Moreover, that non-symmetrical cuts can modify the radiation pattern of antenna. With respect to the rectifier, it is concluded that the use of microstrip lines for the matching circuit design, contributed to a lower soldering loss than the components such as inductors and capacitors.

Acknowledgements

The authors are grateful to Mr. R. David Ravikumar, General Manager, National Centre for Radio Astrophysics, Tata Institute of Fundamental Research, Udthagamandalam (Ooty), India, for helping the authors to understand the mode of microwave harvesting and to obtain various frequencies at the same point.

Disclosure statement

No potential conflict of interest was reported by the authors.

Notes on contributors

Dr. B. Paulchamy received his Ph.D. in Digital Signal Processing, Approach for De-Noising from EEG signal from Anna University Chennai, M.E degree in Applied Electronics from PSG College of Technology, Coimbatore, affiliated to Anna University Chennai, Tamil Nadu and B.E degree in Electronics and communication Engineering from National Engineering College, Kovilpatty, affiliated to Anna University Chennai, Tamilnadu. He has more than a decade of teaching experience in various Engineering colleges in Tamil Nadu. Currently he is working as Professor and Head of department of ECE at Hindusthan Institute of Technology, Coimbatore. His research interests include Signal processing, Image processing and soft computing. He published around 15 papers in refereed conferences and journals. He is the Life Member in the Indian Society for Technical Education and also IEANG.

Dr. J. Jaya received her Ph.D in Information and Communication Engineering from Anna University, Chennai. She completed her M.Tech in Advanced communication systems from SASTRA University, Tanjore, Tamilnadu and B.E in Electronics Communication Engineering from Sri Ramakrishna Engineering College, Coimbatore, Tamilnadu. She has 18 years of Teaching and Research experience in various institutions. She presently holds the post of Principal in Akshaya College of Engineering and Technology, Coimbatore. She is a pioneer in the fields such as Image Processing, Signals and Systems, Digital Signal Processing, Medical Image Processing and Optimization Technology. She has published two books, and has published 28 research papers in International journals and 34 research papers in National level. She has reviewed many National and International level books and journals. She is a proud member of various chapters like IEEE, Indian Society for Technical Education (ISTE) Computer Society of India (CSI), Indian Women Network IWN, International Association of Computer Science & Inf. Tech. (IACSIT), ICTATC, International Association of Engineers (IAENG) and IETE.

Mr. A. Venkatesh received his B.E degree in Electrical and Electronics Engineering from SKP Engineering College, Affiliated to Anna University, Chennai, Tamilnadu and M.E degree in Applied

Electronics from Hindusthan College of Engineering and Technology, Coimbatore, Affiliated to Anna University Chennai, Tamilnadu. Currently he is working as an Assistant Professor in the department of ECE at Hindusthan Institute of Technology, Coimbatore. He had Sound Knowledge in Electrical Machines and Soft Computing. He published variety of technical papers in refereed conferences and journals. He is the Life Member in the Indian Society for Technical Education and also IEANG.

References

- Nihon Dengyo Kosaku Company Ltd & Volvo Tech. 2012. *Dengyo rectennas*. Tokyo: Author.
- Angelopoulos ES, Ana stopoulos AZ, Kaklamani DI, Alexandridis AA, Lazarakis, Dangakis K. 2006. Circular and elliptical CPW-fed slot and microstrip-fed antennas for ultrawideband applications. *IEEE Elliptical CPW Fed Slot Microstrip Fed Antennas Wireless Propag Letts*. 5:294–297.
- Didarul M, Razaul M. 2013. Comparison study of path loss models of WiMAX at 2.5 GHz frequency band. *Int J Future Commun Netw*. 6:12–24.
- Elliott P, Toledano MB, Bennett J, Beale L, de Hoogh K, Best N, Briggs DJ. 2010. Mobile phone base stations and early childhood cancers: case-control study. *Br Med J*. 340:1–7.
- Kalzar L, Prokopec J. 2011. Propagation path loss models for mobile communication. *IEEE International Conference Radioelektronika*. 19–20 April 2011, Brno.
- Khidre A, Lee KF, Elsherbeni AZ, Yang F. 2013. Wide band dual-beam U-slot microstrip antenna. *IEEE Trans Antennas Propag*. 61:1415–1418.
- Kurup DG, Himdi M, Rydberg A. 2003. Synthesis of uniform amplitude equally spaced antenna arrays using the differential evolution algorithm. *IEEE Trans Antennas Propag*. 51:2210–2217.
- Le T, Mayaram K, Fiez T. 2008. Efficient far-field radio frequency energy harvesting for passively powered sensor networks. *IEEE J Solid-State Circuits*. 43:1287–1302.
- Lee KF, Yang SLS, Shk A. 2008. Dual and multiband U-slot patch antennas. *IEEE Antenna Wireless Propag Lett*. 7:645–647.
- Li K, Ingram M, Rausch E. 2002. Multibeam antennas for indoor wireless communications. *IEEE Trans Comm*. 50:192–194.
- Marian V, Allard B, Vollaie C, Verdier J. 2012. Strategy for microwave energy harvesting from ambient field or a feeding source. *IEEE Trans Power Electron*. 27:4481–4491.
- Mikeka C, Arai H, Georgiadis A, Collado A. 2011. DTV band micropower RF energy-harvesting circuit architecture and performance analysis. In: 2011 IEEE International Conference on RFID-Technologies and Applications. p. 561–567.
- Monti G, Congedo F. 2012. UHF Rectenna using a Bowtie Antenna. *Progress In Electromagnetics Research C*. 26:181–192.
- Park JY, Han SM, Itoh T. 2004. A rectenna design with harmonic-rejecting circular-sector antenna. *IEEE Antennas Wireless Propag Lett*. 3:52–54.
- Pi Z, Khan F. 2011. An introduction to millimeter-wave mobile broadband systems. *IEEE Commun Mag*. 49:101–107.
- Pinuela M, Yates DC, Lucyszyn S, Mitcheson PD. 2013. Maximizing DC-to-load efficiency for inductive power transfer. *IEEE Trans Power Electron*. 28:2437–2447.
- Rappaport TS, Murdock JN, Gutierrez F. 2011. State of the art in 60 GHz integrated circuits & systems for wireless communications. *Proc IEEE*. 99:1390–1436.
- Ren W. 2010. Compact H-shaped slot antenna for 2.4/5.8GHz WLAN applications. In: IEEE International Conference on Multimedia Technology (ICMT). p. 1–4.
- Sadasiva Rao B, Raju GSN. 2011. Shaped beams from thick arrays. *Int J Electr Commun Eng*. 4:577–592.
- Salter T, Metzger G, Goldsman N. 2009. Parasitic aware optimization of an RF power scavenging circuit with applications to smart dust sensor networks. In: IEEE Radio Wireless Symposium. p. 332–335.
- Shinohara N. 2011. Power without wires. *IEEE Microw Mag*. 12:S64–S73.

- Thuroczy G, Molnar F, Szabo J, Janossy G, Nagy N, Kubinyi G, Bakos J. 2006. Public exposure to RF from installed sources: site measurements and personal exposimetry. In: First European Conference on Antennas and Propagation. p. 1–4.
- Wei Y, Ji C, Galvan F, Couvillon S, Orellana G, 2013. Dynamic modeling and resilience for power distribution in smart grid communications (SmartGridComm). In IEEE International Conference on Smart Grid Communications. p. 85–90.
- Yang P, Yang F, Nie ZP, Zhou HJ, Li B, Tang XF. 2011. Robust beamformer using manifold separation technique for semispherical conformal array. IEEE Antenna Wireless Propag Lett. 10:1035–1038.
- Wong KL, Kuo JS, Chiou TW. 2001. Compact microstrip antennas with slots loaded in the ground plane. IEEE Antenna Propag Intl Conf. 2:623–626.
- Chen ZN, See TSP, Chia MYW. 2003. Broadband dual-polarization stacked microstrip antennas for Bluetooth applications. Microwave Optic Technol Lett. 37:364–366.

ARTICLE

Proficient Technique for High Performance Very Large-Scale Integration System to Amend Clock Gated Dual Edge Triggered Sense Amplifier Flip-Flop with Less Dissipation of Power Leakage

A. N. Duraivel^{1,*}, B. Paulchamy², and K. Mahendran²

Clocked flip flops are used to memory in synchronous or clocked series networks, adjusting the individual clock signal status. Therefore, at these times of clock signal transfer, the state of the memory unit and the state of the whole electrical structure change. It's only during signal transfer that the key to a flip-flop being correctly operated. Two transitions from 0 and 1 are followed by a clock pulse, and 1 to 0. The pulse shift is defined by the positive and negative sides of the pulse. The data on or off the clock cycle edges are recorded by a single-edge trigger flip flop (SETFF), but the flip flop with the double-edge sensor amplifier (DETSAFF). Another common technique for dynamic energy consumption reduced when the device is idle is the clock gating. In this document. Sleep is used to reduce the power of the leakage Here are the following: High threshold voltages sleep transistors are used. Among the supply voltage and VDD the sleep pMOS transistor and the pull-up system and between the network and the ground GND a sleep NMOs Transistor is located. With sleep transistors, CG-SAFF can save up to 30% of its power during zero input switching operation. For different sequential device architecture, the proposed flip-flop may be used.

Keywords: Pull-Up Network and Pull-Down Network, Sense Amplifier (SA), Sleep Method, Zero Input Switching Activity, Clock Gated Sense Amplifier Flip-Flop (CGSAFF), Dual Edge Triggered Sense Amplifier Flip-Flop.

1. INTRODUCTION

In Field of Very Large-Scale Integration System (VLSI), the power consumption factor is controlled by the clock system sources. The proposed clock system involves the clock distribution network and Flip-Flops (FF). FLIP-FLOPS (FF) has a higher rate and less power consumption and is one of complex systems with complicated clocking elements. Its performance analysis is the main factor for an analysis of the entire synchronization circuit's performance. Normally, SETFF uses one clock edge, another clock edge is idle, but on both sides of the clock cycle rising and dropping edge, DETFF fetches input data. Since

both clock edges are involved in the flip-flop activated dual edge (DETFF), the data output is doubled when the SETFF works at half of its clock frequency. Many low-energy DETFF systems have now been suggested. A flip flop (FF), which is the Dual Edge Sense Amplifier flip flop (DETFF) power efficient system, is divided into two major classes: pulse DETFF, master-slave DETFF activated. The DETFF's master-slave are built by negative as well as positive clock edge flip-flops in parallel. DETFF caused by pulses has individual one phase and is of compact logic circuit complexity. The input clock gating strategy is practical to decrease complex power usage to minimize redundant changes in the pulse generator of DETSAFF [1]. The use of sleep technology in the synchronous method to minimize more dissipation of the power of the leaks related to idle block design.

The following portion is part of this planned work. The current Section 2 has the current memory unit and Clock gated Dual Edge Sensual Amplifier Flip-Flop amplifier that is activated by the double edge. Then Section 3 Explain the new approach to reducing the

¹Electronics and Communication Engineering, Kings Engineering College, Chennai 602117, Tamilnadu, India

²Electronics and Communication Engineering, Hindusthan Institute of Technology, Coimbatore 641032, Tamilnadu, India

*Author to whom correspondence should be addressed.

Email: duraivel.n@gmail.com

Received: 23 June 2020

Accepted: 15 October 2020

dissipation of leakage further. Up to 30% of the energy savings discussed in Part IV of the Sleep Transistor CGSAFF will achieve. In Section 5, the work is finally outlined.

2. LITERATURE SURVEY

The timing components of the integrated circuit (flip-flops and latches) (IC). Flip flops are often used as a timing feature in the IC as storage elements that use more power. One of the common methods of reducing power consumption is the dual-edge triggering principle. Since both the flip-flop (DETFF), which is triggered by the dual-edge, does not fade, therefore, the data flow is high relative to the flip-flop triggered by a traditional one-edge. The (1) Latch-Mux category and (2) flip-flop pulse are two key divisions [1] of the DETFF. Two levels, a master and a slave consist of the latch-mux. These two stages are organised in parallel, one of which is translucent at one level of the clock, and another one at the opposite level of the clock is again transparent. The second form, pulse, caused flip-flops into two more subcategories: (1) Implicit and (2) Explicit. The pulse generator that produces pulses is used in both forms.

The pulse creator produces pulse inside the memory unit, which income the form of pulse is triggered tacit (IP-FF), while the pulse is produced outside the device (EP-FF). On the other hand if EP-FF control is additional than IP-FF, EP-FF is commonly consumed for clock distribution that delivers the pulse generator's overhead power. The definition of double-edge trigger is harder to incorporate into IP-FF, whereas EP-FF is suitable for dual-edge triggering. Various DETFFs were planned in designs for low power integrated circuit (ASIC) applications to reduce power consumption.

2.1. Discharging Controlled Flip-Flop Unit

The illustration figure is given in Figure 1 for static flip-flop discharge-controlled discharge (SCDFF). SCDFF has a double pulse generator [2, 4] and static latch arrangement in its overall structure. The clock pulse is externally produced here. This twist is known as an overt pulsed twist (EP-FF). Two static phases of the static latch structure. Transistors m2 (first stage) and m6 are injected into the external pulse (second stage).

The transistor m2 and m6 are activated during the sampling time. In the first step the transistor m to 1 and m3 is introduced into input D. If $D = 1$ and $Q = 0$ (assumption), the transistors m2, m3 and m4 discharge node X. As a outcome, in the second stage the output Q will immediately switch to high levels with a pull-up transistor m5. As long as D is high, node X is still short. The junction transistor m1 and m3 are supplemented by the D input (in the first step), m3 is turned off.

The feedback path is finally opened and the node X at some voltage is pre-charged. In the second step, the D

inverted input is now used to discharge the m7 transistor, so that output Q is discharged through the m6 and m7 tracks. An additional transistor, m4, powered by a complementary programmed signal is controlled at node X for the unwanted discharge. The SCDFF is used primarily to minimize unnecessary switching operation with low power VLSI architecture.

2.2. Static-Pulsed Flip-Flop with Dual Edge Triggering Unit

Figure 2 displays a pulsed flip flop structural figure with a static triggering two-edge [4, 8] (DETSPPF). The DETSPFF is made up of two components: (1) Circuit (2) Static latch explicit pulse generation. There are four inverters and two NMOS-pass transistors in the explicit pulse generator. The delayed and inverted signal, respectively CLK2 and CLK3, is produced. In the drain of the NMOS transistor N5, the delayed CLK2 clock signal is inserted at the similar period that the N5 gate can be operated by the CLK clock signal. The CLK3 inverted clock has been used in the channel of the other NMOS junction transistor N6, at which point the CLK1 inverted clock signal can be regulated at the time. These two signals produce a small sample window, as seen in the diagram, both on the elevated and dropping clock edges [16].

The N1 and N2 pass transistors are enabled to test data inputs during the sampling process. The D and DB data inputs are incorporated in the N1 and N2 transistors into the SB and S static nodes. It helps to keep the wait minimum. The floating of the SB and S static nodes are operated by the N3 and N4 weak NMOS transistors. If the data entry D is strong, the weak NMOS transistor N4 immediately loads the statistic node SB. The reversed data input will be tiny, while the NMOS transistor P2 upto Vdd will charge the static node S. During another sample time, D is low and the static node SB is modified to V through the PMOS transistor. Simultaneously with the feeble NMOS transistor N4 is unloaded the static node SB. The key purpose of DETSPFF is to remove unintended transformations. While the next input is the same as the previous input, the transformation inside the circuit happens again. This means an undesirable transition.

2.3. Adaptive Clocking Dual Edge Triggered Sense Amplifier Flip-Flop

The flip-flop sensor amplifier (ACSAFF) schematic diagram for adaptive clocking of dual edge [5, 14] is shown in Figure 3. ACSAFF is mostly assisted by Ref. [1] the inverter chain clock [2]. Circuit front end [3]. Latch. Latch. Latch. Used to create delayed clock signals is the clock inverter chain. The NC node is extracted from the front end circuit which, in low operation, disables the clock inverter chain [4]. Both CLK and CLK3 have been high on the CLK climbing edge for a small period and both

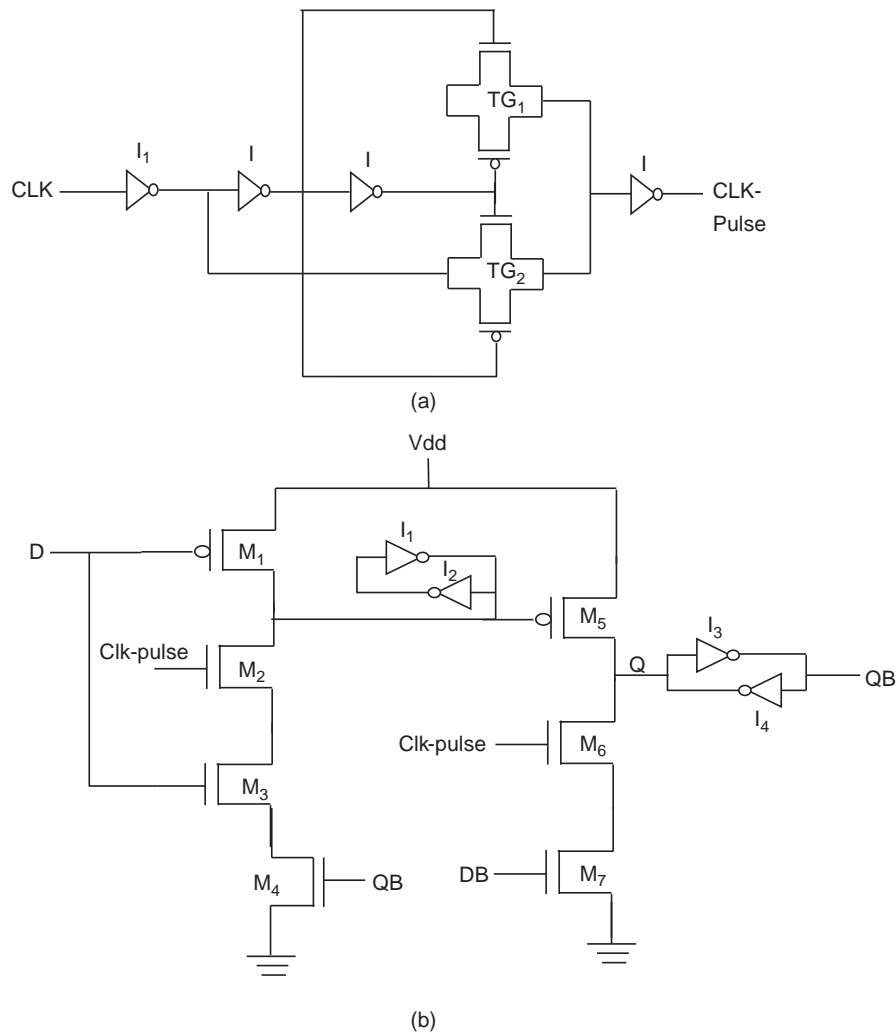


Fig. 1. Illustration diagram of proposed circuit (a) dual pulse generator (b) static latch.

CLK1 and CLK4 have both been very high on one CLK climbing edge for a small period. The delays on the front end circuit are applied. If D is not the same as Q data entry, the NC node is charged through N5 and N6 (or) N7 and N8 transistors. Inverted and delayed signals CLK3 and CLK4, the NIC1- and NIC2-transistor signals will be turned on to create the small sample window at the rising or dropping clock edges. The SB (or) RB Node creates an ACSAFF [5], I latch, unloading path during the narrow sample time. The NC node is pushed down via the N2 and the N1 (or) N3 and N4 transistors as the performance shifts when the NC node deactivates the inverter clock chain. If input D is equal to output, Q, SB and RB nodes will keep their previous output high and latch will keep it high. At low switching operation, ACSEFF saves more energy, but needs more junction transistor to incorporate input clocking.

2.4. Dual-Edge Triggered Sense Amplifier Flip-Flop

Figure 4 shows the diagram [4, 7] of the dual-edge flip-flop sensor amplifier (DETSAFF). The DETSAFF has three main components: (1) dual pulse generator to produce pulse signal on the edges of the up and down clock (2) sensing system dependent on the flip-flop sensory amplifier (SAFF) (3) Look. (3) Look. The DETSAFF is an overt form because the pulse signal is produced outside the system and added to a number of flip-flops. In the sensing system the PMOS transistor SP bin1 is enabled, while the node SB is preloaded to Vdd if input D is small (high). Similarly, the PMOS SP2 transistor is enabled when input D is high and the RB node is uploaded to Vdd (high). In this context, the PMOS transformation driven by input in the preload direction is SP1 and SP2.

When D is extreme, node SB is downloaded to DB at low rate via SN1 and node RB is preloaded to Vdd during the translucent time. Similarly, if D is low node, SB is pre-loaded with SP1 upto Vdd and RB is discharged to low

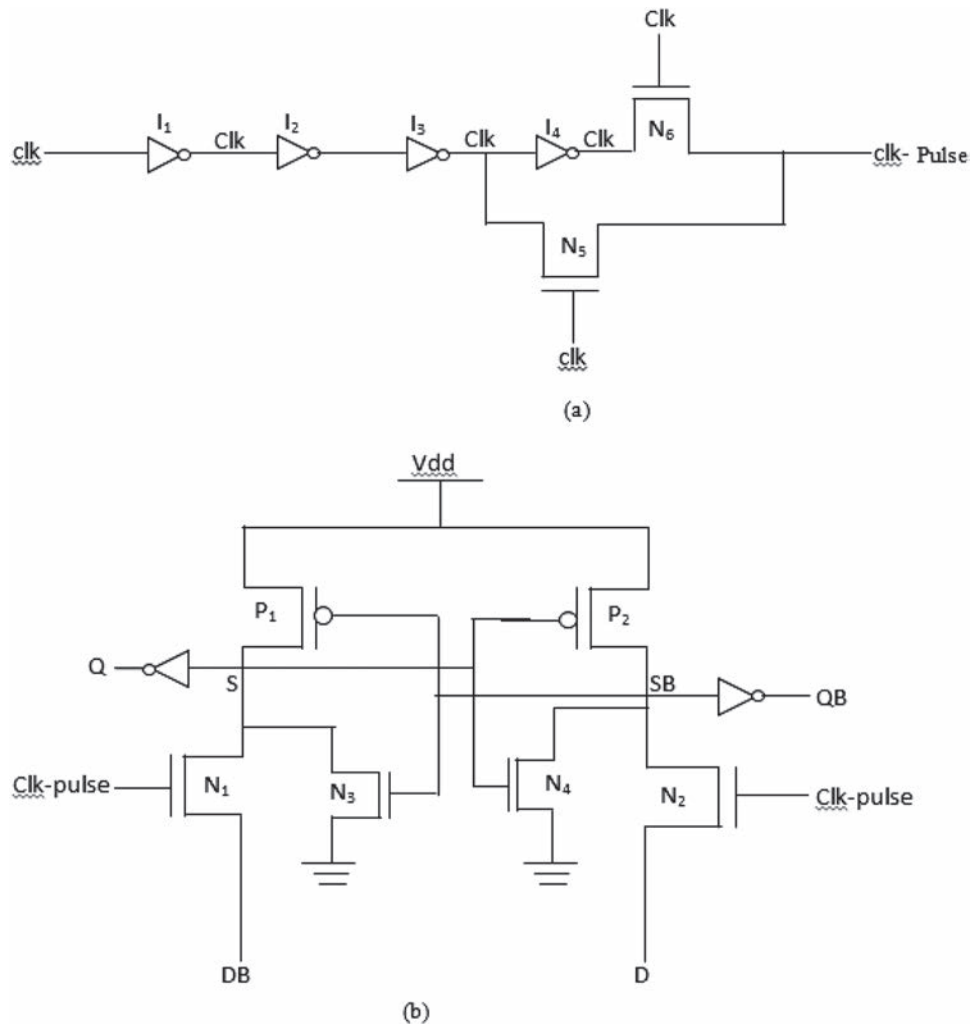


Fig. 2. Schematic diagram of DETSPF (a) dual pulse generator (b) static latch.

state D during the remaining transparent time. SB and RB transmit the signal directly into the LP1 and LP2 pull-up transistors. Data source (D) and inverted source (DB) are fed straight to transistor LN1 and LN2 operated NMOS transistors. Pull up transistors and transfer transistors are used to charge the output node Q and QB. If the flip flop is not visible, the previous value is still maintained using LP3, LP4, LN ltd3, and LN4 internal transistors. Although the data change operation is minimal, the dual pulse generator causes an unwanted clock pulse. As a result, in low switching operations, DETSAFF absorbs more power.

2.5. Clock Gated Sense Amplifier Flip-Flop

In Figure 5 you can view the clock-driven pulse generator [3, 15]. The comparator is here a significant source for both X and Y signals. Differential inputs D and DB are the comparator inputs. As power signals the buffered outputs Q1 and QB1 are. Both (X & Y) signals have respectively been introduced into the CN3 and CN4 doors.

If D differs from the Q output, the X node signal is high and the Y node signal is low. The NMOS transistor CN3 is activated and a clock sign is sent to CL via CN3. As a gated clock, CL is titled. AT simultaneously generates an inverted CLK1 clock signal inserted into the CN6 passenger transistor as well as a CLK3 delay gated clock inserted into the CP6 pass junction transistor. These 2 indicators (CLK1 and CLK3) serve as a gate control signal (TG).

The signal for the TG input is the CL clock). At the up and down edge of the clock the pulse is produced. In the next n iterations, when input D is still the same, the X is pulled down near to the ground and Y to high. Thus, the CN3 junction transistor is disabled and the input pulse of clock is not transferred to CL. The CL is drawn down to the ground via CN4. The clock signal is finally blocked and the flip flop remains invisible. In Figure 6 is presented the schematic diagram of the Clock Gated Sense Amplifier flip flop (CG-SAFF). The detection stage is identical to DET-SAFF. The main alteration among DET-SAFF [6]

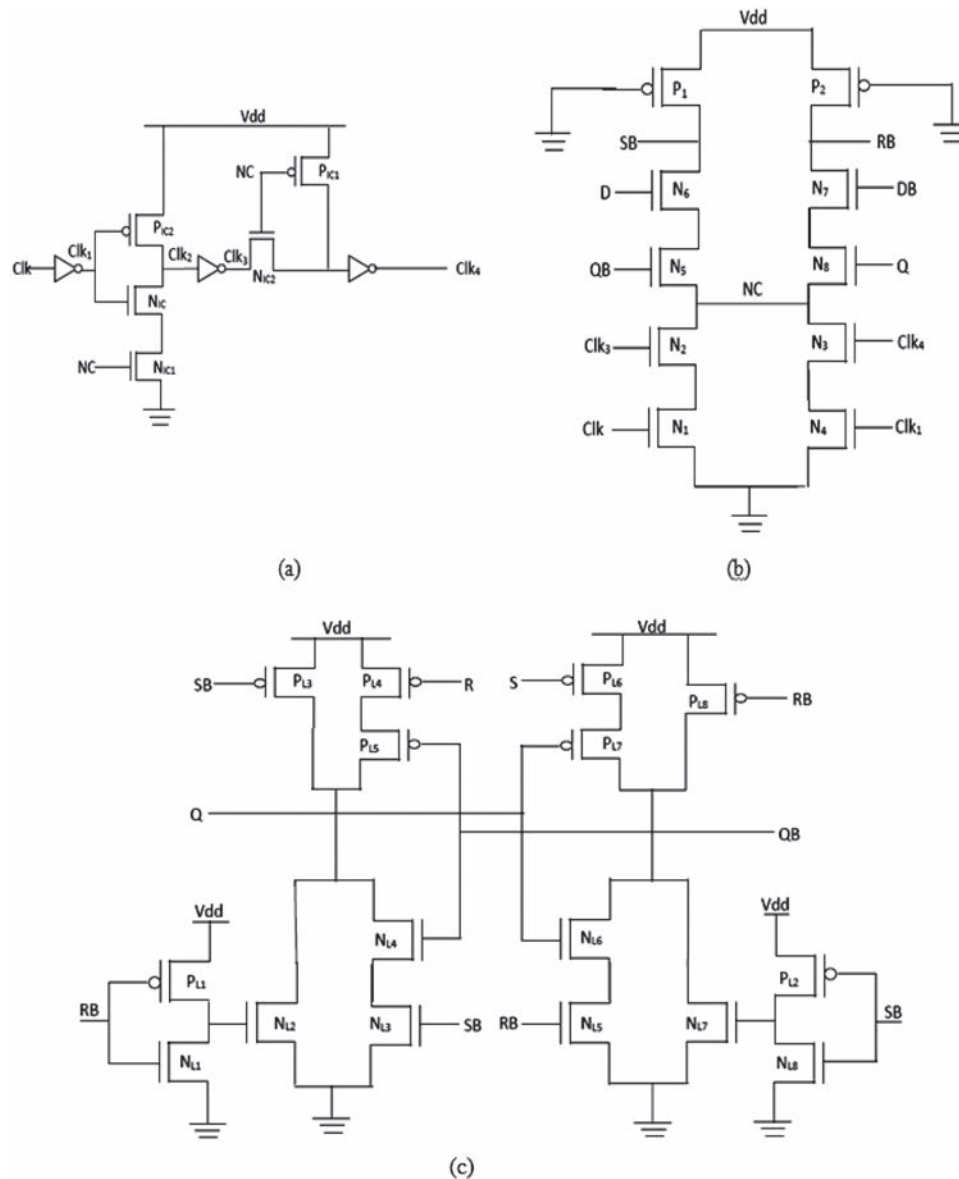


Fig. 3. Schematic diagram of ACSAFF (a) adaptive clocking inverter chain (b) front end sensing stage (C) latch.

and CG-SAFF in the latching phase is the former requirement of pulses but no pulse signal is needed in the latter phase. The buffers are created with differential outputs Q1 and QB1, used to create X and Y rather than Q and QB.

3. PROPOSED METHOD TO REDUCE POWER LEAKAGE

3.1. Sleep Method

This paper deals with CGSAFF's suggestion for a new sleep technique [9–13] to decrease leakage and complex dissipation. High-threshold transistors in the sleeping procedure are taken into consideration. The pMOS transistor sleep configuration is taken among the source power, the

VDD network And a sleep transistor nMOS and pull-up mechanism between the network and the GND field. The solution planned as seen in Figure 6.

Once the electric circuit is in energetic position, the sleep transistor is activated and switched off if the circuit is inactive. This is the following. By cutting the logic circuit off from power supply and soil voltage in sleeping condition, this technique decreases the sub threshold outflow current. The transistors of sleep are sleep driven. The S and S' Signal Characteristic. The sleep signal S is kept at a logic level of 1 tension during daily activity and the supplementary sleep symbol S' at a logic level of 0 tension. The Pull down network and Pull Up Network circuit works like a conventional inverter. During the usual operations of the M1 and M2 transistors the

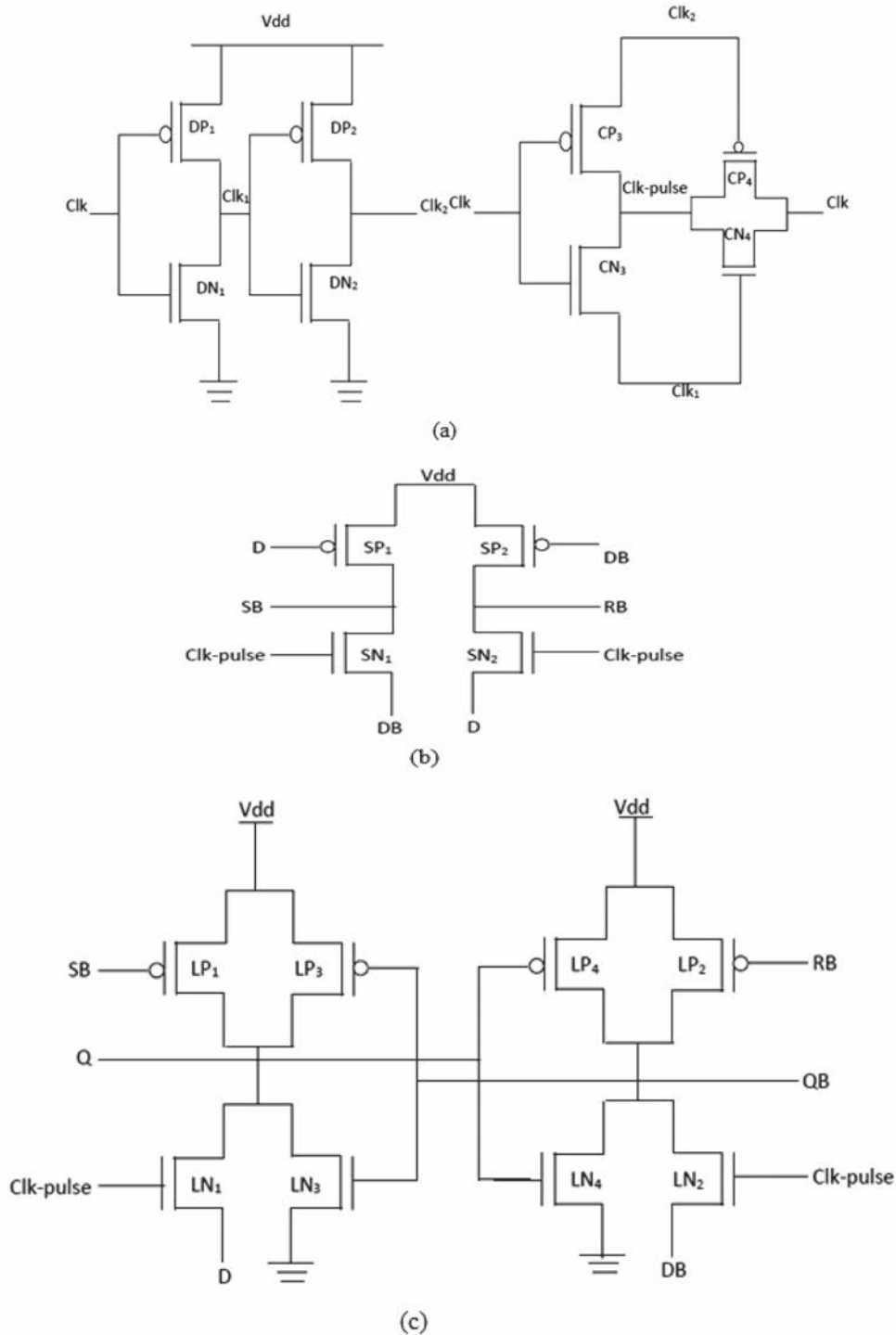


Fig. 4. Schematic diagram of DETSAFF (a) dual pulse generator (b) sensing stage (c) latch.

Virtual Vss node will also be on the ground and the Virtual Vdd node will be on Vdd. This results in reversed output by the inverter. If the inverter needs to work in standby or sleep method, the S signal will be retained at logic 0 and the S signal at logic 1 will be kept. This ensures that all networks reach a cut off condition (pull down and

pull up). The virtual Vss node is therefore virtual and the Virtual Vdd node practically powerful. The inverter then enters idle mode. The theoretical Vss increases due to the cut-off M1 and M2 transistors; the possible Vdd decreases. Pull Down Network's source of body potential increases and increases Pull Down Network's threshold

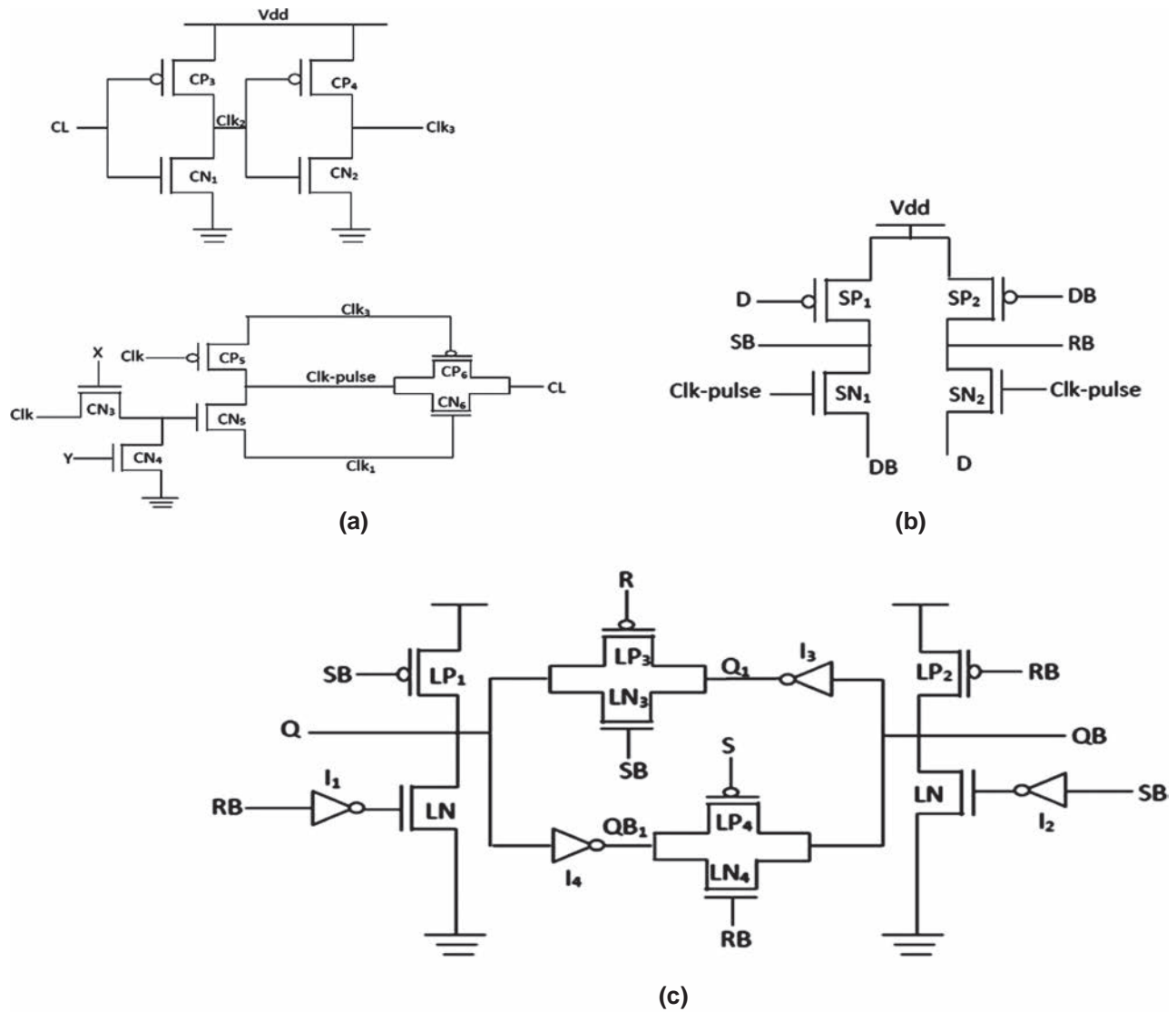


Fig. 5. Schematic diagram of CG-SAFF (a) clock-gated pulse generator (b) sensing stage (c) latching stage.

voltage. This decreases the Pull Down Network’s sub-threshold current. In the Virtual Vdd and Virtual Vdd, the size of the stacked sleep transistors (W/L) defines possible stages. The sleep inverter reduces the capacity of the leakage. But it lacks state information as it goes into idle mode.

According to VLSI theory, static power is commensurate with the voltage, whereas power declines at a lower voltage. The dissipation of the leakage power in the circuit is condensed by the sleep transistor. The PMOS transistor functions as a resistance in this technology, reducing the VDD’s power release to the pull up junction transistor. At the connection points between the PMOS and the Pull Up Network [17], the simulated power supply is voltages. The NMOS connects from a virtual source to the network.

3.2. Proposed System Design

In this work Clock Gated Sense Amplifier Flip-Flop (FF) has the weaker characteristics and implements the new sense-amplifier which is built using the Flip-Flop circuits with the part of sleep transistor circuit. This transistor circuit consists of different characteristic features with the higher speediness and decreased power usage. The sense-amplifier flip-flop circuit is proposed by the various sleeping factor which is implemented within the devices such as microchips, Digital Components, and the real time applications. Sleep methods are also developed to reduce power leakage dissipation. Figure 7 below shows the updated CG-SAFF design. The transistor of both PMOS and NMOS are mounted in one component of the flip-flop. Therefore, when it is not necessary and when an input adjustment for the flip-flop is not needed, the proposed clock-gating technique has been found to disconnect the switch. Dynamic

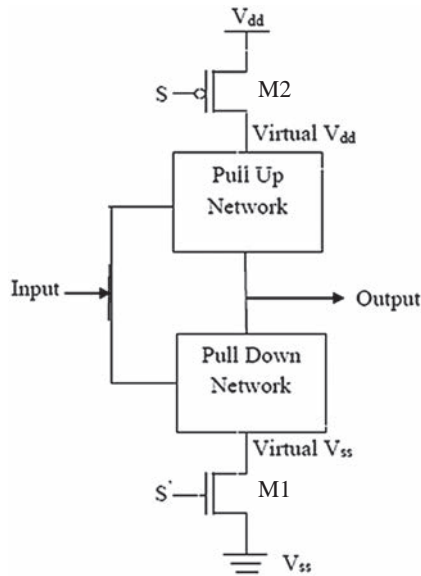


Fig. 6. Sleep approach.

power consumption can be minimised by clock gating techniques with SAFF. CG-SAFF will save up to 30 per cent of power during zero-input shifting operation using the sleep transistor. For different sequence device designs, the proposed Flip-Flop may be used. Displays Figure 8 Changed concept waveform for CG-SAFF.

To reduce the leakage power consumption, the technique proposed is indicated as CG-SAFF. This implemented

technique is subjected towards the higher performance which acquires less power than the other techniques. So, the proposed technique is used in the various applications.

The proposed various stages such as the Pulse Phase, sensing and latching phase is shown in the Figures 8 and 9. The proposed technique at the sensing stage is termed as the conditional pre-charging method which is used to reduce the redundancy of the interior nodal point. By the reflection of two input points such as PMOS transistors in inbuilt in the way of nodal point. The condition is based on the nodal point that the D value remains at the higher range during the n cycles. Due to the higher range of D, SB tends to be discharged. For instance, during the $(n - 1)$ cycles, the SB waveform tends to be lower where the clock pulse is higher. The RB point within the first cycle remains to be higher in the pulse region due to the pre-charged factor. The pre-charging stage is controlled with the conditional factor, pull down pathway of SB and RB region is critical with the individual one junction transistor. This transistor will decrease the settling time within the circuit. Due to the reduction in the discharging time, power will be low, delay will be minimized and therefore speed will be higher.

4. RESULT

Table I shows the influence of the power factor between CG-SAFF and modified CG-SAFF. This work is subject

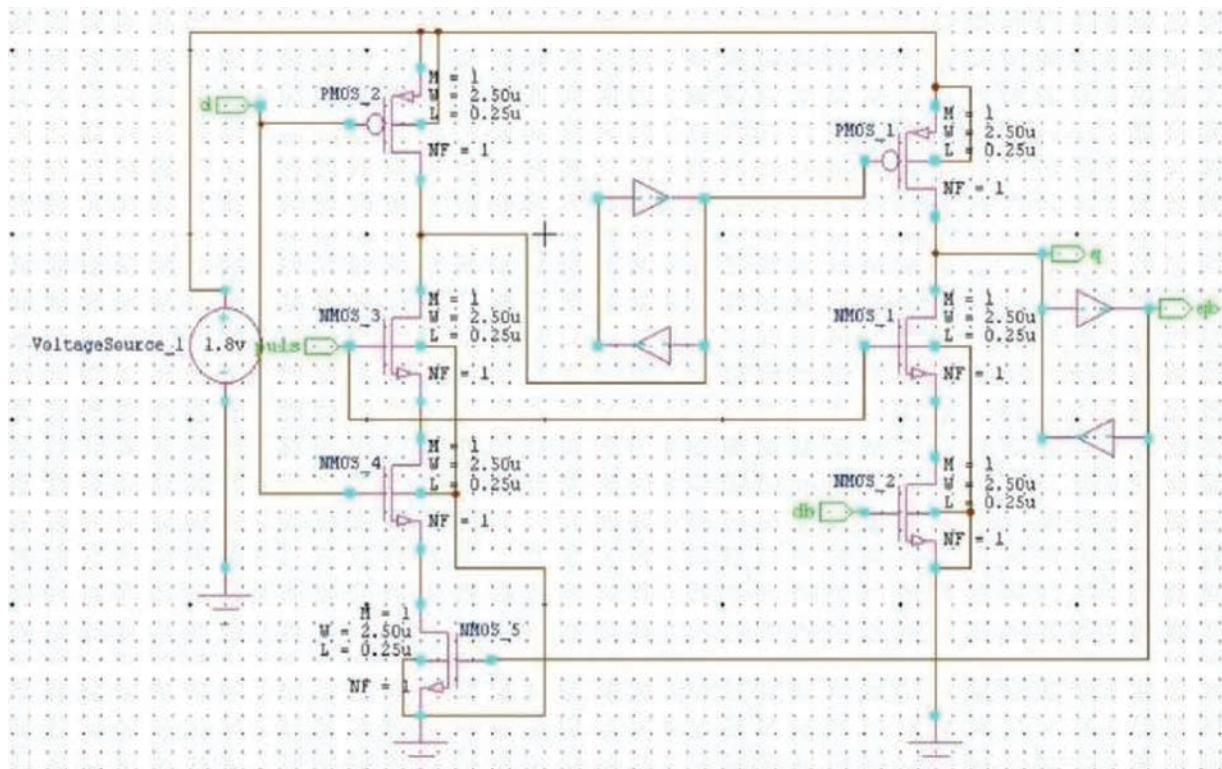
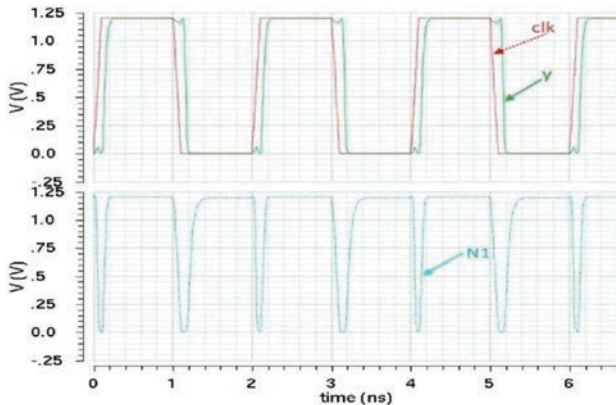


Fig. 7. Schematic diagram modified CG-SAFF.

Table I. Influence of power factor between CG-SAFF and modified CG-SAFF.

Parameter	CG-SAFF	MCG-SAFF
Energy (mw)	79	53
Data to Q delay (Sec)	8.999	3.004
Clock to Q delay (Sec)	5.999	5.004
Number of transistors	38	36
Rise time (ps)	79.06	92.16
Fall time (ps)	78.47	91.26
MOCF (GHz)	1.25	1.25

**Fig. 10.** Simulation waveform of modified CG-SAFF.

different test models can be used for simulating the FF designs.

5. CONCLUSION

The proposed MCGDET-SAFF is not designed directly from the basic Flip Flop design circuit. To obtain the final circuit with high efficiency in terms of low power and high speed, a stage wise improvement/modification is done on the edge triggered Flip Flop. For instance, a sense amplified Flip Flop is incorporated with the clock gating for reducing the power consumption and reducing the memory. Then it will be extended into dual edge triggered clock gated sense amplifier Flip Flop. Finally, the CGDETSAFF remains modified into MCGDET-SAFF and it can provide very less power consumption and it will increase the speed in the application.

References and Notes

- Phyu, M.W., Fu, K., Goh, W.L. and Yeo, K.-E., **2011**. Power-efficient explicit-pulsed dual-edge triggered sense-amplifier flip-flops. *IEEE Transaction Very Large Scale Integration (VLSI) System*, 19(1).
- Phyu, M.W., Goh, W.L. and Yeo, K.S., **2005**. A Low-Power Static Dual Edge Triggered Flip-Flop Using an Output-Controlled Discharge Configuration. *Proceeding of IEEE International Symposium on Circuits and Systems*, Vol. 3, pp.2429–2432.
- Wang, X. and Robinson, W.H., **2013**. Asynchronous data sampling within clock-gated double edge triggered flip-flops. *IEEE Transaction on Circuits and Systems*, 60(9), pp.2401–2411.
- Aliakbar, G. and Hamid, M., **2005**. Dual Edge Triggered Static Pulsed Flip-Flops. *Proceeding of 18th International Conference on VLSI Design*, Vol. 2005, pp.846–849.
- Liu, Y.T., Chiou, L.Y. and Chang, S.J., **2006**. Energy-Efficient Adaptive Clocking Dual Edge Sense Amplifier Flip-Flop. *Proceeding of IEEE International Symposium on Circuits and Systems (ISCAS 2006)*, pp.4329–4332.
- Yu, C.-C., **2007**. Design of Low Power Double Edge Triggered Flip-Flop Circuit. *Proceeding of 2nd IEEE Conference on Industrial Electronics Applications (ICIEA2007)*, pp.2054–2057.
- Zhao, P. et al., **2007**. Low-power clock branch sharing double edge triggered flip-flop. *IEEE Transaction Very Large Scale Integration (VLSI) Systems*, 15(3), pp.338–345.
- Aliakbar, G. and Hamid, M., **2005**. Dual-Edge Triggered Static Pulsed Flip-Flops. *Proc. 18th Int. Conf. VLSI Design*, Vol. 2005, pp.846–849.
- Vinaykumar Madasu and Kedharnath, B., **2013**. Leakage power reduction by using sleep methods. *International Journal of Engineering and Computer Science*, 2(9), pp.2842–2847.
- Jeon, H.J., Kim, Y.-B. and Choi, M., **2010**. Standby leakage power reduction technique for nanoscale CMOS VLSI systems. *IEEE Transactions on Instrumentation and Measurement*, 59(5), pp.1127–1133.
- Zhou, S., Yao, H. and Zhou, Q., **2011**. Minimization of Circuit Delay and Power Through Gate Sizing and Threshold Voltage Assignment. *IEEE Computer Society Annual Symposium on VLSI*, pp.212–217.
- Matherat, P. and MariemSlimani, **2011**. Multiple threshold voltage for glitch power reduction. *Faible Tension Faible Consommation (FTFC)*, Version 1–7, pp.67–70, DOI: 10.1109/FTFC.2011.5948921.
- Kim, S.H. and Mooney III, V.J., **2006**. Sleepy Keeper: A New Approach to Low-Leakage Power VLSI Design. *International Conference on Conference on Very Large Scale Integration [IEEE Xplore]*, DOI: 10.1109/VLSISOC.2006.313263.
- Zhao, P., Darwish, T.K. and Bayoumi, M.A., **2004**. High-performance and low-power conditional discharge flip-flop. *IEEE Transaction Very Large Scale Integration (VLSI) Systems*, 12(5), pp.477–484.
- Phyu, M.W., Goh, W.L. and Yeo, K.S., **2005**. A Low-Power Static Dual Edge Triggered Flip-Flop Using an Output-Controlled Discharge Configuration. *Proceeding of IEEE International Symposium on Circuits and Systems (ISCAS 2005)*, Vol. 3, pp.2429–2432.
- Aliakbar, G. and Hamid, M., **2005**. Dual-Edge Triggered Static Pulsed Flip-Flops. *Proceeding of 18th International Conference on VLSI Design*, Vol. 2005, pp.846–849.
- Liu, Y.T., Chiou, L.Y. and Chang, S.J., **2006**. Energy-Efficient Adaptive Clocking Dual Edge Sense-Amplifier Flip-Flop. *Proceeding of IEEE International Symposium on Circuits and Systems (ISCAS 2006)*, pp.4329–4332.
- Nikolic, B., Oklobdzija, V.G., Stajanovic, V., Jia, W., Chiu, J.K. and Leung, M.M., **2000**. Improved sense-amplifier based flip-flop: Design and measurements. *IEEE Journal of Solid-State Circuits*, 35(6), pp.876–883.
- Kim, J.I. and Kong, B.S., **2000**. Dual edge-triggered flip-flop with modified NAND keeper for high-performance VLSI. *Current Applied Physics*, 4(1), pp.49–53.

A Simple Approach to Stepwise Synthesis of Graphene Oxide Nanomaterial

Paulchamy B¹, Arthi G² and Lignesh BD³¹Professor and Head, Department of ECE, Hindusthan Institute of Technology, Coimbatore, India²SRF, International Advanced Research Centre for Power Metallurgy and New Materials, Hyderabad, India³M.Tech (Nanotechnology) Student, Anna University Regional Centre, Coimbatore, India

Abstract

Technology research in nanotechnology promises breakthroughs in areas such as materials and manufacturing, nanoelectronics, medicine and healthcare, energy, biotechnology, information technology, and national security. One of the crucial bottlenecks for the application of graphene-based systems in materials science is their mass production. Meeting the requirements, graphene oxide (GO) has been considered widely as a prominent precursor and a starting material for the synthesis of this processable material. This work describes the synthesis of Graphene oxide (GO) by both Hummer's and Modified Hummer's method and its characterization by XRD, FT-IR spectroscopy and SEM. The results obtained from the characterization techniques mentioned above is also explained. This GO acts as a base material for the future application of water purification, super capacitors and as a composite in antibacterial activity, solar cells and coatings.

Keywords: Graphene oxide (GO); Hummer's method; Oxidation; XRD; FT-IR spectrum; SEM

Introduction

Nanoscience and nanotechnology primarily deal with the synthesis, characterization, exploration, and exploitation of nanomaterials. Carbon, one of the most common atoms on Earth, occurs naturally in many forms and as a component in countless substances which are called allotropes of carbon. Graphene, a "wonder material" is the world's thinnest, strongest, and stiffest material, as well as being an excellent conductor of heat and electricity. It is the basic building block of other important allotropes. Graphene oxide (GO) is of great interest due to its low cost, easy access, and widespread ability to convert to graphene. Scalability is also a much desired feature.

Graphene oxide is graphite that has been oxidized to intersperse the carbon layers with oxygen molecules, and then reduced, to separate the carbon layers completely into individual or few layer graphene. Graphene oxide is effectively a by-product of this oxidation as when the oxidizing agents react with graphite, the interplanar spacing between the layers of graphite is increased. The completely oxidized compound can then be dispersed in a base solution such as water, and graphene oxide is then produced [1-22].

A large number of oxygen-containing functional groups have been introduced onto both sides of a single graphite sheet (namely, graphene). The implantation of functional groups overcomes the inter-sheet van der Waals force and enlarges the interlayer spacing. The sheets in such an expanded structure are then easily pulled open using an external force such as sonication. That is, the expanded graphite is exfoliated into multi-layered or even single-layered sheets. Generally, the oxidized graphene sheets, namely, GO, acquire multiple defects and the degree of the defects is subject to the additive amount of oxidant and the oxidizing time [22]. GO is produced by the oxidative treatment of graphite by one of the principle methods developed by Brodie, Hummers or Staudenmeier.

Properties of GO

Graphene oxide, like graphite oxide, is often described as an electrical insulator, due to the disruption of its sp^2 bonding networks. In actuality, this is not entirely true. The ability for graphene oxide

to conduct electrons depends on the amount of oxidization in the compound, as well as the method of synthesis. It's the oxidization in the solution that disturbs electrical conductivity, so while highly oxidized graphene oxide would be a very poor conductor of electricity, even if graphene oxide were to be heavily reduced, though it would possibly be able to conduct electricity, it would still not perform as well as high quality graphene monolayers in terms of electron mobility.

However, there are methods that can be used to counteract this situation, and those are by a process often referred to as functionalization, which means to chemically modify a substance in order to develop its properties to suit a specific application. The main properties include: 1) Hygroscopicity, 2) Dispersibility and 3) Toxicity [23-31].

Functionalization of graphene oxide can fundamentally change graphene oxide's electrical properties. The resulting chemically modified graphenes (CMGs) could then potentially become much more adaptable for almost limitless applications. There are many ways in which graphene oxide can be functionalized, depending on the desired application.

Methods and Materials

GO consists of graphene sheets decorated mostly with epoxide and hydroxyl groups. Rapid heating of GO results in expansion and delamination, due to evaporation of the intercalated water and evolution of gases from pyrolysis of the oxygen containing functional groups. The structure and properties of GO depend on the synthesis

***Corresponding author:** Paulchamy Balaiah, Professor and Head, Department of ECE, Hindusthan Institute of Technology, Coimbatore, India, Tel: 0422-4393113; E-mail: balurjp@yahoo.co.in

Received November 07, 2014; Accepted December 16, 2014; Published January 01, 2015

Citation: Paulchamy B, Arthi G, Lignesh BD (2015) A Simple Approach to Stepwise Synthesis of Graphene Oxide Nanomaterial. J Nanomed Nanotechnol 6: 253. doi: [10.4172/2157-7439.1000253](http://dx.doi.org/10.4172/2157-7439.1000253)

Copyright: © 2015 Paulchamy B, et al. This is an open-access article distributed under the terms of the Creative Commons Attribution License, which permits unrestricted use, distribution, and reproduction in any medium, provided the original author and source are credited.

method and degree of oxidation. The most common method of synthesis is chemical method of synthesis by Hummer's method [28]. This method of synthesis can be varied by varying the oxidizing agents used to exfoliate graphite flakes. Here, we represent two method of synthesis technique one is by common method and other by modified method of synthesis namely, Hummer's and Modified Hummer's method of synthesis.

Chemicals required

Graphite Flakes (acid treated 99%, Asbury Carbons), Sodium nitrate (98%, Nice chemicals), Potassium permanganate (99%, RFCL), Hydrogen peroxide (40% wt, Emplura), Sulphuric acid (98%, ACS), Hydrochloric acid (35%, RANKEM).

Hummer's method of synthesis

Graphene oxide was synthesized by Hummers method through oxidation of graphite. The stepwise preparation is given as follows:

1. Graphite flakes (2 g) and NaNO_3 (2 g) were mixed in 50 mL of H_2SO_4 (98%) in a 1000 mL volumetric flask kept under at ice bath (0-5°C) with continuous stirring.
2. The mixture was stirred for 2 hrs at this temperature and potassium permanganate (6 g) was added to the suspension very slowly. The rate of addition was carefully controlled to keep the reaction temperature lower than 15°C.
3. The ice bath was then removed, and the mixture was stirred at 35°C until it became pasty brownish and kept under stirring for 2 days.
4. It is then diluted with slow addition of 100 ml water. The reaction temperature was rapidly increased to 98°C with effervescence, and the color changed to brown color.
5. Further this solution was diluted by adding additional 200 ml of water stirred continuously.
6. The solution is finally treated with 10 ml H_2O_2 to terminate the reaction by appearance of yellow color.
7. For purification, the mixture was washed by rinsing and centrifugation with 10% HCl and then deionized (DI) water several times.
8. After filtration and drying under vacuum at room temperature, the graphene oxide (GO) was obtained as a powder.

Modified Hummer's method of synthesis

This modified method of synthesis involves both oxidation and exfoliation of graphite sheets due to thermal treatment of solution. The stepwise synthesis method is given as follows:

1. Graphite flakes (2 g) and NaNO_3 (2 g) were mixed in 90 mL of H_2SO_4 (98%) in a 1000 ml volumetric flask kept under at ice bath (0-5°C) with continuous stirring.
2. The mixture was stirred for 4 hrs at this temperature and potassium permanganate (12 g) was added to the suspension very slowly. The rate of addition was carefully controlled to keep the reaction temperature lower than 15°C.
3. The mixture is diluted with very slow addition of 184 ml water and kept under stirring for 2 hrs. The ice bath was then removed, and the mixture was stirred at 35°C for 2 hrs.

4. The above mixture is kept in a reflux system at 98°C for 10-15 min. After 10 min, change the temperature to 30°C which gives brown colored solution.
5. Again after 10 min, change it to 25°C, and maintain the temperature for 2 hrs.
6. The solution is finally treated with 40 ml H_2O_2 by which color changes to bright yellow.
7. 200 ml of water is taken in two separate beakers and equal amount of solution prepared is added and stirred for 1 hr.
8. It is then kept without stirring for 3-4 hrs, where the particles settles at the bottom and remaining water is poured to filter.
9. The resulting mixture is washed repeatedly by centrifugation with 10% HCl and then with deionized (DI) water several times until it forms gel like substance (pH- neutral).
10. After centrifugation the gel like substance is vacuum dried at 60°C for more than 6 hrs to GO powder.

The following Figure 1 shows the synthesized GO solution as well as powder form.

Results and Discussions

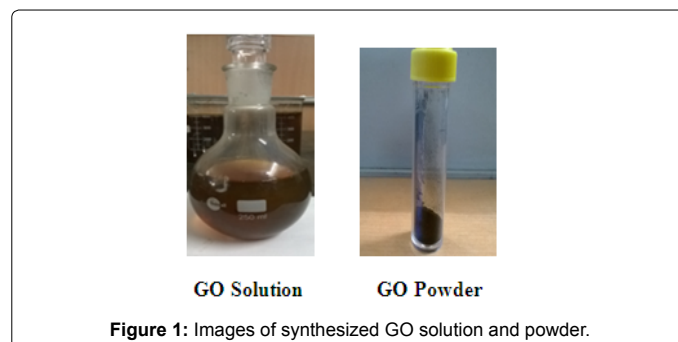
The synthesized GO by Hummer's and Modified Hummer's methods are characterized by X-Ray Diffraction Analysis (XRD), Fourier Transform- Infrared Spectroscopy (FT-IR), Raman Spectroscopy, Scanning Electron Microscopy (SEM) & FESEM.

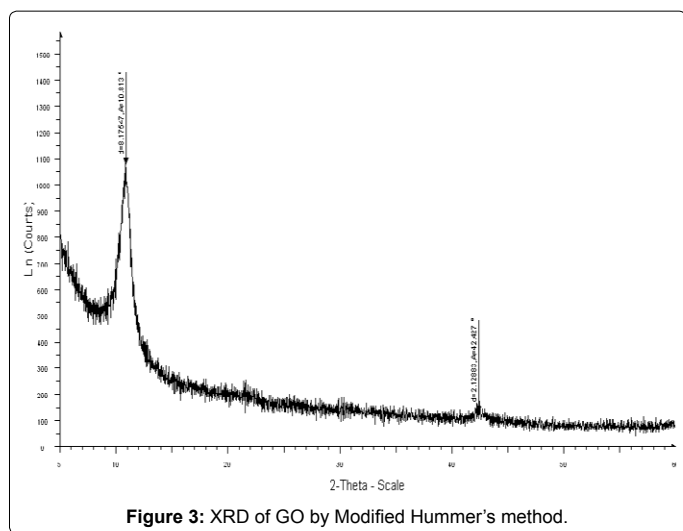
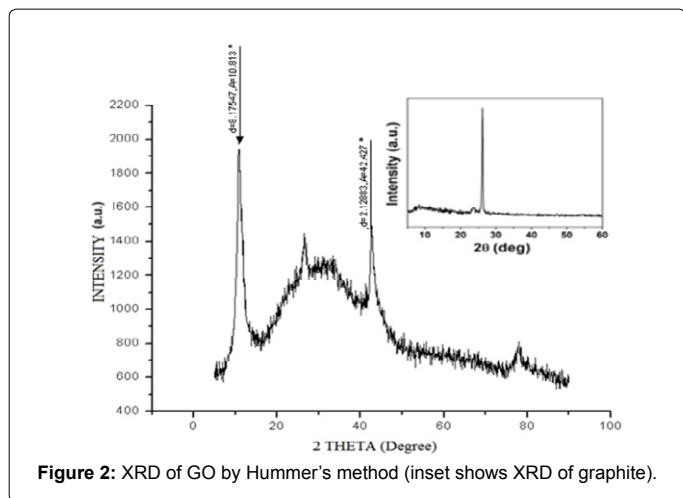
XRD analysis

The X-ray diffraction (XRD) is the most widely used technique for general crystalline material characterization. It is used to Measure the average spacing's between layers or rows of atoms, determine the orientation of a single crystal or grain. The XRD pattern obtained for as synthesized GO nanoparticles by Hummer's method is shown in Figure 2.

It shows the diffraction peak at $2\theta=10^\circ$, which is mainly due to the oxidation of graphite. The diffraction peak of pure graphite is found around 26° , corresponding to the highly organized layer structure with an interlayer distance of 0.34 nm along the (002) orientation is shown as inset in Figure 2. The XRD pattern for synthesized GO by Modified Hummer's method is shown in Figure 3.

The disappearance of the peak at 26° and appearance of the peak at 10° , shows that the product is completely oxidized after the chemical oxidation and exfoliation, indicating an increase in d-spacing from 0.34 nm to 0.82 nm.





FT-IR analysis

It is a technique adopted to obtain an infrared spectrum of absorption, emission, and photoconductivity of a solid, liquid or gas. Also it can be utilized to quantitative analysis of an unknown mixture. FTIR measurement was employed to investigate the bonding interactions in graphene before and after the oxidation process. It assumes the intensities of the peaks are directly related to the amount of sample present.

Figure 4 shows that synthesized GO has a peak at 1081 cm^{-1} which is attributed to the C-O bond, confirming the presence of oxide functional groups after the oxidation process. The peaks in the range of 1630 cm^{-1} to 1650 cm^{-1} show that the C=C bond still remained before and after the oxidation process. The absorbed water in GO is shown by a broad peak at 2885 cm^{-1} to 3715 cm^{-1} , contributed by the O-H stretch of H_2O molecules. This supports the fact that GO is a highly absorptive material, as verified by its ability to become a gel-like solution.

SEM analysis

Scanning Electron microscopy provides morphology and structure of nanomaterials. Figure 5a shows the SEM image of typical graphite. From SEM image it is clear that how the sheets are stalked together in Figure 5a. Figure 5b shows the SEM image of exfoliated GO. It clearly

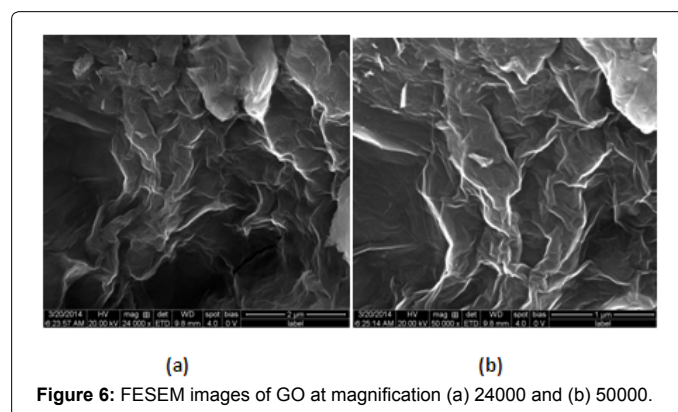
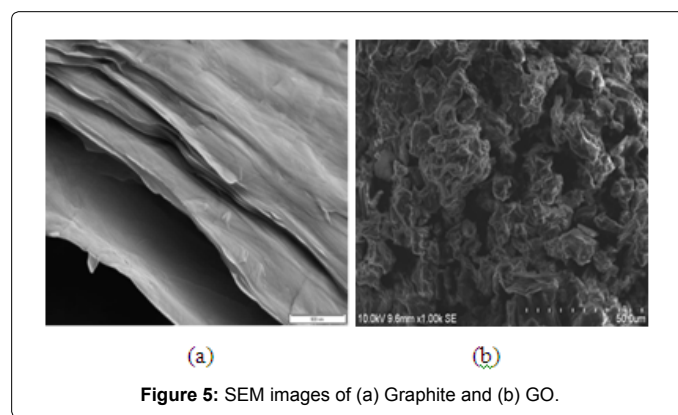
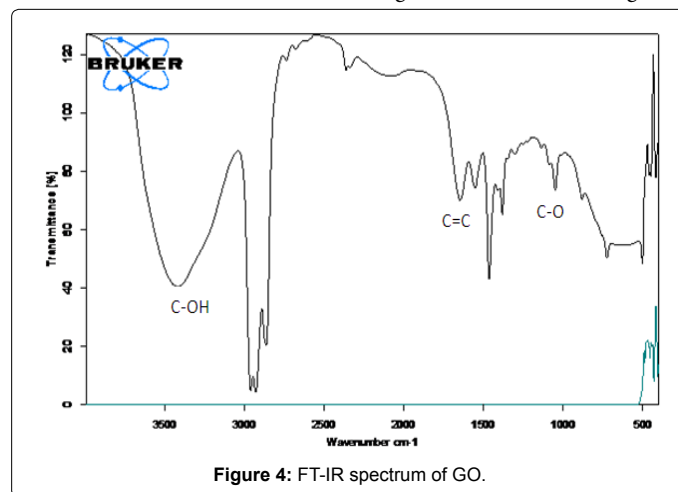
shows that how the graphene sheets are exfoliated.

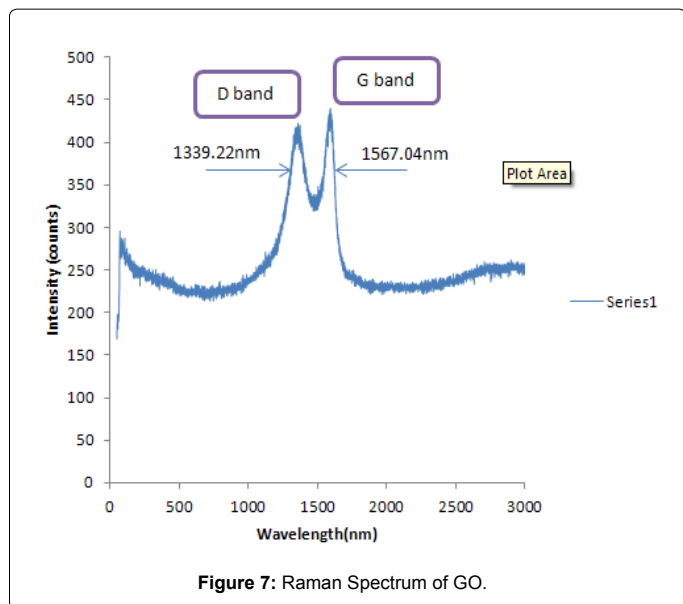
FESEM analysis

The grain size and surface morphology were observed by the field emission scanning electron microscope (FESEM). FESEM images of the Graphene Oxide (GO) have well defined and interlinked three-dimensional Graphene sheets, forming a porous network that resembles a loose sponge like structure as shown in Figure 6.

Raman spectrum analysis

Raman spectroscopy is a widely used tool for the characterization of carbon products, especially considering the fact that conjugated & double carbon- carbon bonds lead to high Raman intensities. Figure 7





shows the Raman spectrum of GO, where the in-phase vibration (G band) of GO is at 1567.04 nm and the disorder band (D band) of GO is at 1339.22 nm.

Conclusion

The Graphene oxide thus synthesized by Hummer's & Modified Hummer's method in this work shows the simple and convenient method of synthesis. This work confirms the existence of oxygen functional groups by XRD and presence of C-O and C=C bonds by FT-IR analysis. Also the exfoliation of graphene sheets is confirmed by SEM image. Thus, the synthesized GO shows many interesting and unique properties that can be applied in variety of applications.

References

- Balaprasad, Farah (2012) Water soluble graphene synthesis. *Chemical Science Transactions* 10: 500-507.
- Ban FY, Majid SR, Huang NM, Lim HN (2012) Graphene Oxide and Its Electrochemical Performance. *Int J Electrochem Sci* 7: 4345-4351.
- Benjamin (2011) Growing graphene via chemical vapour deposition.
- http://www.nanowerk.com/nanotechnology/introduction/introduction_to_nanotechnology_1.php
- Cecilia M, Goki E, Stefano A, Steve M, Andre K, et al. (2009) Evolution of Electrical, Chemical, and Structural Properties of Transparent and Conducting Chemically Derived Graphene Thin Films. *Adv Funct Mater* 19: 2577-2583.
- Chenliang S, Kian PL (2011) Carbocatalysts: Graphene oxide and its derivatives. *Acc Chem Res* 46: 2275-2285.
- Daniel R, Sungjin P, Christopher W, Rodney S (2010) The chemistry of graphene oxide. *Chem Soc Rev* 39: 228-240.
- Daniela C, Dmitry V, Jacob M, Alexander S, Zhengzong S, et al. (2010) Improved Synthesis of Graphene Oxide. *ACS Nano* 4: 4806-4814.
- Deep J, Anchal S, Pulickel A (2011) Graphene synthesis and band gap opening.
- <http://arxiv.org/ftp/arxiv/papers/1212/1212.6413.pdf>
- Geim AK, Novoselov KS (2007) The rise of grapheme. *Nature materials* 6: 183-191.
- Goki E, Manish C (2010) Chemically Derived Graphene Oxide: Towards Large-Area Thin-Film Electronics and Optoelectronics. *Adv Material* 22: 2392-2415.
- Gunasekaran V, Karthikeyan K, Rajneesh M, Sang K (2012) An investigation

of the electrical transport properties of graphene-oxide thin films. *Materials Chemistry and Physics* 132: 29-33.

- Grzegorz S, Jaroslaw S, Joanna J, Rafal K, Mariusz Z, et al. (2012) Graphene Oxide Vs Reduced Graphene Oxide as saturable absorbers for Er-doped passively mode-locked fiber laser. *Optics Express* 20: 19463-19473.
- Heyrovska R (2008) Atomic structures of graphene, benzene and methane with bond lengths as sums of the single, double and resonance bond radii of carbon.
- Hofmann U, Holst R (1939) Über die Säurenatur und die Methylierung von Graphitoxyd. *Chem Ges* 72: 754-771.
- Huang NM, Lim HN, Chia CH, Yarmo MA, Muhamad MR (2011) Simple room-temperature preparation of high-yield large-area graphene oxide. *International Journal of Nanomedicine* 6: 3443-3448.
- Hui X, Qing Y, Fan L, Linsheng T, Xingchun Z, et al. (2013) A graphene-based platform for fluorescent detection of SNPs. *Analyst* 138: 2678-2682.
- Kian P, Qiaoliang B, Manish C (2010) Graphene oxide as a chemically tunable platform for optical applications. *Nature Chemistry* 2: 1015-1024.
- Laura JC, Jaemyung K, Vincent CT, Jiayan L, Franklin K, et al. (2011) Graphene oxide as surfactant sheets. *Pure Appl Chem* 83: 95-110.
- Lewis G, Zhang Y, Chongwu Z (2011) Large Scale Graphene by Chemical Vapor Deposition: Synthesis, Characterization and Applications.
- Ling S, Bunshi F (2000) Massive production of graphene oxide from expanded graphite.
- Long Z, Jiajie L, Huang Y, Yanfeng M, Yongsheng C (2009) Size-controlled synthesis of graphene oxide sheets on a large scale using chemical exfoliation. *Carbon* 47: 3365-3368.
- Ramendra SD, Ranjan K, Retna C, Panigrahi MK (2012) Rapid room temperature chemical route for the synthesis of graphene: Metal-mediated reduction of graphene oxide. *Chemical Communications*.
- Sasha, Dmitriy A, Richard D, Kevin A, SonBinh T, et al. (2007) Synthesis of graphene-based nanosheets via chemical reduction of exfoliated graphite oxide. *Carbon* 8: 1558-1565.
- Sohan C (2012) Bulk synthesis of Graphene Nanosheets.
- Viet HP, Phamm HD, Thanh TD, Sunwook K, Jin SC, et al. (2012) Chemical reduction of an aqueous suspension of graphene oxide by nascent hydrogen. *Journal of Materials Chemistry* 22: 10530-10536.
- Vimlesh C, Kwang S (2011) Highly Selective Adsorption of Hg²⁺ by Polypyrrole-Reduced Graphene Oxide Composite. *Chemical Communications* 47: 3942-3944.
- Virendra S, Daeha J, Zhai L, Das S, Sudipta IK, et al. (2011) Graphene based materials: Past, present and future. *Progress in Materials Science* 56: 1178-1271.
- Vorrada L, Krit T, Passakorn E, Wanchai B, Achanai B (2013) Preparation and Characterization of Reduced Graphene Oxide Sheets via Water-Based Exfoliation and Reduction Methods. *Advances in Materials Science and Engineering* 2013: 923403.
- Wei (2012) Graphite Oxide: Structure, Reduction and Applications.

Citation: Paulchamy B, Arthi G, Lignesh BD (2015) A Simple Approach to Stepwise Synthesis of Graphene Oxide Nanomaterial. J Nanomed Nanotechnol 6: 253. doi: 10.4172/2157-7439.1000253



Comparative Evaluation of Artifacts Removal Techniques from Electroencephalography Signals

Dr. B. Paulchamy*; Dr. J. Jaya**

*Head and Professor,

Hindusthan Institute of Technology,

Department of Electronics and Communication Engineering,

India.

**Principal,

Akshaya College of Engineering and Technology,

India.

Abstract

Cerebrum is the most unpredictable organ in the human body. The mind makes a scope of electric potential for each activity done by the human. For cerebrum judgment the Electroencephalogram (EEG) is the sign of investment. Be that as it may EEG which ought to peruse the scalp electrical movement of the human body likewise understands its physiological and additional physiological exercises which are altogether called as 'artifacts'. These ancient rarities which are the obstruction to EEG ought to be dispensed with for fitting conclusion. In this paper, four systems are produced for the effective evacuation of antiquities. The main technique portrays the fundamental standard behind the free part examination method. The second technique proposes rule behind the neuro fluffy framework obviously. The third strategy displays the guideline of Haar transform. This transform cross-duplicates a capacity against the Haar wavelet with different movements and extends, in the same way as the Fourier transform cross-reproduces a capacity against a sine wave with two stages and numerous extends. The fourth system shows the points of interest behind the multiwavelet transform. They are characterized utilizing a few wavelets with a few scaling capacities. Multiwavelet has a few favorable circumstances in examination with scalar wavelet. The peculiarities, for example, smaller help, orthogonally, symmetry, and higher request rough guess are known to be critical in sign preparing. In this system thresholding strategy is utilized for sign de-noising. It can be seen that the Multiwavelet transform is more efficient in removal of artifacts than the other methods namely ICA, Neuro fuzzy filter and Haar wavelet transform. The efficiency is measured in terms of SNR, SDR and Correlation factor.

Keywords: Electroencephalogram, ICA, Neurofuzzy Filter, Haar Transform, Multiwavelet Transform, SDR, SNR. Correlation Factor.

1. Introduction

Electroencephalogram is a medical imaging technique that reads scalp electrical activity generated by brain structures. Thus it helps in the analysis of actual health of the brain. In the EEG Electrical activity is recorded from the scalp surface after being picked up by metal electrodes and conductive media. The standard placement guide for the electrodes used in EEG measurement is the 10-20 system of electrode placement. Historically EEG is often divided into five major types of continuous rhythmic sinusoidal waves (δ , θ , α , β and γ) based on series of frequency range (1). The EEG is designed to amplify those electrical signals developed by the brain. However, additional electrical activity generated by the human body (physiological) and from external sources (extra physiological) is often also recorded in the EEG. This activity, collectively termed as artifacts, creates a problem in EEG analysis as it can very often mimic or obscure the underlying cerebral activity of interest. This problem could be eliminated by employing certain methods which can yield the original EEG. In this thesis, various methods are proposed to remove the Artifacts and retain the signal information. Artifact removal is the process of identifying and removing artifacts from brain signals (2). An artifact removal method should be able to remove the artifacts as well as keep the related neurological phenomenon intact.

2. Literature Survey

Artifact removal is the process of identifying and removing artifacts from brain signals. An artifact removal method should be able to remove the artifacts as well as keep the related neurological phenomenon intact (4) & (10).

- **Principle Component Analysis:** Lagerlund et al used Principal Component Analysis (PCA) to remove the artifacts from EEG. It outperformed the regression based methods. However, PCA cannot completely separate OA from EEG, when both the waveforms have similar voltage magnitudes. PCA decomposes the leads into uncorrelated, but not necessarily independent components that are spatially orthogonal and thus it cannot deal with higher-order statistical dependencies.
- **Canonical Correlation Analysis:** The Canonical Correlation Analysis (CCA) is developed to overcome the disadvantages of ICA. CCA is used as a Blind Source Separation technique (BSS) for artifacts removal from EEG signal. CCA based BSS method utilizes the temporal auto correlation in the source signal as a contrast function. It measures the linear relationship between two multi-dimensional variables, by finding two bases and bases are optimal with respect to correlation. CCA method has considerable amount of spectral error and thus it cannot be implemented in real time.
- **Regression Method:** It is based on complex regression analysis. It is suitable for handling transfer of EOG activity to EEG which can have different frequency and phase characteristics, because the regression formula is used in frequency domain. A complex

regression coefficient (P(jw))for EOG and EEG is calculated and then a common regression is removed from EEG. It is found that the complex regression coefficient (P(jw)) is used in the subtraction formula. This technique is demanding because it requires quantitative data relating to several thousand individuals. Implementing the data collection can be time consuming and expensive.

- **Subtraction Method:** Subtraction methods are based on the assumption that the measured EEG is a linear combination of an original EEG and a signal caused any sort of body movement E.g. Eye movement, called EOG (Electrooculogram) is a potential produced by movement of the eye or eyelid. The original EEG is hence recovered by subtracting separately recorded EOG from the measured EEG using appropriate weights. This method holds good for even the other type of Artifacts such as EMG, ECG, etc.

2.Materials and Methods

2.1. ICA Model

A simple mathematical representation of ICA model [6] is as follows: Consider a simple linear model which consists of N sources of T samples i.e. $S_i = [s(1)_i \dots s(t)_i \dots s_i(T)]$. The symbol t, here represents time but it may represent some other parameter like space. M weighted mixtures of the sources are observed as X, where $X_i = [x_i(1) \dots x_i(t) \dots x_i(T)]$. This can be represented as in Eqn. (1)

$$x = As + n \tag{1}$$

Where

$$X = \begin{bmatrix} x_1 \\ x_2 \\ \cdot \\ \cdot \\ \cdot \\ x_M \end{bmatrix}, S = \begin{bmatrix} s_1 \\ s_2 \\ \cdot \\ \cdot \\ \cdot \\ s_N \end{bmatrix} \text{ and } n = \begin{bmatrix} n_1 \\ n_2 \\ \cdot \\ \cdot \\ \cdot \\ n_K \end{bmatrix} \tag{2}$$

and **n** represents the Additive White Gaussian Noise (AWGN). It is assumed that there are at least as many observations as sources i.e., $M \geq N$. The $M \times N$ matrix **A** is represented as in Eqn(3)

$$A = \begin{bmatrix} a_{11} & a_{12} & \dots & a_{1N} \\ a_{21} & a_{22} & \dots & a_{2N} \\ \cdot & & & \\ \cdot & & & \\ a_{M1} & a_{M2} & \dots & a_{MN} \end{bmatrix} \quad (3)$$

A is called the mixing matrix. The estimation of the matrix **S** with knowledge of **X** is the linear source separation problem.

The number of observed signals, *m*, is greater than or equal to the number of latent variables, *n* (i.e. $m \geq n$). If $n > m$, we come to a special category of Independent Component Analysis called ICA with over-complete bases(6). In such a case the mixed signals do not have enough information to separate the independent components. There have been attempts to solve this particular problem but no rigorous proofs exist as of yet. If $m > n$ then there is redundancy in the mixed signals. The ICA model works ideally when $n = m$. The mixing matrix is of full column rank, which means that the rows of the mixing matrix are linearly independent. If the mixing matrix is not of full rank then the mixed signals will be linear multiples of one another. The propagation delay of the mixing medium is negligible. ICA has been used to correct for ocular artifacts, as well as artifacts generated by other sources. ICA is an extension of PCA which not only decorrelates but can also deal with higher order statistical dependencies. However, the ICA components lack the important variance maximization property possessed by the PCA components

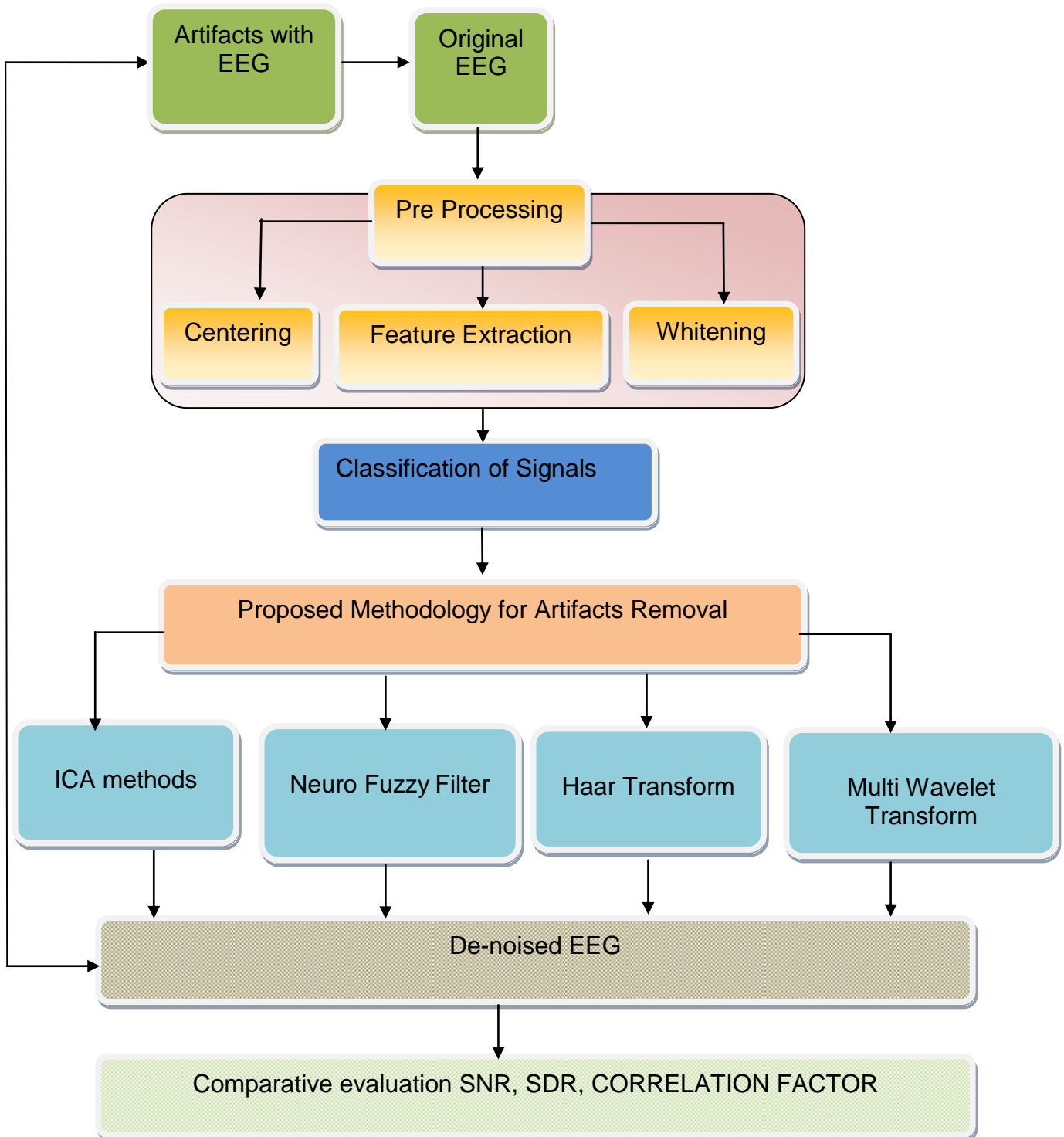


Fig. 1. General Block Diagram

2.2. Neuro-Fuzzy Filter

Neuro-Fuzzy framework is a mix of fake neural systems and the fuzzy rationale. It is cross breed framework. Each smart part has its own particular point of interest and weakness. For example on the off chance that we take the neural systems they are great at perceiving the examples of signs however not great at clarifying how they achieve their conclusions. Then again, the fluffy frameworks have a decent rationale behind their choice however can't naturally obtain the principles they used to make those decisions. The above reasons are the focal main impetus for hybridization. The systems are joined together to conquer the limits of the individual procedure. This helpful methodologies use neural system to make best utilization of specific parameters of fluff frameworks and the other way around. This neuro-fluffy methodology is extremely guaranteeing for non-straight albeit for the most part thought to be the acknowledgment of a fluffy framework through connectionist system(14).

Two conceivable models of neuro-fluffy frameworks are:

- In reaction to semantic explanations, the fluffy interface square gives an information vector to a multi-layer neural system. The neural system can be adjusted (prepared) to yield sought summon yields or choices.
- A multi-layered neural system drives the fluffy derivation component.

Neural systems are utilized to tune enrollment capacities of fuzzy frameworks that are utilized as choice making frameworks for controlling supplies . Al however fluffy rationale can encode master learning specifically utilizing tenets with phonetic marks, it normally takes a considerable measure of time to plan and tune the enrollment capacities which quantitatively characterize these semantic names. Neural system learning systems can computerize this methodology and considerably lessen advancement time and expense while enhancing execut.

2.3. Methodology of Neuro-fuzzy Filter

The computational process envisioned for fuzzy neural systems is as follows. It starts with the development of a "fuzzy neuron" based on the understanding of biological neuronal morphologies, followed by learning mechanisms [9]. This leads to the following three steps in a fuzzy neural computational process.

- Development of fuzzy neural models motivated by biological neurons.
- Models of synaptic connections which incorporates fuzziness in to neural network.
- Development of learning algorithms (the method of adjusting the synaptic weights).

The fig .2 gives the pictorial representation of the neuro-fuzzy filter. It includes subnet works. The circle denotes aggregation techniques. In this study, we have taken signals namely artifacts and delayed artifacts as inputs and measured EEG signal as target for training the Neuro-Fuzzy filter structure. We have used generalized bell type as membership function for tuning the parameters(11). The filter has the following structure,

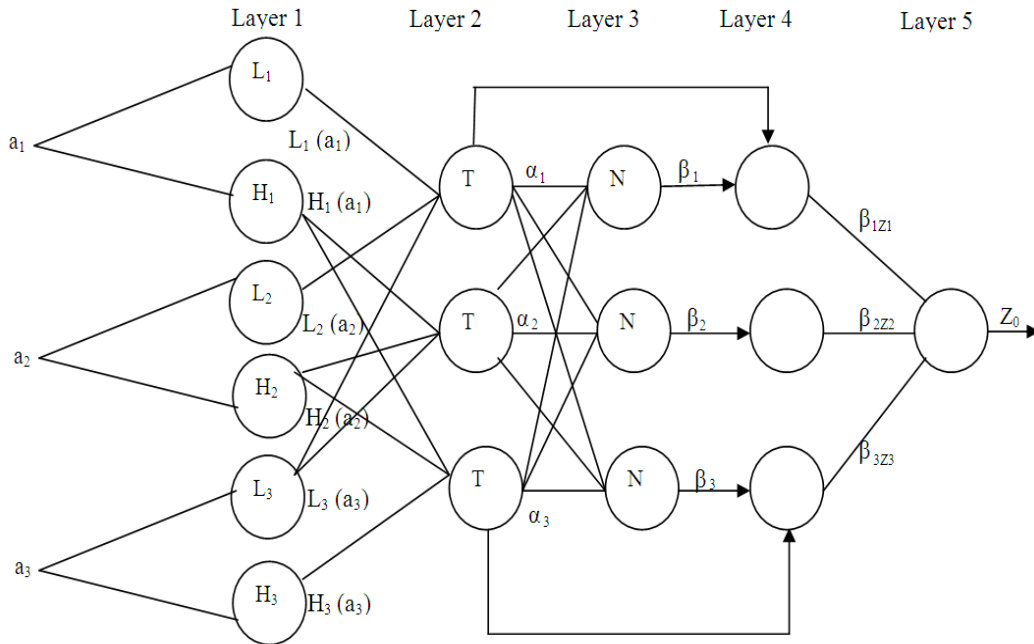


Fig. 2: Structure of Neuro-Fuzzy Filter

Layer 1: The output of the node is the degree to which the given input satisfies the linguistic label associated to this node .

Layer 2: Each node computes the firing strength of the associated rule. The nodes of this layer are called rule nodes.

The output of top neuron is:

$$\alpha_1 = L_1(a_1) \wedge L_2(a_2) \wedge L_3(a_3) \quad (4)$$

The output of the middle neuron is:

$$\alpha_2 = H_1(a_1) \wedge H_2(a_2) \wedge L_3(a_3) \quad (5)$$

And the output of the bottom neuron is:

$$\alpha_3 = H_1(a_1) \wedge H_2(a_2) \wedge H_3(a_3) \quad (6)$$

Layer 3: This layer is labeled as N to indicate the normalization of the firing levels. The output of the top, middle and bottom neuron is the normalized firing level of the corresponding rule:

$$\beta_1 = \frac{\alpha_1}{\alpha_1 - \alpha_2 + \alpha_3} \quad (7)$$

$$\beta_2 = \frac{\alpha_3}{\alpha_1 - \alpha_2 + \alpha_3} \quad (8)$$

$$\beta_3 = \frac{\alpha_3}{\alpha_1 - \alpha_2 + \alpha_3} \quad (9)$$

Layer 4: The output of the top, middle and bottomneuron is the product of the normalized firing Level.

$$\beta_{1z1} = \beta_1 \mathbf{V} \mathbf{B}^{-1} (\alpha_1) \quad (10)$$

$$\beta_{2z2} = \beta_2 \mathbf{B}^{-1} (\alpha_2) \quad (11)$$

$$\beta_{3z3} = \beta_3 \mathbf{S}^{-1} (\alpha_3) \quad (12)$$

Layer 5: The single node in this layer computesthe overall system output as the sum of all incoming signals.

$$z_0 = \beta_{1z1} + \beta_{3z2} + \beta_{3z3} \quad (13)$$

The various artifacts mixed in the EEG signal cannot be filtered directly because they pass through the human body and turn into an interference component. This interference component cannot be estimated directly because the spectrum of the EEG signal and the interference signal overlap each other and also because of the characteristics of noise and the EEG signal which vary with time.

2.4. Haar Transform

The Haar transform is the simplest of the wavelet transforms. This transform cross-multiplies a function against the Haar wavelet with various shifts and stretches, like the Fourier transform cross-multiplies a function against a sine wave with two phases and many stretches. The Haar transform can be thought of as a sampling process in which rows of the transformation matrix act as samples of finer and finer resolution (3). It provides shortest path and Time consumption is less. The Haar wavelet's mother wavelet function $\psi(t)$ can be described as

$$\psi(t) = \begin{cases} 1 & 0 \leq t < 1/2, \\ -1 & 1/2 \leq t < 1, \\ 1 & \text{otherwise.} \end{cases} \quad (14)$$

Its scaling function $\phi(t)$ can be described as

$$\phi(t) = \begin{cases} 1 & 1 \leq t < 2, \\ 0 & \text{otherwise.} \end{cases} \quad (15)$$

Any continuous real function can be approximated by linear combinations of $\phi(t)$, $\phi(2t)$, $\phi(4t)$ $\phi(2^k t)$... and their shifted functions. This extends to those function spaces where any function therein can be approximated by continuous functions.

- (i) Any continuous real function can be approximated by linear combinations of the constant function $\psi(t)$, $\psi(2t)$, $\psi(4t)$ $\psi(2^k t)$... and their shifted functions.
- (ii) Orthogonally in the form

$$\int_{-\infty}^{\infty} \psi(2^m t - n) \psi(2^{m_1} t - n_1) dt = \delta_{m, m_1} \delta_{n, n_1} \quad (16)$$

Here $\delta_{i,j}$ represents the Kronecker delta. The dual function of $\psi(t)$ is $\psi(t)$ itself.

- (iii) Wavelet/scaling functions with different scale m have a functional relationship:

$$\phi(t) = \phi(2t) + \phi(2t - 1) \quad (17)$$

By analysing the frequency spread of the EEG data that contained the Artefacts, researchers found that the difference in the frequency of the spikes caused due to rapid eye blink and the EEG signal could be used along with a simultaneous recording of the EOG to detect and remove these Artefacts(7). But correlation of the EEG and EOG is futile, especially because of the inherent corruption of EEG data by the restraint on the user's eye movements and blinks. EEG signal and EOG signal is taken at 1x4000. It is then sampled at 1x1000. The EEG recordings are contaminated by EOG signal. The EOG signal is a non-cortical activity. The eye and brain activities have physiologically separate sources, so the recorded EEG is a superposition of the true EEG and some portion of the EOG signal (12).

The proposed Algorithm in this paper involves the following steps:

- i) Apply Discrete Wavelet Transform to the contaminated EEG with Haar wavelet as the basis function to detect the Artefact zone.
- ii) Apply Stationary Wavelet Transform with Coif 3 as the basis function to the contaminated EEG with OA zones identified for removing Artefacts.

- iii) For each identified OA zone, select optimal threshold limit at each level of decomposition based on minimum Risk value and apply that to the soft-like thresholding function which best removes noise.
- iv) Apply inverse stationary wavelet transform to the threshold wavelet coefficients to obtain the de-noised EEG signal.

Haar wavelet transforms have single scaling function and single wavelet function. It is in the form of Square. So all the Signal to be analysed in the Square form only (8). It can better representation of Approximation only. Detailed representation is very less. To overcome this Disadvantage we move to Multiwavelet Transform. Multiwavelet transform Represent both approximation and Detailed better than wavelet transform.

3.Multiwavelet Transform

Multiwavelets are defined using several wavelets with several scaling functions. Multiwavelets have several advantages in comparison with scalar wavelet. The features such as compact support, orthogonally, symmetry, and high order approximation are known to be important in signal processing (5). A scalar wavelet cannot possess all these properties at the same time. On the other hand, a Multiwavelet system can simultaneously provide perfect reconstruction while preserving length (Orthogonally), good performance at the boundaries (via linear-phase symmetry), and a high order of approximation (vanishing moments) (JPEG2000 Overview). Thus Multiwavelet offer the possibility of superior performance and high degree of freedom for image processing applications, compared with scalar wavelets . A Multiwavelet with r scaling functions and r wavelet functions is said to have multiplicity r. When r = 1, one scaling function and one wavelet function, the Multiwavelet system reduces to the scalar wavelet system. Multiwavelets have two or more scaling functions and wavelet functions (13). For notational difference the set of scaling functions can be written using the vector notation

$$\Phi(t) = [\phi_1(t), \phi_2(t), \dots, \phi_r(t)]^T \tag{18}$$

Where, $\phi(t)$ is called the multi-scaling function. Likewise the Multiwavelet function is defined from the set of wavelet function

$$\psi(t) = [\psi_1(t), \psi_2(t), \dots, \psi_r(t)]^T \tag{19}$$

r=1, $\psi(t)$ is called a scalar wavelet or simply called wavelet.

Multiwavelets differ from scalar wavelet systems in requiring two or more input streams to the Multiwavelet filter bank. Multiwavelets are an extension of the scalar wavelet to the vector case. As in the scalar wavelet case, the theory of Multiwavelet is based on the idea of multiresolution analysis (MRA). The difference is that Multiwavelet has several scaling functions. For Multiwavelets, the notion of MRA is the same except that now a basis for V_0 and V_1 is generated by translates of N scaling functions.

$$\phi_1(t-k), \phi_2(t-k), \dots, \phi_N(t-k) \tag{20}$$

The multi scaling function and the Multiwavelet function will satisfy matrix dilation as in the following equations.

$$\phi(t) = \sqrt{2} \sum_{k=-\infty}^{\infty} H_k \phi(2t-k) \quad (21)$$

$$\Psi(t) = \sqrt{2} \sum_{k=-\infty}^{\infty} G_k \phi(2t-k) \quad (22)$$

The filter coefficients H_k and G_k are N by N matrices instead of scalar. Corresponding to each Multiwavelet system, there is a matrix-valued multi-rate filter bank. A Multiwavelet filter bank has “taps” that are $N \times N$ matrices. The 4-coefficient symmetric Multiwavelet filter bank whose low pass filter is given by the four $N \times N$ matrices named C . Unlike a scalar 2-band Para unitary filter bank, the corresponding high pass filter specified by the four $N \times N$ matrices named D , cannot be obtained simply as an “alternating flip” of the low pass filter; the wavelet filters D must be designed. The resulting N channel, $N \times N$ matrix filter bank operates on N input data

Streams, filtering them into $2N$ output streams, each of which is down sampled by a factor of 2.

4. Multiwavelet Denoising Technique

Suppose one has to measure a signal on which an external noise is super imposed. EEG the true signal $S(t)$ and the external noise $\epsilon(t)$, So that the measured signal can be written in the form

$$X(t) = S(t) + \epsilon(t) \quad (23)$$

The only assumptions needed are that $S(t)$ and $\epsilon(t)$ are uncorrelated and are stationary processes, and can be written as equation 23. Thresholding is a technique used for signal and image de-noising. When we decompose a signal using the wavelet transform, we are left with a set of wavelet coefficients that correlates to the high frequency sub bands (9). These high frequency sub bands consist of the details in the data set. If these details are small enough, they might be omitted without substantially affecting the main features of the data set. The de-noising of EEG signal is carried out by using different combinations of threshold limit, thresholding function and window sizes. Choice of threshold limit and thresholding function is a crucial step in the denoising procedure, as it should not remove the original signal coefficients leading to loss of critical information in the analyzed data (15). In this paper, the following thresholding (statistical empirical) formula is used for calculating the thresholding limits. This formula produces better de-noised results than, which is applied to the entire length of the signal. Threshold based on Statistics of the signal.

Threshold Value

$$T_k = N \times \left(\frac{\bar{x} - \zeta}{\bar{x} + \zeta} \right) \quad (24)$$

Window Length=10 Seconds

Where N is a Positive Integer, ranging from 100 to 150

\bar{x} - Mean of all samples

ζ - Standard deviation of all samples

5. Results & Discussion

EEG data with artifacts are taken from [http:// www. sccn.ucsd.edu/~arno/famzdata/ publicly_avialble_EEG_data.html](http://www.sccn.ucsd.edu/~arno/famzdata/publicly_avialble_EEG_data.html) for testing the proposed methods. The effect of artifacts is dominant in the Frontal and fronto –polar channels like Fp1, Fp2, F7, F8. Hence it is Sufficient to apply the method to these channels. The proposed methods results are shown in Fig 3. In the case of multiwavelet transform the denoising of EEG signals is carried out by using threshold limit, threshold function and window Size. Choice of threshold limit and thresholding function is a crucial step in the de nosing procedure, as it should not remove the original signal coefficients leading to loss of critical information in the Analyzed data.

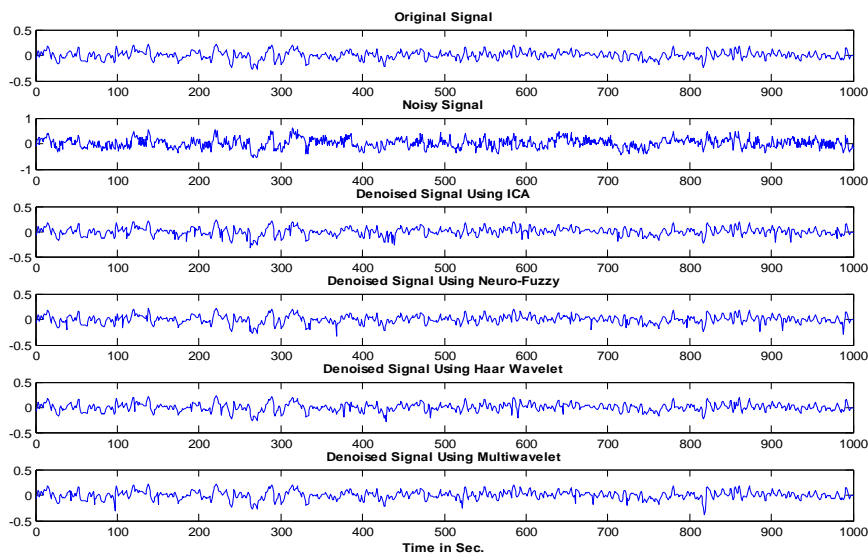


Fig. 3.Original, Noisy & Denoised Signal using Various Artifacts Removal Method

5.1. Comparative Analysis of SNR Value using Various Methods

The Signal to Noise Ratio of denoised Signal (Corrected EEG) using proposed methods ICA, Neuro fuzzy filter, Haar wavelet transform and Multiwavelet transform is summarized in Table.I. Conclude that the ICA method SNR value is higher than contaminated signal. Neuro-fuzzy filter

SNR value is higher than ICA. Haar wavelet SNR value is higher than Neuro fuzzy filter. Finally multiwavelet achieves high SNR value compare with other methods.

Table I: SNR Values for Proposed Methods

Trials	Contaminated Signal SNR (dB)	SNR in dB for proposed Methods			
		Using ICA Method (JADE)	Neuro fuzzy Filter	Haar wavelet Transform	Multi wavelet Transform (SA4 Filter)
Trial 1	5.5243	9.9500	14.2044	18.6276	27.9943
Trial 2	7.2792	12.3495	21.2361	25.3578	34.9961
Trial 3	8.6072	16.6945	22.6764	26.4352	35.2639
Trial 4	9.3072	17.3363	24.1735	28.5073	36.8562
Trial 5	8.3030	16.7890	23.5227	27.9367	35.3810

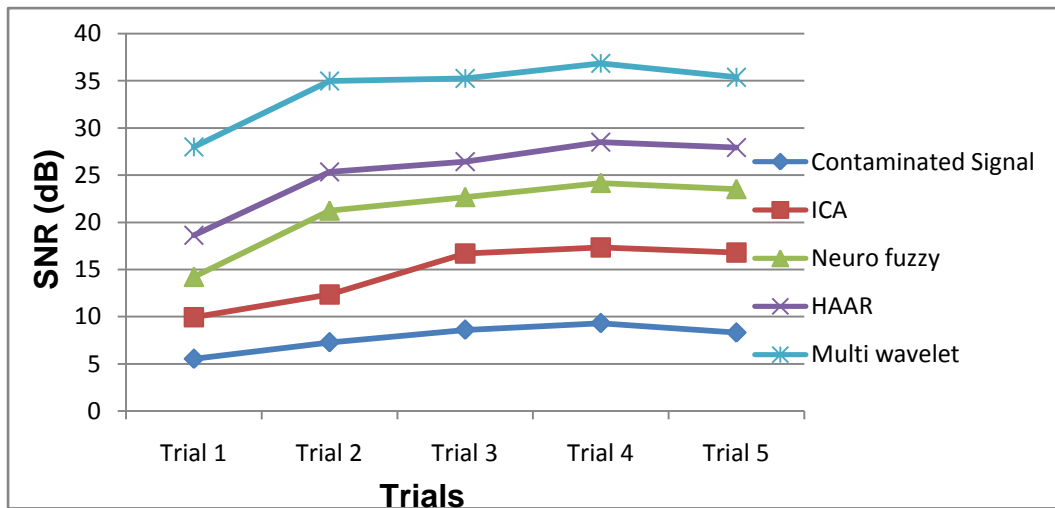


Fig.4 SNR Curve for Contaminated Signal and Proposed Artifacts Removal Methods

The signal to noise ratio curve for various methods along with contaminated signal is shown in Fig 4. This curve clearly shows that the Multiwavelet transform proves better result than other methods.

5.2. Comparative Analysis of Correlation Factor for Various Methods

Correlation Factor (CF) of denoised signal (Corrected EEG) using proposed methods ICA, Neuro fuzzy filter, Haar wavelet transform and Multiwavelet transform is summarized in Table.II. Conclude that the adaptive filter CF value is higher than contaminated signal. Neuro-fuzzy filter CF value is higher than adaptive filter. Haar wavelet CF value is higher than Neuro fuzzy filter. Finally multiwavelet achieves high CF value compare with other methods.

Table II. Correlation Factor Values for Proposed Methods

Trials	Contaminated Signal Correlation Factor	Correlation factor for proposed Methods			
		ICA Method	Neuro fuzzy Filter	Haar wavelet Transform	Multi wavelet Transform (SA4 Filter)
Trial 1	0.2060	0.9535	0.9814	0.9932	0.9992
Trial 2	0.6775	0.9895	0.9963	0.9986	0.9998
Trial 3	0.6956	0.9910	0.9957	0.9986	0.9999
Trial 4	0.8042	0.9898	0.9962	0.9986	0.9998
Trial 5	0.3395	0.9728	0.9890	0.9960	0.9995

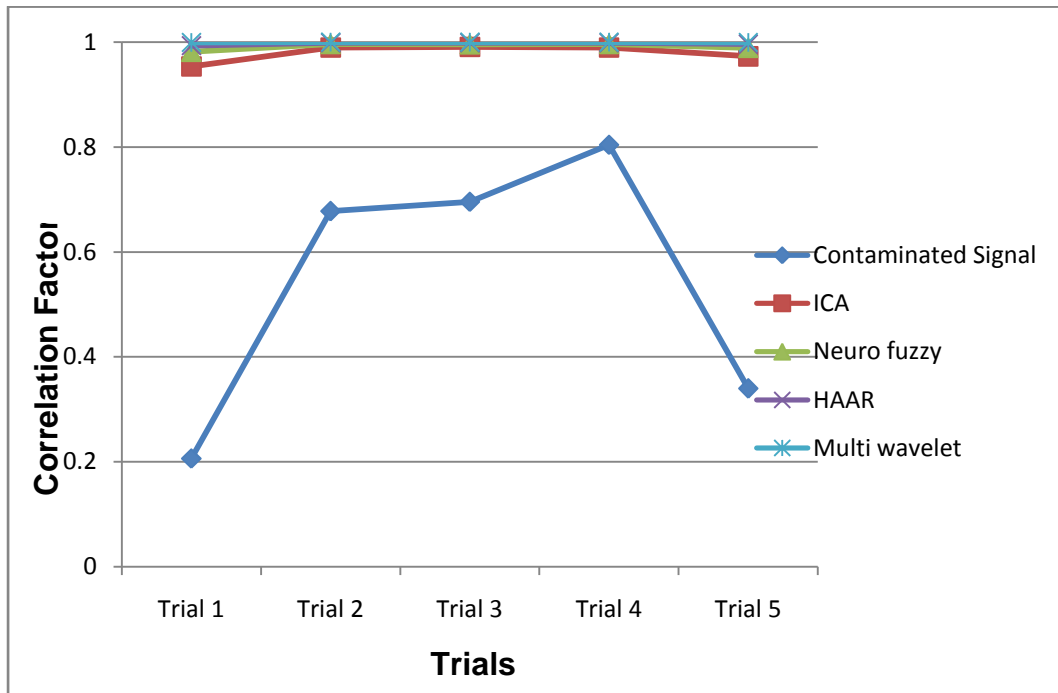


Fig. 5.CF Curve for Contaminated Signal and Proposed Artifacts Removal Methods

The Correlation factor curve for various methods along with contaminated signal is shown in Fig.5. This curve clearly shows that the Multiwavelet transform proves better result than other methods.

5.3. Comparative Analysis of Signal Distortion Ratio for various Method

The Signal Distortion Ratio (SDR) of denoised signal (Corrected EEG) using proposed methods ICA, Neuro fuzzy filter, Haar wavelet transform and Multiwavelet transform is shown in Table III. Conclude that the ICA method SDR value is higher than contaminated signal. Neuro-fuzzy filter SDR value is higher than ICA. Haar wavelet SDR value is higher than Neuro fuzzy filter. Finally multiwavelet achieves high SDR value compare with other methods.

Table III: Signal Distortion Ratio For Proposed Methods

Trials	SDR for contaminated signal	SDR for proposed Methods			
		ICA Method	Neuro fuzzy Filter	Haar wavelet Transform	Multi wavelet Transform (SA4 Filter)
Trial 1	0.2803	9.8855	26.3292	72.9060	172.060
Trial 2	1.3425	46.7144	132.9265	343.3833	634.460
Trial 3	1.4479	54.1539	116.8538	349.5577	674.910
Trial 4	1.3512	47.7420	131.0229	355.4125	614.410
Trial 5	0.4674	17.1771	44.9023	124.0718	219.718

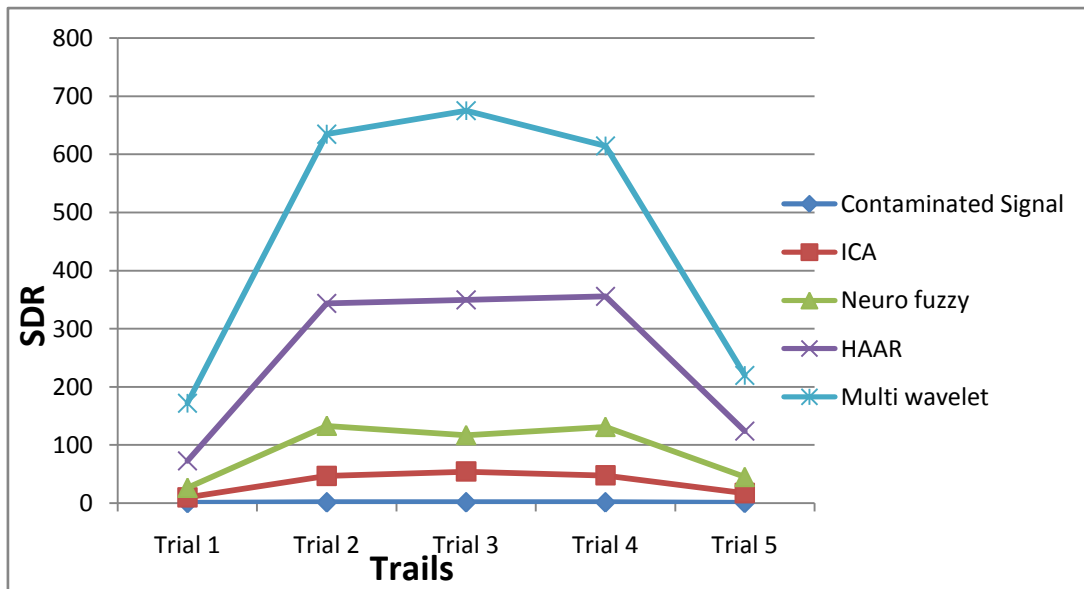


Fig. 6.SDR Curve for Contaminated Signal and proposed Artifacts Removal Methods

The SDR curve for various proposed methods along with contaminated signal is shown in fig 6. This curve clearly shows that the Multiwavelet transform proves better result than other methods.

6. Conclusion

In recent years researchers have used both ICA algorithms and Wavelet transforms to denoise EEG signals. In this paper we propose a comparative evaluation method for ICA, Neuro fuzzy filter, Wavelet transform & Multi wavelet Transform. From the Experiment can conclude the following,

- It can be seen from the experiments that it can successfully separate noise from EEG signals.

- Multiwavelet method has outperformed ICA, Neuro fuzzy filter and Wavelet Transform as far as SNR, SDR and Correlation factor concerned.
- It can be seen from the experiments the powers of the spectral components have been fully retained.
- Based on these results it can be concluded that Multiwavelet transform has an overall performance which is better than all three methods like IJADE, Haar transform and Neuro fuzzy filter, i.e. Multiwavelet is the most consistent and robust artifacts removal method.

References

- N. O.S.B. Karait, S. M. Shamsuddin and R. Sudirman, Swarm Negative Selection Algorithm for Electroencephalogram Signals Classification, 5:995-1002. DOI: 10.3844/jcssp, 995.1002, (2009).
- M.M.Teplan, Fundamentals of EEG Measurement, Measurement and science review, 2, 1-11, (2002).
- Alfaouri, M. and K. Daqrouq, ECG Signal De-noising By Wavelet Transform Thresholding. American Journal of Applied Science. 5: 276-281, (2008).
- W. M. Bukhari, W. Daud, R. Sudirman and C. Omar, Identification of Electrooculography Signals, (2011).
- V. Krishnaveni, S. Jayaraman, L. Anitha, K. Ramadoss, Removal of Artefacts from EEG using Adaptive thresholding of Wavelet coefficients, Journal of Neural Engineering, 3, 338-346, (2006).
- Aapo Hyvarinen. Independent Component Analysis: Algorithms and Applications, IEEE transactions on Neural Networks, 13, 411-430, (2000).
- H. om and M. Biswas, An Improved De-noising Method based on wavelet Thresholding (IIDMWT), Journal of Signal and Information Processing (USA), 3(1), 109-116, (2012).
- B.C.Rao and M.M.Latha, Selective Neighboring wavelet Coefficients Approach for image De-noising, International Journal of Computer Science and Communication, 2(1), 73-77, (2011).
- J. Gao, H. Sultan, J. Hu and W. W. Tung, "De-noising nonlinear time series by adaptive filtering and wavelet shrinkage: a comparison," IEEE Sig. Proc. Let., 17(3), 237-240, (2010).
- S. S. Patil and M. K. Pawar, "Quality advancement of EEG by wavelet de-noising for biomedical analysis," IEEE International Conference on Communication, Information & Computing Technology (ICCICT), 1-6, (2012).

- H. Leung, K. Schindler, A.Y. Chan, A.Y. Lau, K.L. Leung, E.H. Ng, K.S. Wong, "Wavelet-de-noising of electroencephalogram and the absolute slope method: A new tool to improve electroencephalographic localization and lateralization," *Clin Neurophysiol*,20(7), 1273-1281,(2009).
- S.K. Mohideen, S.A.Perumal and M.M. Sathik, Image De-Noising using Discrete Wavelet Transform,*International Journal of Computer Science and Network Security*,8(1), 213-216,(2008).
- Karmurl Hassan Talkuder and Koichi Harda,Haar Wavelet based approach for image compression & quality assessment of compressed image, *IAENG,IJAM*,(2007).
- Mu'azu, M.B.Forecasting and modeling statistical phenomena using neuro-fuzzy logic: A Case study of rainfall forecasting for Zaria. PhD dissertation. Department of Electrical Engineering. A B U, Zaria.2, 95-105,117-120,134-136, (2006).
- S. Kothar Mohideen, Dr.S.Arumuga Perumal, Dr.M. Mohamed Sathik, Image De-noising using Discrete wavelet transform *International Journal of computer Science and Network security(IJCSNS)*,8(1),(2008).



Asian Research Consortium

Asian Journal of Research in Social Sciences and Humanities
Vol. 6, No. 8, August 2016, pp. 179-195.

ISSN 2249-7315

A Journal Indexed in Indian Citation Index

DOI NUMBER: 10.5958/2249-7315.2016.00602.X

Category: Science and Technology

Asian Journal
of Research in
Social Sciences
and
Humanities

www.ajsh.com

Proficient Technique to Communicate and Detect Emotion of Differently - Abled Persons using Sensor Devices and Electroencephalogram Signals

Dr. B. Paulchamy*; Dr. J. Jaya**

*Professor & Head,

Department of ECE,

Hindusthan Institute of Technology,

Coimbatore, India.

**Principal,

Akshaya College of Engineering & Technology,

Coimbatore, India.

Abstract

This paper presents an effective communication method for differently-abled persons. Emotion is an important aspect in the interaction between humans. It is fundamental to human experience and rational decision-making. Generally, normal people can easily interact with one another but Sign language is the only means of communication for those who are dumb and deaf. This paper describes the design and working of a system which is used to communicate and to detect emotions of dumb and deaf. Hence by this methodology differently-abled people can able to interact with each other and also with the normal people. The dumb people use their standard sign language which is not recognizable by common people. For This purpose we are converting the sign language into voice which is easily understandable by normal people. Sensors and electrodes are used to detect the sign language and emotions that are processed by microcontroller (ATMEGA) where the in-built ADC converts the given analog signals into digital form. Then this digital signal is transmitted to PC via zig-bee. The PC produces the voice output for sign language (Differently abled to Normal people) and voice is translated into text form(normal people to Differently-abled) and their corresponding EEG signal determines the state of mind(Happy, Sad, Frustrated, etc.)

Keywords: Flux Sensor, Speech Synthesis, EEG, ATMEGA, Amplifier.

1. Introduction

“Speech” and “gestures” are the expressions, which are mostly used in communication between human beings. Learning of their use begins with the first years of life. Research is in progress that aims to integrate gesture as an expression in Human- Computer Interaction (HCI).

In human communication, the use of speech and gestures is completely coordinated. Machine gesture and sign language recognition is about recognition of gestures and sign language using computers. A number of hardware techniques are used for gathering information about body positioning; typically either image-based (using cameras, moving lights etc) or device-based (using instrumented gloves, position trackers etc.), although hybrids are beginning to come about [1], [2], [3].

However, getting the data is only the first step. The second step, that of recognizing the sign or gesture once it has been captured is much more challenging, especially in a continuous stream. In fact currently, this is the focus of the research. This research paper analyses the data from an instrumented data glove for use in recognition of some signs and gestures and the third step is to determine the neuronal brain activity by the electrodes. The Electroencephalogram (EEG) is one of the useful bio signals detect the human emotions. This paper also discusses research conducted to determine the changes in the electrical activity of the human brain related to distinct emotions. Thus the statistical learning method that can provide very stable and successful emotional classification performance over six emotional states.

The acquired signals are processed by the microcontroller which in-turn transmit these signals through Zig-bee protocol to interface with PC. Hence this system is developed for recognizing emotions, signs and their conversion into speech and text (vice-versa). The results will show that despite the noise and accuracy constraints of the equipment, the reasonable accuracy rates have been achieved.

A wonderful and latest survey of the work done in this field is described in reference [4]. Reference [5] and [6] discuss the gesture recognition for human robot interaction and human robot symbiosis. Reference [7] offers a novel “signal-level” perspective by exploring prosodic phenomena of spontaneous gesture and speech co-production. A comprehensive framework is presented that addresses two important problems in gesture recognition systems in [8]. An augmented reality tool for vision based hand gesture recognition in a camera-projector system is described in reference [9]. Continuous hand gesture recognition requires the detection of gestures in a video stream and their classification.

Before a system can recognize the face and hand poses, it must possess knowledge of the characteristic feature of these poses. This means that the system designer must either build the necessary discriminating rules into the system or the system must learn them. To adapt to new users and new hand poses the system must be able to perceive and extract relevant properties from the unknown faces and hand poses, find common among them and formulate discrimination criteria consistent with the goal of the recognition process.[10]

Many gesture can be described by the motion pattern generated by the upper body. The spatial movement of the hands, in particular, contain meaningful information about a performed gesture. We therefore focused on the time series of the hands movement as a basis for our gesture recognition system. It is known to be difficult to reconstruct the 3D configuration of the human body parts if a 2D image is the only data source.[11]

2. Materials and Methods

This research paper analyses the data from an instrumented flex and accelerometer sensor for use in recognition of some signs and gestures. A system is developed for recognizing these signs and their conversion into speech. The results will show that despite the noise and accuracy constraints of the equipment, the reasonable accuracy rates have been achieved.

The Electroencephalogram (EEG) is one of the useful bio signals detect the human emotions. This paper also discusses research conducted to determine the changes in the electrical activity of the human brain related to distinct emotions. Thus the statistical learning method can provide very stable and successful emotional classification performance over six emotional states.

Block diagram of the system is shown Fig.1.

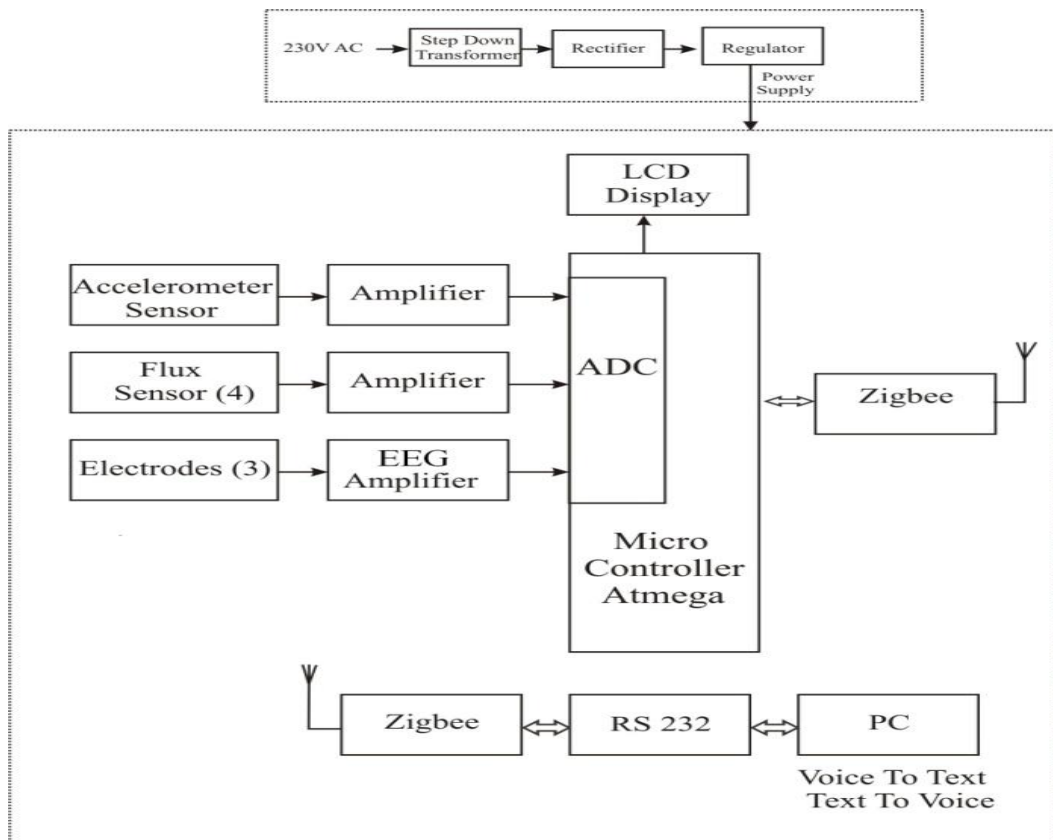


Fig. 1.Overall Block Diagram

The system is consisted of following modules:

- Data Glove
- Tilt detection
- Gesture detection
- Speech Synthesis
- LCD Display

Data glove is consisted of two sensors; bend sensors and tilt sensor. The output of the tilt sensors is detected by the tilt detection module, while the output of the bend sensors, and the overall gesture of the hand are detected by the gesture detection module. The gesture detection module gives an 8-bit address to speech synthesis module; 8-bit address is different for each gesture. Speech Synthesis module speaks the message respective to address received by it.

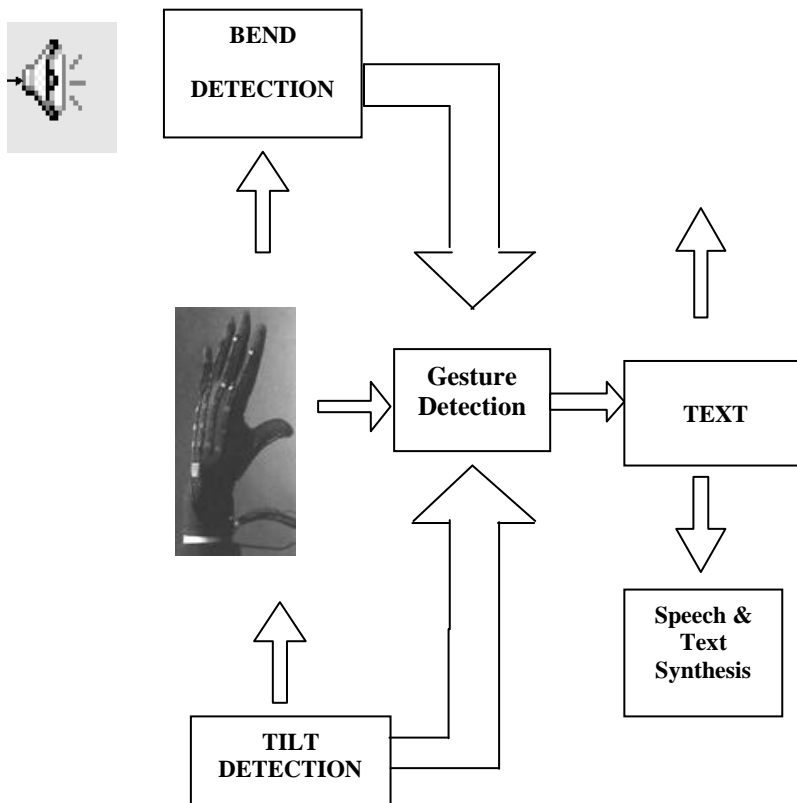


Fig.2. Block Diagram of the System

3. System Description

3.1 Data Glove: Data glove consisted of two sensors: flux sensors and accelerometer.



Fig.3. Photo Shot of our Designed Data Glove

3.2 Flux Sensor: Flexion sensor, (from Latin *flectere*, 'to bend') also called bend sensors, measure the amount of deflection caused by bending the sensor. There are various ways of sensing deflection, from strain-gauges to hall-effect sensors. The three most common types of flexion sensors are:

- Conductive ink-based
- Fiber Optics
- Conductive Fabric/thread/polymer-based



Fig. 4.Flux Sensor

A property of bend sensors worth noting is that bending the sensor at one point to a prescribed angle is not the most effective use of the sensor. As well, bending the sensor at one point to more than 90° may permanently damage the sensor. Instead, bend the sensor around a radius of curvature. The smaller the radius of curvature and the more the whole length of the sensor is involved in the deflection, the greater the resistance will be (which will be much greater than the resistance achieved if the sensor is fixed at one end and bent sharply to a high degree). In fact, Systems define the sensing parameter as “flex angle multiplied by radius”.

3.3 Accelerometer: One of the most common inertial sensors is the accelerometer, a dynamic sensor capable of a vast range of sensing. An accelerometer is an electromechanical device that will measure acceleration forces. These forces may be static, like the constant force of gravity pulling at your feet, or they could be dynamic -caused by moving or vibrating the accelerometer.ump over the lazy dog. The quick brown fox jump over the lazy dog. The quick brown fox jump over the lazy dog. The quick brown fox jump over the lazy dog. The quick brown fox jump over the lazy dog.

An accelerometer is a device that measures the vibration, or acceleration of motion of a structure. The force caused by vibration or a change in motion (acceleration) causes the mass to "squeeze" the piezoelectric material which produces an electrical charge that is proportional to the force, and the mass is a constant, then the charge is also proportional to the acceleration. Accelerometers are available that can measure acceleration in one, two or three orthogonal axes. They are typically used in one of the three modes:

- As an inertial measurement of velocity and position
- As a sensor of inclination, tilt, or orientation in 2 or 3 dimensions, as referenced from the acceleration of gravity ($1\text{ g} = 9.8\text{m/s}^2$)
- As a vibration or impact (shock) sensor.

There are considerable advantages to using an analog accelerometer as opposed to an inclinometer such as a liquid tilt sensor – inclinometers tend to output binary information (indicating a state of on or off), thus it is only possible to detect when the tilt has exceeded some thresholding angle. Most accelerometers are Micro-Electro-Mechanical Sensors (MEMS). The basic principle of operation behind the MEMS accelerometer is the displacement of a small proof mass etched into the silicon surface of the integrated circuit and suspended by small beams. Consistent with Newton's second law of motion ($F = ma$), as an acceleration is applied to the device, a force develops which displaces the mass. The support beams act as a spring, and the fluid (usually air) trapped inside the IC acts as a damper, resulting in a second order lumped physical system. This is the source of the limited operational bandwidth and non-uniform frequency response of accelerometers.

3.4 Tilt Detection: The output, which is obtained from the accelerometers after amplification, is an analog output. To deal with this analog output, and to make it useful for the further use, it is required to change it into some form, which is detectable for the microcontroller. The analog output of the accelerometer is converted into digital form. This Gesture Vocalizer system is a dual axis

system, which can detect the tilt of the hand in two axes. A dual channel ADC can be used to convert the outputs of the accelerometers in to digital form.

The basic function of this module is to detect the tilting of the hand and sending some binary data against meaningful gestures, to the bend detection module.

Now the output of the accelerometers is converted into the digital form this output is useful, in a sense that it is detectable by the microcontroller, and useful for the further use.

Next step for the microcontroller is to check the data from the ADC's. The microcontroller checks whether the data received from the ADC's is some meaningful data, or useless one. Meaningful means that the tilt of the hand is some meaningful tilt and is signaling some defined gesture, or a part of the gesture, because gesture means a complete motion of the hand in which the bending of the finger is also involved. The microcontroller compares the values received from the ADC's with the predefined values, which are present in the memory of the microcontroller and on the basis of this comparison the microcontroller decides that, is the gesture a meaningful gesture.

If the hand is signaling a meaningful gesture then the microcontroller moves toward the next step. The next step of the microcontroller is to send eight bit binary data to the main "bend detection" module. The eight-bit code is different for every valid gesture. On the basis of this code, which is, sent by the tilt detection module, the "bend detection" module checks the gestures as a whole, and takes some decisions. The "bend detection module" sends eight bit data to the speech synthesises module that knows the meaning of each data.

3.5 Bend Detection: The bend detection module is the most important and the core part of the paper. This module is based on a microcontroller-controlled circuitry.

Flexion sensors typically consist of two layers of conductive material with a layer of resistive material in between. It is mostly sandwiched in between layers of more rugged material, e.g. Neoprene. As pressure is applied (directly or by bending) the two layers of conductive material get pushed closer together and the resistance of the sensor decreases. This sensing mechanism is similar to force-sensitive resistors.

These types of sensors are pressure sensors which also sense deflection (pressure as a function of deflection): bending the sensor across an angle of a rigid structure results in stretch of the sensor material which exerts pressure onto the sensor. It is this pressure that is measured.

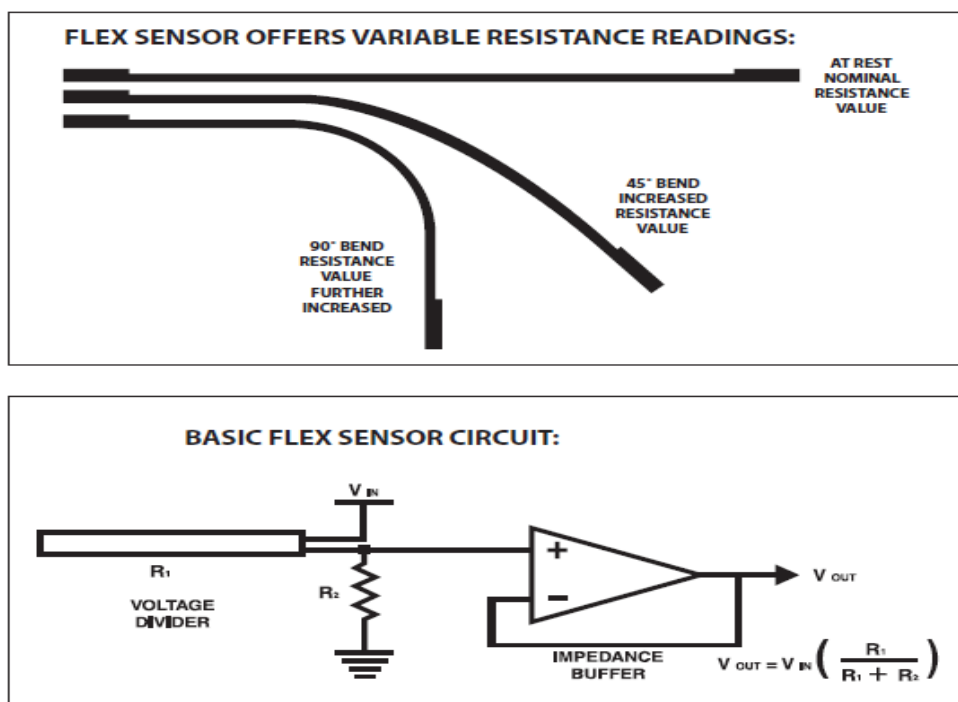


Fig.5. Circuit Diagram of Flux Sensor

In this module one microcontroller is used and three ports of this microcontroller are in use. Port zero takes the input from the five bend sensors, which is to be processed. The port one takes data from the tilt detection module and the port three gives final data, which represents some meaningful gesture to the speech synthesis module.

At first the microcontroller takes input of the five-bend sensor at its port zero. Output of the five bend sensors is given at the separate pin. Microcontroller deals with the bend sensors one by one. First of all the microcontroller checks the output of the first bend sensor, and calculates its pulse width, after the calculation of the pulse width of the first bend sensor the microcontroller saves its output, and then moves towards the second bend sensor and calculates its pulse width in the similar manner, and keeps on calculating the pulse width of the bend sensors one by one, having calculated the pulse width of the outputs of the five bend sensors, the microcontroller moves towards the next step of the module, i.e. gesture detection.

Gesture detection is the most important part of this module. The pulse width calculation part of the module calculates the pulse width of the signal obtained from the bend sensors at a regular interval. Even a little bend of the finger is detected at this stage of the system, so the bending of the figure has infinite levels of bends, and the system is very sensitive to the bending of the finger. Now the bending of each finger is quantized into ten levels. At any stage, the finger must be at one of these levels, and it can easily be determined how much the finger is bended. So far the individual bending of each finger is captured. System knows how much each finger is bended. Now the next step is to combine the movement of each finger and name it a particular gesture of the hand.

Now the system reads the movements of five fingers as a whole, rather than reading the individual finger. Having read bending of the fingers, the system checks whether the bend is some meaningful bend, or a useless or undefined bend. If the bending of the fingers gives some meaningful gesture, then system moves towards the next step.

In the next step the system checks the data, which was sent by tilt detection module at port one of the microcontroller. The data sent by this module shows whether the tilt of the hand is giving some meaningful gesture or it is undefined. If the tilt of the hand is also meaningful then it means the gesture as a whole is a meaningful gesture. So far it is detected by the system whether the gesture given by hand is some meaningful gesture, or a useless one. If the gesture is meaningful the system sends an eight bit data to the speech synthesis module. This eight bit data can represent 256 ($2^8=256$) different gestures. The gesture detection module assigns a different 8bit code to each gesture.

3.6 EEG Signal Analysis: EEG measurement is non invasive and inexpensive, have a very high sensitivity to receive information about the internal (endogenous) changes of brain state these data are particularly suited for studies on brain mechanisms of cognitive-emotional information processing which occurs in the millisecond range.[12]

Nonverbal information appearing in human facial expressions, gestures, and voice plays an important role in human communication. Especially, by using information of emotion and/or affection the people can communicate with each other more smoothly [13]. This means that non verbal communication is basis of human communication. In addition to this human-human communication, it is also important that human-human communication via computer and the communication between human - machines are more and more common one in the recent field of research. In order to understand the communication between man-machine, we discussed the emotion as interface between the human and machine through the EEG signals.

3.7 Emotions: Emotions and their expression are key element in social interactions, being used as mechanisms for signaling, directing attention, motivating and controlling interactions, situation assessment, construction of self- and other's image, expectation formation, inter subjectivity, etc[14].

Recently, a constellation of findings, from neuroscience, psychology, and cognitive science, suggests that emotion plays surprising critical roles in rational and intelligent behaviour. When we are happy, our perception is biased at selecting happy events, likewise for negative emotions. Similarly, while making decisions, users are often influenced by their affective states. Reading a text while experiencing a negatively valence emotional state of often leads to very different interpretation than reading the same text while in a positive state [15].

It is not only tightly intervened neurologically with the mechanisms responsible for cognition, but that they also play a central role in decision making, problem solving, communicating, negotiating, and adapting to unpredictable environments. Emotion consists of more than its outward physical expression: it also consists of internal feelings and thoughts, as well as other internal process of which the person experiencing the emotion may not be aware [16]. Individual emotional state may

be influenced by kinds of situations, and different people have different subjective emotional experiences even response to the same stimulus [17].

The human emotions are basically classified into three types: Motivational (Thirst, Hunger, Pain, Mood), Basic (Happy, Sad, Fear, Disgust, Anger, Surprise) and Self Conscious or Social (Shame, Embarrassment, Pride, Guilt)[16]. Pattern recognition efforts aimed at finding physiological correlates, focusing on t-tests or Analysis of Variance (ANOVA) comparisons and combining data over many subjects, where each was measured for a relatively small amount of time [18].

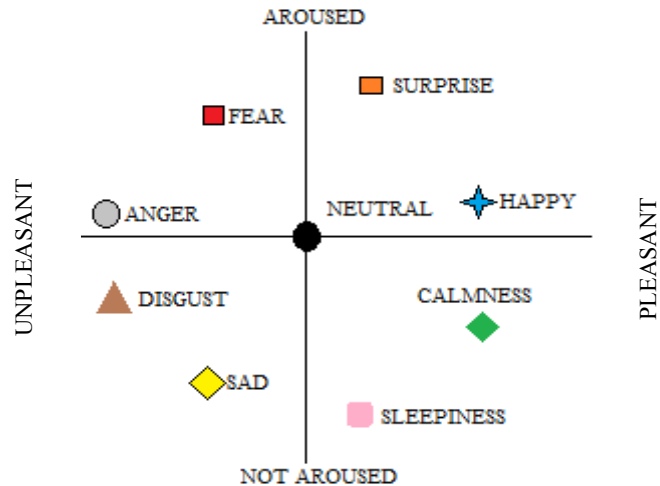


Fig.6.Russel Model for Emotion

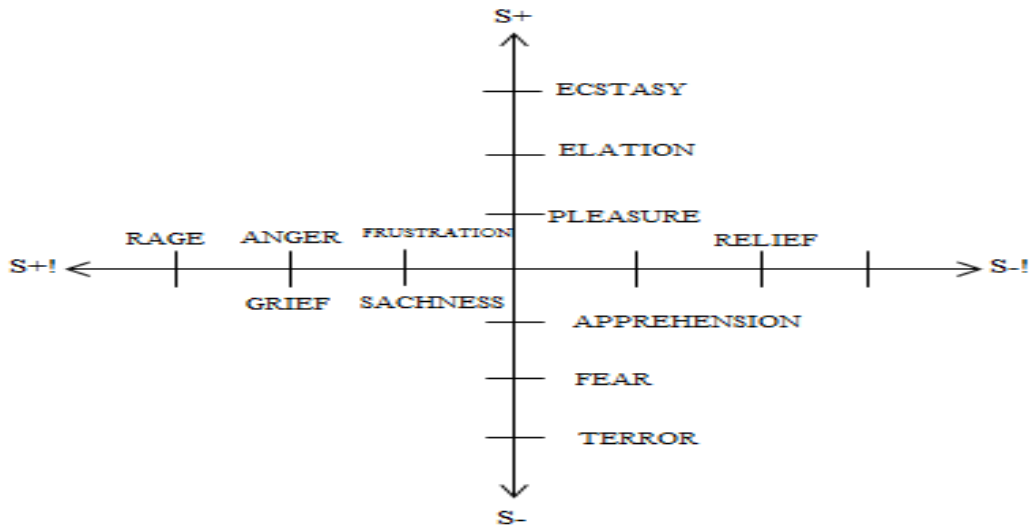


Fig.7.Discussion Model for Rolls Theory of Emotion

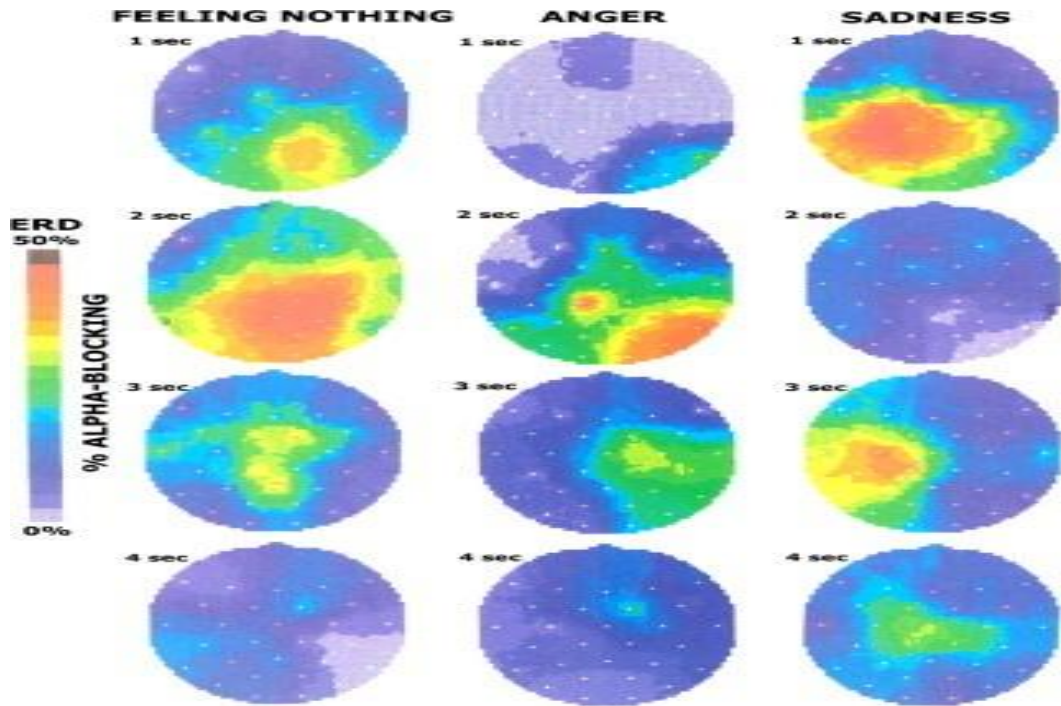


Fig.8 Brain Activity for Normal State, Angry and Sad

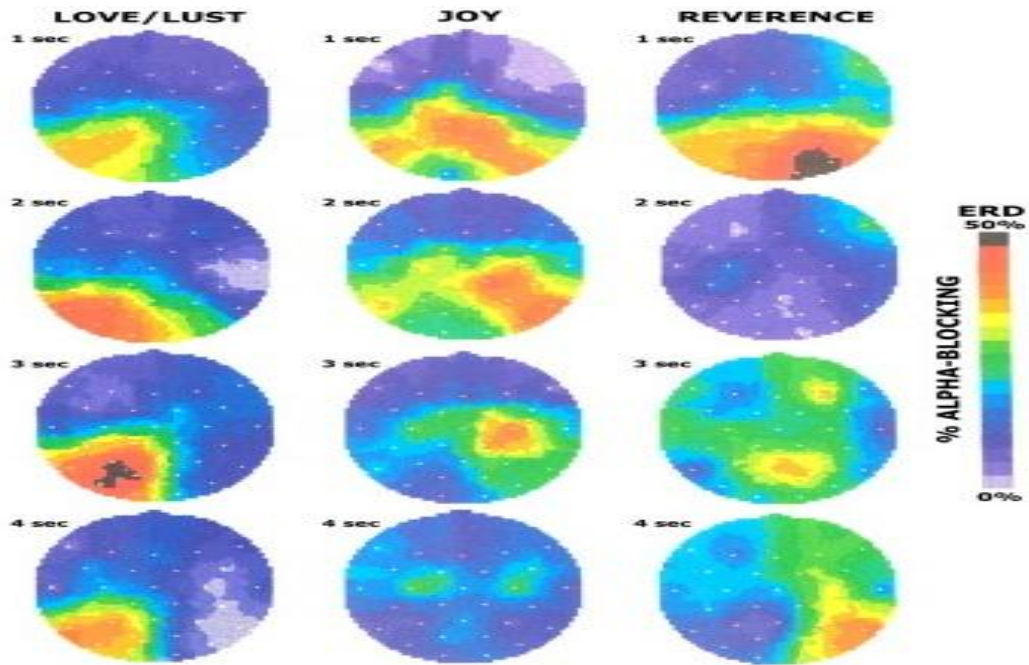


Fig .9.Brain Activity for Love, Joy and Reverence

The above Fig. 6 and Fig.7 shows the region of relation between arousal with valence. The relation between physiological signals and arousal/valence is established due to the activation of the automatic nervous system when emotions are elicited. After perceiving a stimulating event, an individual instantly and automatically experiences physiological changes, these response to this changes are called Emotion. Fig.8 and Fig.9 shows the various emotion states and its brain activity.

3.8 Recording of Emotional States Changes through EEG: EEG was used to study the individual's emotional state for more than two decades. The useful information about the emotional state may be obtained as long as stable EEG patterns on the scalp are produced. EEG recordings capture neural activity on a millisecond scale from the entire cortical surface [19].

According to (Lee M, 2000) this study, the positive and negative emotions may or may not be estimated from the EEG signal using Skinner's Point -Wise Correlation Dimension (PD2) analysis. But this PD2 represents some of the mental activity in the brain areas. The Fig.10 simply shows the region of brain activated in emotion recognition. Where the Green color indicates the neutral, red color indicates the anger emotion and purple color indicates the happiness. At last the blue color indicates the sadness of the human.



Fig.10. Localization of Brain Region for Emotion Recognition

The electrical activity of the human brain is recorded through the electrodes, which are placed on the scalp of the brain. These recorded brain waves are undergone for pre-processing [20].

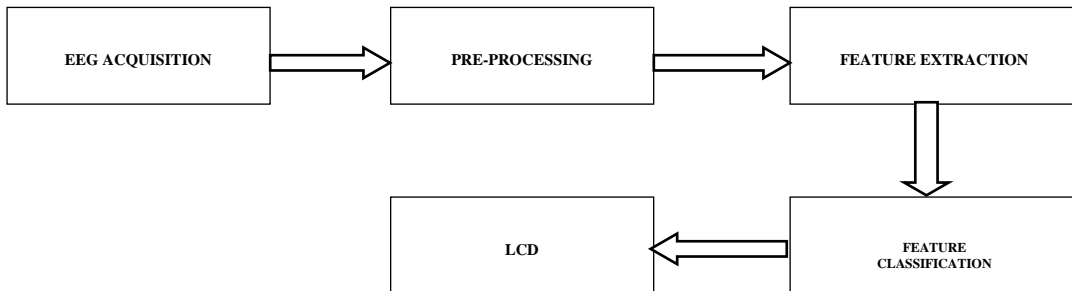


Fig.11. Basic Diagram for Human Emotion Recognition using EEG signals

Dimension reduction can be done by several methods such as, Principal Component Analysis (PCA), Independent Component Analysis (ICA).[21] These extracted features are classified for seven different kinds of emotions say, Happy, Anger, Joy, Disgust, Fear, Relax, and Neutral through artificial intelligence techniques such as Neural Network, Genetic Algorithm, Support Vector Machine, Fuzzy Logic, and Hybrid Structure of the above method [22].

3.9 Speech Synthesis: This module of the system is consisted of a microcontroller (ATMEGA), a SPO256 (speech synthesizer) IC, amplifier circuitry and a speaker.

The function of this module is to produce voice against the respective gesture. The microcontroller receives the eight bit data from the "bend detection" module. It compares the eight bit data with the predefined values. On the basis of this comparison the microcontroller comes to know that which gesture does the hand make.

Now the microcontroller knows that which data is send by the bend detection module, and what the meaning of this data is. Meaning means that the microcontroller knows, if the hand is making some defined gesture and what should the system speak.

The last step of the system is to give voice to the each defined gesture. For this purpose a speech synthesizer IC, SPO256 is used. Each word is consisted of some particular allophones and in case of Speech synthesizer IC each allophones have some particular addresses. This address is to be sent to the SPO256 at its address lines, to make the speaker, speak that particular word.

The summary of the story is that we must know the address of each word or sentence, which is to be spoken by this module. Now these addresses are already stored in the microcontroller. So far, the microcontroller knows what is the gesture made by the hand, and what should be spoken against it. The microcontroller sends the eight-bit address to SPO256. This eight-bit address is representing the allophones of the word to be spoken.

SPO256 gives a signal output. This signal is amplified by using the amplifying circuitry. The output of the amplifier is given to the speaker.

3.10 LCD Display: By using the gesture vocalizer the dumb people can communicate with the normal people and with the blind people as well, but the question arises that how can the dumb people communicate with the deaf people. The solution to this problem is to translate the gestures, which are made by the hand, into some text form. The text is display on LCD. The gestures are already being detected by the "Gesture Detection" module.

This module sends signal to the speech synthesis module, the same signal is sent to the LCD display module. The LCD display module is consisted of a microcontroller and an LCD. The microcontroller is controlling the LCD. A signal against each gesture is received by LCD display module. The LCD display module checks each signal, and compares it with the already stored values. On the basis of this comparison the microcontroller takes the decision what should be displayed, having taken the decision the microcontroller send an eight bit address to the LCD, this eight bit address, tells the LCD, what should be displayed.

The EEG signal output is given to the LCD to display the emotion of the person in order to know his state of speech. Using the information's from EEG signal (emotion) the person can communicate with each other more smoothly.

The block diagram of the LCD display module is shown in the Fig.12.

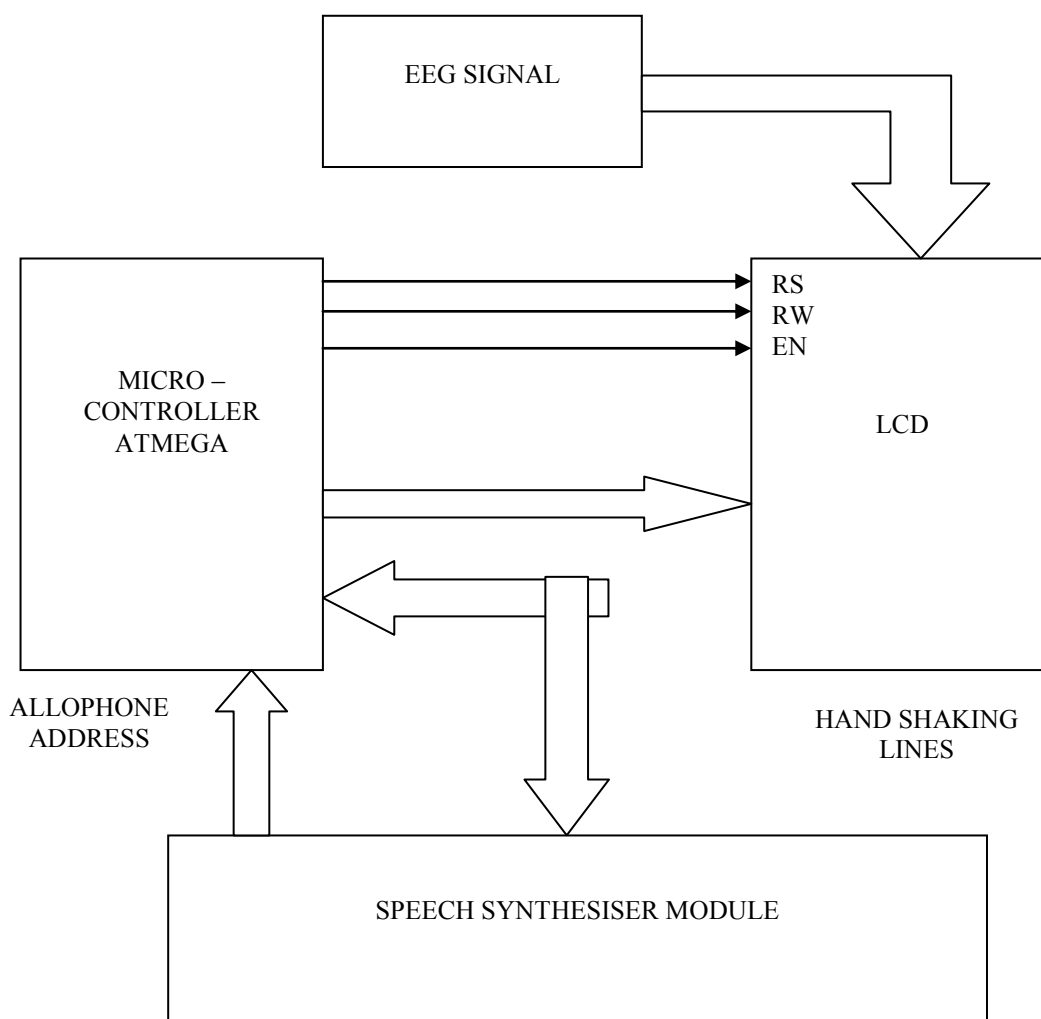


Fig. 12. Block Diagram LCD Display Module

4. Result and Discussion

Thus the effective communication device for the differently-abled persons is designed and their emotions are determined with the help of EEG using which they are able to communicate like ordinary people. The flex and accelerometer sensors determines the Gesture (sign language), it is then converted into speech and text using Microcontroller and PC Interface. The electrodes are used

for analysing the EEG signals for detecting the emotion of the people during his conversation. By combining these new –SMART DEVICE” is developed for Gifted Aspirants.

5. Overall Kit Design

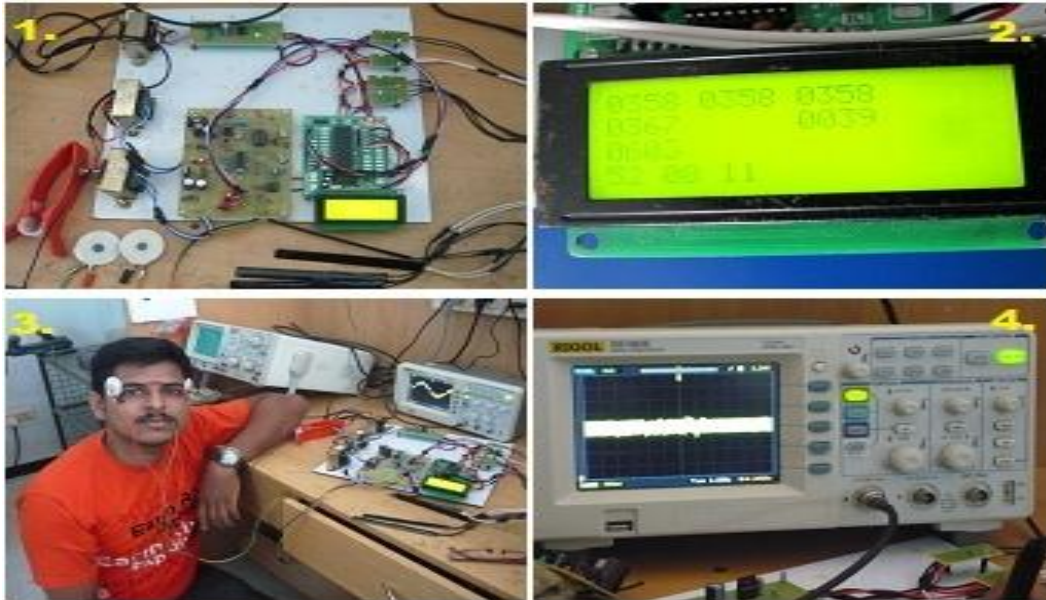


Fig.13.SnapShot of Designed Module

- Embedded Kit along with Sensors and Electrodes.
- LCD Module.
- Analysis of EEG Signal.
- EEG Output.

6. Conclusion and Future Enhancements

This research paper describes the design and working of a system which is useful for dumb and deaf to communicate with one another and with the normal people. The dumb people use their standard sign language which is not easily understandable by common people and blind people cannot see their gestures. This system converts the sign language into voice which is easily understandable by blind and normal people. The sign language is translated into some text form, to facilitate the deaf people as well. This text is display on LCD.

There can be a lot of future enhancements associated to this research work, which includes:

- 1- Designing of wireless transceiver system for –Differently –Abled persons using sensors”

- 2- Perfection in monitoring and sensing of the dynamic movements involved in –Sensors and Gesture Vocalizer”.
- 3- Designing of a whole jacket, which would be capable of vocalizing the gestures and movements of Human.
- 4- Virtual reality application e.g., replacing the conventional input devices like joy sticks in videogames with the data glove.
- 5- The Robot control system to regulate machine activity at remote sensitive sites.

References

- Kazunori Umeda Isao Furusawa and Shinya Tanaka, —Recognition of Hand Gestures Using Range Images”, Proceedings of the 1998 IEEW/RSJ International Conference on intelligent Robots and Systems Victoria, B.C., Canada October 1998, pp.1727-1732
- SrinivasGutta, Jeffrey Huang, Ibrahim F.Imam, and Harry Wechsler, –Face and Hand Gesture Recognition Using Hybrid Classifiers”, ISBN: 0- 8186-7713-9/96, pp.164-169
- Jean-Christophe Lementec and Peter Bajcsy, —Recognition of Am Gestures Using Multiple Orientation Sensors: Gesture Classification”, 2004 IEEE Intelligent Transportation Systems Conference Washington, D.C., USA, October 34, 2004, pp.965- 970
- SushmitaMitra and TinkuAcharya,”Gesture Recognition: A Survey”, IEEE TRANSACTIONS ON SYSTEMS, MAN, AND CYBERNETICS—PART C:APPLICATIONS AND REVIEWS, VOL. 37, NO. 3, MAY 2007, pp. 311-324
- Recognition: A Survey”, IEEE TRANSACTIONS ON SYSTEMS, MAN, AND CYBERNETICS—PART C:APPLICATIONS AND REVIEWS, VOL. 37, NO. 3, MAY 2007, pp. 311-324
- Seong-Whan Lee, —Automatic Gesture Recognition for Intelligent Human-Robot Interaction” Proceedings of the 7th International Conference on Automatic Face and Gesture Recognition (FGR’06) ISBN # 0-7695- 2503-2/06
- Md. Al-Amin Bhuiyan, –On Gesture Recognition for Human-Robot Symbiosis”, The 15th IEEE International Symposium on Robot and Human Interactive Communication (RO-MAN06), Hatfield, UK, September 6-8, 2006, pp.541-545
- Toshiyuki Kirishima, Kosuke Sato and KunihiroChihara, –Real-Time Gesture Recognition by Learning and Selective Control of Visual Interest Points”, IEEE TRANSACTIONS ON PATTERN ANALYSIS AND MACHINE INTELLIGENCE, VOL. 27, NO. 3,MARCH 2005, pp. 351-364
- Attila Licsár and TamásSzirány, –Dynamic Training of Hand Gesture Recognition System”, Proceedings of the 17th International Conference on Pattern Recognition (ICPR’04), ISBN # 1051-4651/04,

- D. W. Patterson, "Introduction to Artificial Intelligence and Expert Systems", Prentice-Hall Inc., Englewood Cliffs, N.J, USA, 1990.
- J R. Poppe, "Vision-based human motion analysis: An overview", *Computer Vision and Image Understanding*, vol. 108, 2007, pp. 4-18
- Dr.R.Newport, Human Social Interaction perspectives from neuroscience, www.psychology.nottingham.ac.uk/staff/rwn.
- Marcel S, Jose del and R.Millan, 2006. "Person Authentication Using Brainwaves (EEG) and Maximum A Posteriori Model Adaptation", *IEEE Trans on Pattern Analysis and Machine Intelligence*, Special issue on Biometrics, pp, 1-7.
- Jenkins J.M, Oatley K, and Stein NL, 1998. "Human Emotions", A reader Balck Well Publisher.
- Cacioppo C.J, Tassinary LG, 1990. "Inferring Physiological Significance from Physiological Signals", *American Psychologist*.
- Ekman P, Levenson R.W, and Freison W.V, 1983. "Autonomic Nervous System Activity Distinguishes Among Emotions", *Journal of Experimental Social Psychology*, pp, 195-216.
- Winton WM, Putnam L, and Krauss R, 1984. "Facial and Autonomic Manifestations of the dimensional structure of Emotion", *Journal of Experimental Social Psychology*, pp, 195-216.
- Savran A, ciftci K, Chanel G, Javier Cruz Mota, Luong Hong Vie , Sankur B, Akarun L, Caplier A, and Rombaut M, 2006. "Emotion Detection in the Loop from Brain Signals and Facial Images" *eNTERFACE'06*.
- Picard R.W, 2000. "Affective Computing", MIT Press.
- Picard R.W, Vyzas E, and Healey J, 2001. "Towards Machine Emotional Intelligence: Analysis of Affective Physiological State", *IEEE Transactions on Pattern Analysis and Machine Intelligence*, 23(10), pp, 1175- 1191.
- Ali S. AlMejrad "Human Emotions Detection using Brain Wave Signals: A Challenging" - *European Journal of Scientific Research* ISSN 1450-216X Vol.44 No.4 (2010), pp.640-659
- Niemic C.P, 2002. "The theoretical and empirical review of psycho physiological studies of emotion", 1(1), *Journal on Clinical and Social Psychology*, pp, 15-18.

Efficient Removal of Artifacts from EEG SIGNAL Using Enhanced Hybrid Learning Method

B. Paulchamy

*Department of Electronics and Communication Engineering,
Hindusthan Institute of Technology, Coimbatore, Tamil Nadu, India*

KEYWORDS IANFIS. Monitoring System. Motion Artifacts. Signal Processing. PSO

ABSTRACT In this paper, the analysis and removal of artifacts is done by the proposed technique. Normally, ECG is one of the components of artifacts source and EEG is mixed by various artifacts and affects the electroencephalographic data. For further clinical analysis the data preparation is important to minimize the artifacts. In proposed method, Improved Adaptive Neuro-Fuzzy Inference System (IANFIS) and Improved ANFIS-Particle Swarm Optimization (IANFIS-PSO) algorithms are used to separate the signals of ECG and EEG for eliminating artifacts and to intensify the estimation of EEG signal quality. The pre-processing is done by ennobled quantum based genetic algorithm for fast process of optimization and removal of noise interference. The simulation result shows the improvement in Signal-to-Noise Ratio (SNR), minimum Mean-Square Error (MSE) along with the Power Spectrum Density (PSD) plot, which are used to measure the performance comparison of proposed with existing algorithm. The prospective method performs with more appropriate process of enhanced hybrid learning method and outperforms in minimizing the artifacts of ECG from the corrupted signals of EEG.

INTRODUCTION

In developing the environment, the advanced technology plays an important role in all fields. In medical line, recording of human body electric potentials and detecting the implantable system is done by using the advanced technology. Electrocardiogram or Electromyogram recording is used to monitor the activities of brain by detecting the location (Ravi and Suma 2016). The signal bandwidth is varied for both ECG and EMG from tens to hertz or kilo-hertz while the site of recording is small with amplitude voltage less or in mill-volts. The extracted signal magnitude is based on various factors like signal level activity, electrode type, contact impedance and electrode placement. These would vary as per time according to the patients. Generally high gain is required to ensure the signal-to-noise ratio throughout the cascade of signal processing management (Pavithra 2016). The automatic adjustment of gain in amplifier is necessary for condition matching during recording time. The conventional method is used to perform the variation process of gain.

In signal processing, the detection of disorder and status of sleep is obtained by the standard technique of Polysomnography (PSG) analysis (Princy 2015). In order to procure the knowledge of various functions of corporal, the perfor-

mances of the biological signals are analyzed. By including the signals like electromyogram, electroencephalogram, abdominal and thoracic breathings, oronasal airflow, electrocardiogram, oxygen saturation, electro-oculogram, blood pressure and other biomedical records are used to analyze the signals to detect the status of health (Umera Banu et al. 2016). To observe the activity of brain, Electroencephalography (EEG) tool is used. By this tool the performance of detecting the localization and resolution of time are considered apparent, easy accessible, prostrate and prominent in performances. In clinical work this signal is used widely and have small signal-to-noise ratio. The normal signal waveform of EEG is shown in Figure 1.

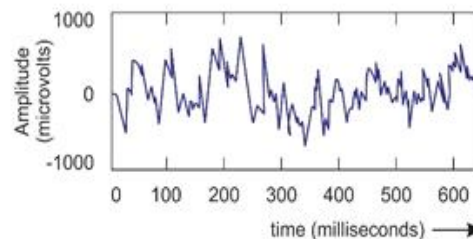


Fig. 1. EEG signal waveform
Source: Author

Usually EEG signal is used to detect the rhythms neural which are affected by the source of noise and biological signals. According to the process of EEG signal the sources are analyzed and the clinical information is obtained. The analysis will become difficult when the source of noise increases. In frequency and time domain the techniques are developed in order to remove artifacts. By filtering, the common noises are removed which are present in the recorded signal (Serteyn et al. 2015). Figure 2 shows the flow work of removing noise from the signal.

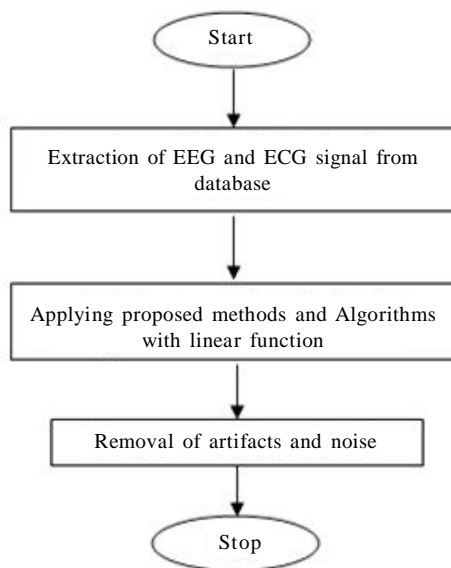


Fig. 2. Noise removal flow work
Source: Author

In this paper, the removal of artifacts is done by using the proposed method and algorithm. By the proposed method the EEG and ECG signals are separated. The functions are trained and initialized to extract the signals by using IANFIS-PSO algorithm. The rest of the paper is organized section wise. In section II the literature review of ECG and EEG extraction is discussed. In section III the explanation of proposed method and algorithm is presented. The simulation result of the proposed technique is illustrated in section IV. Finally the conclusion and future work are presented in section V.

MATERIAL AND METHODS

The removal of artifacts and the analysis of signals are discussed in this section. Electroen-

cephalogram (EEG) is an electrical activity recording and improved to proceed with the cerebral signal recording. The unwanted signals, generated when recording activities are called artifacts. The analysis of signal is affected by artifacts and in order to reduce artifacts, hybrid learning algorithm is implemented based on Adaptive Neuro-Fuzzy Inference System (ANFIS). By Particle Swarm Optimization (PSO) algorithm the process of extracting is performed with the analysis of signal (Priyadharshini and Edward 2014). During the recording of EEG the sources of noise is reduced by those techniques (Reddy and Narava 2013). The structure of ANFIS is shown in Figure 3.

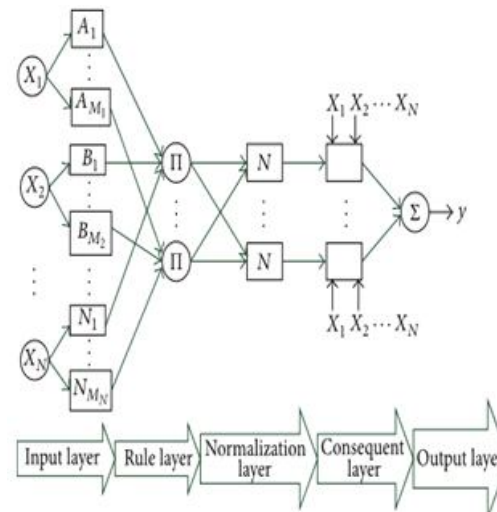


Fig. 3. ANFIS structure
Source: Author

The changes of activities with various parameters are recorded, based on signal EEG inside and outside the environment. Event related potential is used to generate the informative signals from the device and it is made more informative by using mathematical tool. Every change is based on the data of ERP. In order to generate signal processing the biomedical engineering ERP and EEG is used for analysis and pre-process by using soft computing tools (Tandle and Jog 2015).

Based on adaptive filter of cascade, the EEG signal artifact is removed by the Least Mean Square (LMS) algorithm. The filter function is used to cancel EOG spikes, line interference elimination and ECG artifacts removal. For reduction Finite Impulse Response (FIR) filter is present-

ed in EEG signals (Roy and Shukla 2015). The reduction of noise factors is based on Adaptive Linear Neural Networks (ADALINE) and wavelet transformation in EEG signals (Zhang et al. 2015).

The efficiency of the ECG monitoring is significantly damaged by artifacts movement, which causes unsuitable treatment or false alarm triggers and misdiagnoses. However, noise separation from bio-signal is challenging because of overlapping frequency spectrum. As per the removal technique of artifacts, motion using accelerometer helps to monitor ECG and tele-homecare (Reyes et al. 2014; Al-Qazzaz et al. 2015).

To reduce interference common mode, the microcontroller operates the automatic gain control circuit (AGC) and setup of recording Double-Differential (DD) to provide tunable gain. The imbalance network is reduced by generating the signal clock by using custom-designed variable gain amplifiers (ASIC) based on microcontroller (Rieger and Deng 2013).

The physiological parameters of the ECG signals are tested and optimized based on Block-Based Neural Network (BBNN) algorithm. The structure of model, parameters and weight are performed by optimizing with wavelet mutation, searches through information element over a space search (San et al. 2013). The data of ECG is accomplished in an unrestricted manner by developing the technique by detecting and analysis of obstructive apnea with quality (Lee et al. 2013).

The application of portable ECG monitoring, the mixed-signal ECG System-on-Chip (SoC) is operative with low-power consumption for high quality signal. By custom digital signal processor the detection of peak and removal of artifacts motion is performed (Kim et al. 2014). Figure 4 shows the mixed signal of ECG and EEG with interference of line in recording.

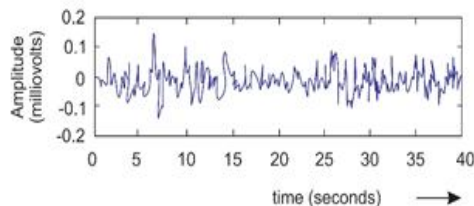


Fig. 4. EEG signal recording with ECG signal and interference
Source: Author

Proposed Work

In this section, the proposed algorithm technique of removing artifacts is explained with application. By the proposed method the input source is trained and initialized to extract the signal from the MIT-BIH database. By the analysis and implementation of proposed enhanced hybrid learning method, the ECG and EEG signals are separated with artifacts minimization.

EEG signal is affected by the artifacts of ECG. In order to avoid the artifacts the signals are separated for better quality of signal to analyze the EEG signal. It records the electrical activity of the brain. When recording the signal the cerebral origin is also included, this is mentioned as ECG artifacts. In the designed method Improved Adaptive Neuro-Fuzzy Inference System (IANFIS) and Improved ANFIS-Particle Swarm Optimization (IANFIS-PSO) algorithm, are used to remove artifacts from the signal and the flow of proposed system implementation is shown in Figure 5.

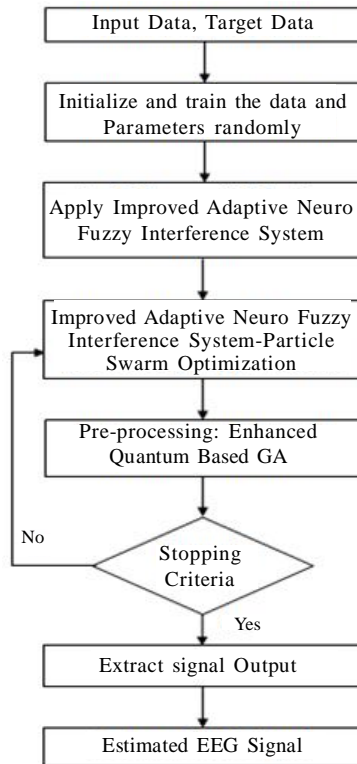


Fig. 5. Proposed system Flow work
Source: Author

The optimized parameter is applied to the structure of IANFIS for separating the signals with removal of artifacts. By optimization algorithm the membership function is initialized and the input and the parameters are trained randomly using Improved ANFIS-Particle Swarm Optimization (IANFIS-PSO). The membership function of the proposed algorithm is given below:

$$\mu_X(a_1) = \frac{1}{1 + \left| \frac{a_1 - z_i}{x_i} \right|^{2y}} \quad (1)$$

The parametric representation of IANFIS, back propagation function and updating functions of parameter is given below:

$$S1 = \{ \{x_{11}, y_{11}, z_{11}\}, \{x_{12}, y_{12}, z_{12}\}, \dots, \{x_{1p}, y_{1p}, z_{1p}\}, \dots, \{x_{np}, y_{np}, z_{np}\} \} \quad (2)$$

Back propagation:

$$E = \sum_{k=1}^K E_k \quad (3)$$

Parameter Updating

$$\Delta \alpha_n = -\eta \frac{\partial E}{\partial \alpha_n} \quad (4)$$

Pre-processing of the system is used to filter the noise from the signal extraction. It is processed in the system until it satisfies the stopping criteria of finding minimum particles of error, using the step based enhanced quantum based genetic algorithm. It provides fast process and removal of noise interferences (Singh and Sharma 2015). The flow work or the procedure of pre-processing is implemented as shown in Figure 6 and learning process procedure is given below.

Procedure of learning the process and GA is performed for finding the fitness function and sorting the chromosomes in ascending order. Then the maximum generation is obtained to find probabilities of mutation and crossover.

Procedure Begin

Initialize $t = 0$ and $P(t)$;

While ($t < \text{maximum generation}$) do

Increment $t = t + 1$;

Evaluate sorting-fitness ($P(t-1)$);

Find $P(t)$ and $P(t-1)$;

Complete $P(t)$ by mutation and crossover;

End while

End

To maximize the iteration of the process, stopping criteria is used and by fitness function the Mean Square Error is considered (Ashfanoor and Cellia 2012). At the end of iteration the best

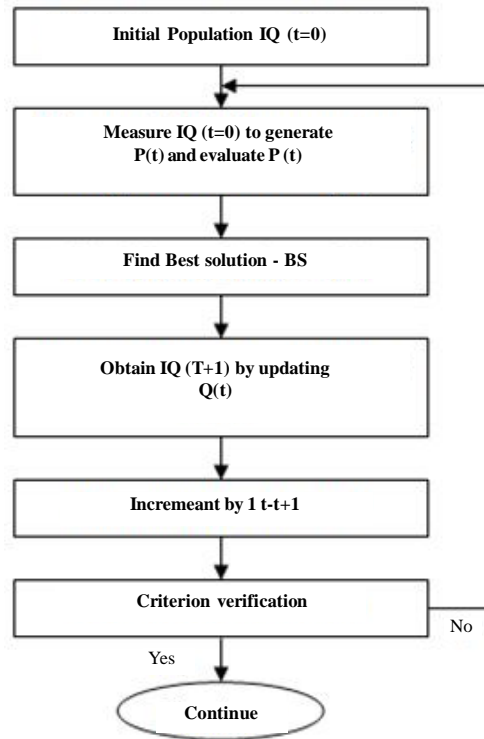


Fig. 6. Flow work of Enhanced quantum based GA
Source: Author

solution is obtained by finding the Minimum Mean Square Error particle and the solution is submitted to ANFIS structure. To extract signal using the optimized parameters is implemented by using proposed algorithm and obtain EEG signals with minimized artifacts and estimation.

RESULTS AND DISCUSSION

In this section, the simulation results of the proposed system is evaluated and analyzed to show better performance than the existing system. The proposed algorithm is executed to simulate the real data set from the MIT-BIH database to extract the EEG signal. Figure 7 shows the input sources of mixed standard signal of EEG and ECG.

From the source signal the separation of signals are EEG and ECG is performed by using proposed method. EEG signal is to be found along with noise. So, by using proposed algorithm IANFIS-PSO the EEG signal is extracted by reducing noise. Figure 8 shows the extrac-

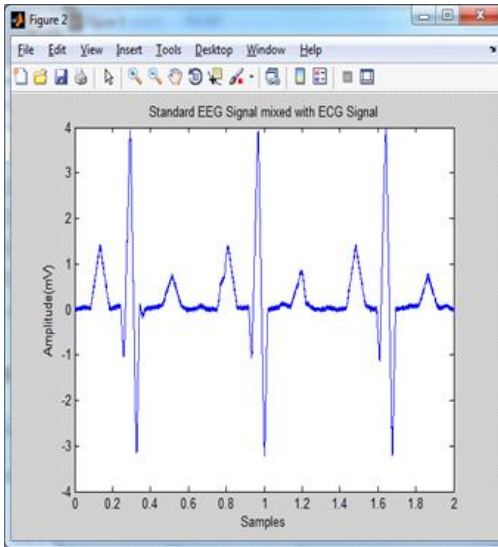


Fig. 7. Standard EEG signal mixed with ECG signal
 Source: Author

tion of EEG signal from the input source signal. It clearly shows the proposed technique removes only the noise from the EEG signal without affecting the information content. And Figure 9 shows the extraction of non-linear ECG signal from the source input (Khatwani and Tiwari 2013). The source input is original EEG signal with Noise (ECG) Signal. From the original input through the proposed technique the non-

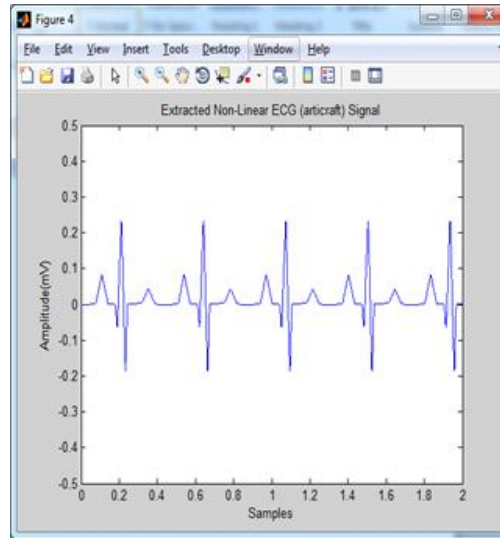


Fig. 9. Extracted Non-linear ECG (artifacts) signal
 Source: Author

linear ECG Artifacts signal only removed. The power spectral density of the proposed system is shown in Figure 10. This power spectral plot shows the each trial of noisy EEG signal and artifacts Signal by the proposed method.

Table 1 performance analysis of proposed system with existing system, it summarizes the comparison of performance analysis of proposed and existing algorithms with the results of pa-

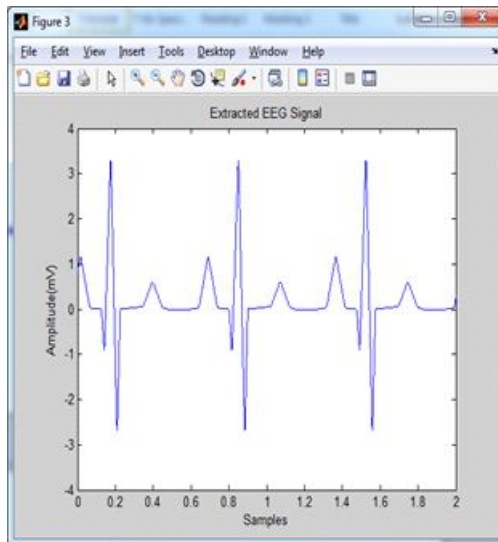


Fig. 8. Extracted EEG signal
 Source: Author

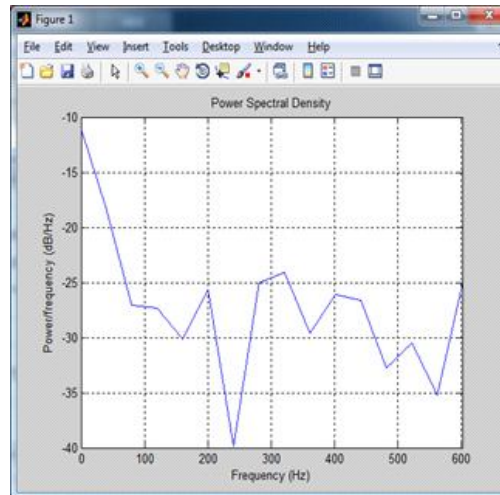


Fig. 10. Analysis of proposed system power spectral density
 Source: Author

Table 1: Performance analysis of proposed system with existing system

Methods	PSNR (dB)	SNR (dB)	MSE	Entropy	Execution time
Existing method	27.45	15.0245	5.1424e-004	3.0859	6.543258
ANFIS	29.57	10.0423	0.0015	5.3323	4.157356
IANFIS-PSO	31.63	9.4858	0.0011	8.3348	3.033725

rameters PSNR, SNR, MSE, entropy and execution time. Concluded that in ANFIS method PSNR value is higher than existing method. IANFIS-PSO method PSNR value is higher than in ANFIS method. Finally IANFIS-PSO method achieves high PSNR value compared to existing and ANFIS method. Similarly IANFIS-PSO method outperformed existing and ANFIS method as far as SNR, MSE, entropy and execution time Figure 11 shows the performance evaluation of the proposed system X-axis epochs, Y-axis Root Mean Square Error and Figure 12 shows the PSNR and SNR performance of proposed system with existing system (Sabarimalai and Suman 2012; Kaur and Malhotra 2014). This comparative analysis clearly shows that the proposed technique gives better PSNR and SNR values compared to existing method. And Figure 13 shows the analysis of Entropy and processing time of proposed method with existing method. It clearly shows that, IANFIS-PSO method outperformed when

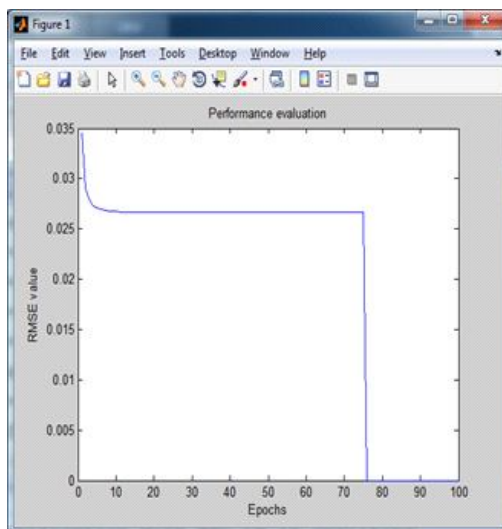


Fig. 11. Analysis of proposed system performances evaluation
Source: Author

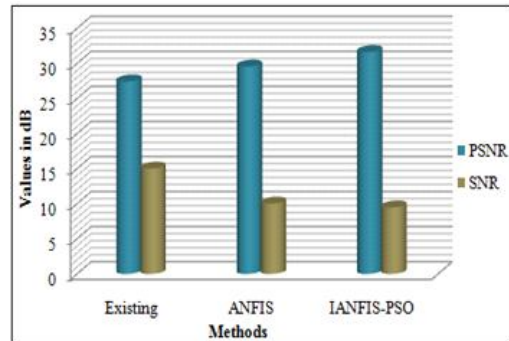


Fig. 12. Performance analysis of PSNR and SNR values

Source: Author

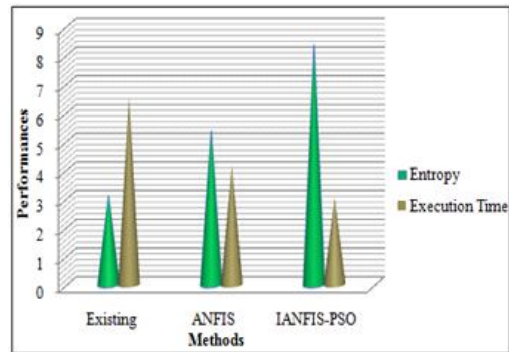


Fig. 13. Performance analysis of entropy and execution time

Source: Author

compared to existing and ANFIS method as far as entropy and execution time are concerned.

CONCLUSION

In this paper, the IANFIS is applied to the model to train and initialize the data from the MIT-BIH database to extract the signal for better performance for reducing the artifacts in the signal. The efficient process of identifying the parameters is based on the enhanced hybrid learning algorithm. The experimental and simulation results of our system shows better perfor-

mance than existing, without performance degradation for same data; also reduced noise or artifacts in the signal. The RMSE result is based on member function inputs. From the experiment results finally the researcher concludes that the proposed method provides improvement in power spectral density of de-noised signal high signal to noise ratio value, reduction in the time in removal process, Entropy achievement and improvement of information content in the signal.

RECOMMENDATIONS

Future work is to further improve the performance of reducing the artifacts in EEG signal. Consider more data sets with some more parameters to provide analysis with high quality of solution and performances. Multidirectional transforms like curvelet and contourlet transform can be investigated to denoise the EEG signal.

REFERENCES

- Acharya Rajendra, Molinari U, Filippo, Sree Vinitha, Chattopadhyay, S, Subhagata Ng Kwan Hoong, Suri Jasjit S 2012. Automated diagnosis of epileptic EEG using entropies. *Most cited Biomedical Signal; Processing and Control Article*, 7(7): 401-408.
- Al-Qazzaz NK, Mohd Ali SHB, Ahmad SA, Islam MS, Escudero J 2015. Selection of mother wavelet functions for multi-channel EEG signal analysis during a working memory task. *Int Journal Sensors*, 15: 29015-29035.
- Ashfanoor Kabir Md, Cellia Shahnaz 2012. Denoising of EEG signal based on noise algorithm in EMD and wavelet domains. *Most cited Biomedical Signal; Processing and Control Article*, 7(5): 481-489.
- Banu Umera, Patil GM, Fatima Ruksar 2016. A Survey on sources of noise and advanced noise removal Techniques of Biosignals. *International Journal on Emerging Technologies (Special Issue on ICRIET-2016)*, 4(4): 8-1.
- Kaur Simranpreet, Malhotra Sheenam 2014. Various techniques for denoising EEG signal: A review. *International Journal of Engineering and Computer Science*, 3(8): 7966-7973.
- Khatwani Priyanka, Tiwari Archana 2013. A survey on different noise removal techniques of EEG signals. *International Journal of Advanced Research in Computer and Communication Engineering*, 2(2): 1091-1095.
- Kim H, Kim S, Helleputte NV, Artes A, Konijnenburg M, Huisken J, Hoof CV, Yazicioglu RF 2014. A configurable and low-power mixed signal SoC for portable ECG monitoring applications. *IEEE Transactions on Biomedical Circuits and Systems*, 8(2): 257-267.
- Lee HJ, Hwang SH, Lee SM, Lim YG, Park KS 2013. Estimation of body postures on bed using unconstrained ECG measurements. *IEEE Journal of Biomedical and Health Informatics*, 17(6): 985-993.
- Princy R, Thamarai P, Karthik B 2015. Denoising EEG signal using wavelet transform. *International Journal of Advanced Research in Computer Engineering & Technology (IJARCET)*, 4(3): 1070-1074.
- Pavithra A 2016. Removing of artifacts from biomedical Signals by using DWT and ANC Algorithm in real time sensor applications. *International Journal of Innovative Research in Advanced Engineering*, 3(4): 46-49.
- Ravi M, Suma KV, 2016. Hardware Simulation for Bio-Signal Acquisition System. *International Journal of Engineering Research in Electronic and Communication Engineering*, 3(6): 121-126.
- Reddy AG, Narava S 2013. Artifact removal from EEG signals. *International Journal of Computer Applications* 77(13): 17-19.
- Reyes BA, Posada-Quintero HF, Bales JR, Clement AL, Pins GD, Swiston A, Riistama J, Florian JP, Shykoff B, Qin M, Chon KH 2014. Novel electrodes for underwater ECG monitoring. *IEEE Transactions on Biomedical Engineering*, 61(6): 1863-1876.
- Rieger R, Deng SL 2013. Double-differential recording and AGC using micro controlled variable gain ASIC. *IEEE Transactions on Neural Systems and Rehabilitation Engineering*, 21(1): 47-54.
- Roy V, Shukla S 2015. A survey on artifacts detection techniques for Electro Encephalography (EEG) signals. *International Journal of Multimedia and Ubiquitous Engineering*, 10(3): 425-442.
- Sabarimalai Manikandan, Soman KP 2012. A novel method for detecting R-peaks in electrocardiogram (ECG) signal. *Most cited Biomedical Signal; Processing and control Article*, 7(2): 118-128.
- San PP, Ling SH, Nguyen HT 2013. Industrial application of evolvable block-based Neural Network to Hypoglycemia Monitoring System. *IEEE Transactions on Industrial Electronics*, 60(12): 5892-5901.
- Serteyn A, Vullings R, Meftah M, Bergmans JW 2015. Motion artifacts in capacitive ECG measurements: Reducing the combined effect of DC voltages and capacitance changes using an injection signal. *IEEE Transactions on Biomedical Engineering*, 62(1): 264-273. Singh, Vivek, Sharma, Reecha 2015. Wavelet based method for denoising of electroencephalogram. *International Journal of advanced Research in Computer Science and software Engineering*, 5(4): 1113-1117.
- Suja Priyadarshini S, Edward Rajan S 2014. An efficient method for removal of ECG artifacts from measured EEG signal using PSO algorithm. *International Journal Soft Computing Applications*, 6(1): 1-19.
- Tandle A, Jog N 2015. Classification of Artefacts in EEG Signal Recordings and Overview of Removing Techniques. *International Conference on Computer Technology (ICCT)*, Coimbatore, India, September 15, pp. 46-50.
- Zhang C, Tong L, Zeng Y, Jiang J, Bu H, Yan B, Li J 2015. Automatic artifact removal from electroencephalogram data based on a priori artifact information. *BioMed Research International*, 2015: 1-8.



Simulation and performance analysis of 15 Nm FinFET based carry skip adder

N. Duraivel¹ | B. Paulchamy²

¹Department of Electronics and Communication, Kings Engineering College, Chennai, India

²Department of Electronics and Communication, Hindusthan Institute of Technology, Coimbatore, India

Correspondence

N. Duraivel, Department of Electronics and Communication, Kings Engineering College, Chennai, Tamil Nadu, India.
Email: duraivelkings@gmail.com

Abstract

Various changes in the advanced semiconductor industry, designing adder with higher performance is a major concern. These proposed works constrain the major area in FinFET designing at the range of 15-nm FinFET technology at 25°C. By designing the FinFET technology with the range of 15 nm is the rising transistor technology with the lesser delay and the management in the power tradeoff. FinFET technology makes the evolutionary step in the semiconductor field because various adders have various complications in scaling at the range of 15 nm. The speed reinforcement is used based on various schemes to improve the efficiency of the conventional carry skip adder (Conv-CSKA) structure. By taking into account multiplexer logic, the proposed designing structure made in the account of AND-OR-Invert (AOI) and OR-AND-Invert (OAI) compound gates which are used as the skip logic. The simulation is carried out using HSPICE and Tanner. In various research works, it is concluded that the FinFET based adders are implemented in the semiconductor devices which are the advanced part of the computerized technique with the advancement in the designing circuits. The proposed designing structure includes the 8 T adders which reduce the power consumption with different datapath. The modified designing increases the slack time and decreases the input voltage. This article implements the comparison of FinFET designing based



on their speed, power, and energy with the other adder circuits using 15-nm FinFET technology.

KEYWORDS

AND-OR-Invert (AOI) and OR-AND-Invert (OAI), conventional carry skip adder (conv-CSKA), FinFET technology

1 | INTRODUCTION

The semiconductor circuit designing process has subjected to various difficulties and challenges, which happen due to the rapid growth in the trending world and the innovation in the equipment for past years. In addition to that, more functional changes happen due to the demands in the applications in the revolutionary changes of chip designing. By increasing the requirements in the single-chip designing based on the demands and the development of the various complex tools, can perform the complicated operations. This complicated operation may lead to an increase in power and energy. The speed of the processor depends upon the adders and multipliers which is the major concern of the designing scenario. Based on the power and energy, many efforts were carried out by many researchers which are illustrated in References 1,2 This higher speed may increase with the lower energy and the lower power consumptions, which is the major difficult task faced by the designers of general-purpose processors.

The best technique to reduce the power consumption in the digital circuits is by decreasing the supply voltage which happens due to the switching of energy because of voltage. By the consideration of the sub-threshold current between the devices, the leakage current is low in the OFF circuits which have an exponential increment due to the supply voltage through the technique that is drained-induced barrier lowering effect.³

The major technique for the supply voltage reduction is by the several operations carried out during the ON devices in a transistor, which may lead to the formation of three regions, namely, super threshold, near-threshold, and sub-threshold regions. By the changes in the super threshold region, the low delay and higher switching with the lesser leakage powers are achieved. In the sub-threshold region, the delay between the gates and the leakage power is achieved with the lower value using the supply and threshold voltages.

Most of the recent analysis states that the nearest threshold region has been included as the major region of analyzing the trade point between the low delay and the power dissipation as compared to the sub-threshold region. By the sub-threshold region, the delay in the designed circuit will be less due to factors such as switching and leakage powers.

By considering the threshold operation, the input voltage that is approximately nearer toward the threshold voltage of the transistor circuit⁴ has the lesser delay and leakage power as a comparison with the sub-threshold region.

The performance of the circuit device depends upon the supply voltage, which is featured based on the input dynamic voltage and the frequency scaling. By the reduction in energy consumption, the input system changes the input voltage level which is based on the workload surroundings.⁵ By the changes in the system, the designed circuit will work under the various supply voltage circumstances.

To increase the speed within the circuit, the supply voltage is reduced in the computational blocks. In the major part of the designing, an adder is a major component that affects the speed

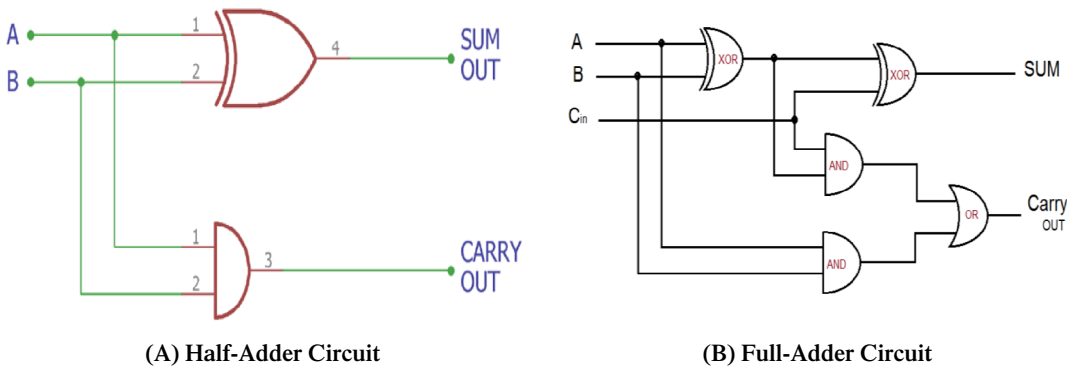


FIGURE 1 A, Half-adder circuit. B, Full-adder circuit [Color figure can be viewed at wileyonlinelibrary.com]

factor and the efficiency within the processors.^{6,7} By the changes in the supply voltage, different adder structures represent the changes in the optimization in power and speed.

1.1 | Design of adders using FINFET technology

Adder represents the basic component in any hardware implementation of the semiconductor devices. By the changes in the adder circuit, the performance of the processor may change. Hence, the changes in the performance of the processor depend upon the adder circuit, which is analyzed in various surveys.⁸

Various surveys were taken externally or internally in the semiconductor devices for the increment in the performance of the processors.⁹ The testing that is taking place externally deals with the input data, whereas the internal testing deals with the logical analysis, circuitual design, and the structure of the adder, and multiplier that is designed.¹⁰

Figure 1A,B represents the design of different kinds of adders, which decides the inner circuit-level performances. The battery's performance is decided by the low power and efficiency in many industrial applications.^{11,12} By demonstrating Moore's law, discovered in the year 1965 by Gordon Moore. He was the co-founder of INTEL Corporation. He made the drastic changes in the digital production field and he computed the cost range in the devices due to the increase in power and speed. He demonstrated that the increment in the transistor range in the semiconductor world would increase every 2 years in the range of two times. This prediction is also indicated as Moore's law. The designing process is carried out in the nanometer range in the current world.¹³

The transistor is restricted by the various constraints such as short channel effects (SCE), which are explained as the hot carrier effect and the tunneling effect through the doping layer thickness. In the process, arithmetic logic unit (ALU) is the main part of the circuit.¹⁴ The ALU unit includes the major element as the adder circuit. The major role of the adder circuit is to perform the arithmetic operations within the circuit. In some cases, adders act as a major part of the processor to calculate the address of the registers, index calculations, and other arithmetic operations.^{15,16}

By increasing the various requirements such as power, efficiency, and area in devices such as mobile phones, laptops, tablets, performances also increase in the integrated circuit.¹⁷ The adder



cells are used based on the requirements of the application, where the low power adder is used in low power applications and high power adder is used in the high power applications. This article implemented the use of adders using FinFET technology within the integrated circuit.¹⁸

1.2 | Design of conventional carry skip adder

The proposed work demonstrates the CSKA architecture, which is mainly aimed at reducing the delay by the reduction in the static FinFET logic. The main concept of static FinFET logic initializes from the wide range of variation in the supply voltage in the trending technologies.¹⁹ The projected technique will increase the speed of the circuit with the reduction in the area and the power consumption in the proposed CSKA. As by the changes in the architecture of the CSKA, the power consumption will be lower whereas the speed of the CSKA will increase. Most of the VLSI systems may include Low power consumption, smaller area occupation, and higher performance-based on speed and energy.²⁰ Most of the application such as movable and mobile devices, multi-standard receivers, and various instrumentation applications have low power consumptions.

The major component is included in the arithmetic unit is the adder circuit. This efficient adder designing includes the complex digital signal processing (DSP) system. This major design improves the performance of various applications.²¹

Adder that is represented as the basic block of the architecture in the arithmetic and logical unit (ALU) increases the speed and reduces the power and energy. By the impact of the adder, speed increases and the power of the processor will reduce within the logical circuit.²²

Many of the works of various researchers were involved in the optimization of speed and the energy that is influence by various parameters.²³ The designers felt difficulties in designing the circuit that varies the speed with the low power and the lower energy consumptions within the processors. The main technique used to lower various metric consumptions in the digital circuits will be based on the switching energy within the voltage.

When the adder circuit is in the sub-threshold state, the main leakage current is said to be low when the transistor is in the OFF state. Conventional carry skip adder (Conv-CSKA) is developed by ordering the full adders in the parallel form to design the ripple carry adder and that can be used for carrying propagation with the 2:1 multiplexer that includes the propagation block. In this proposed adder circuit, carry is skipped toward the i th position.²⁴ Figure 2 represents the working procedure concluded with two stages, namely, ripple carry adder block and the carry propagation block. The propagation block uses the EXOR gates, which produce the propagation bits. The generated bits will be fed toward the AND gates.

The outcomes of the propagation block are given toward the selection line of the multiplexer, which decides the carry bits. The proposed method can construct the 16-bit Conv-CSKA which includes the 920 transistors that can be subdivided into 608 transistors at the ripple stage and 80 transistors at the propagation stage for 2:1 multiplexer circuit.

The rest of this article includes the following sections. Section 2 includes the study of various survey as well as existing algorithm. Section 3 includes the various topology structures and the usage of FinFET technology. Section 4 includes the proposed structure of FinFET technology.

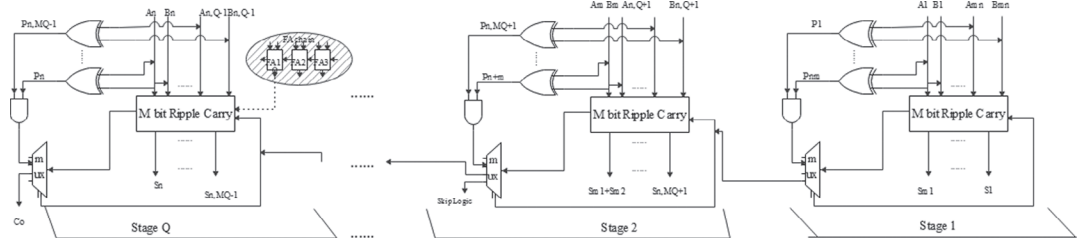


FIGURE 2 Conventional carry skip adder circuit

Section 5 includes the design and implementation of the proposed structure. Section 6 includes the experimental results and analysis of the proposed work.

2 | LITERATURE SURVEY

Many surveys had undergone to analyze the power and efficiency of the adders within the integrated circuit. Jiao et al⁹ proposed the structure of carrying skip adder (CSKA) that mainly undergoes the reduction in power with the increment in the speed due to lower energy consumption. The speed changes are carried out using the concatenation and incrimination schemes in the adder circuit. By the increment in the speed, the efficiency of the Conv-CSKA is re-arranged. The proposed technique includes the AND-OR-Invert (AOI) and OR-AND-Invert (OAI) compound gates for the skip logic. Thus the structure can be fixed by the various size of the adders and the variable stage size designs which improve the speed and energy parameters of the adders.

Guo et al²⁵ concluded fast and energy-efficient which has the 64-bit added to the high performance of the processor. Various adders have the highest power density processor blocks, with the thermal hotspot and the sharp temperature. The presence of the n number of ALU unit is the major factor in the superscalar processors, but the major disadvantage is the cooling cost is higher.

Stojanovic and Oklobdzija²⁶ developed that selection lines within the circuit that implements the performance of the devices. The performance mainly maintained by various sectors such as power and speed. Time consumption is also a major factor in the increment in performance analysis.

Jain et al⁶ discussed that the leakage power dissipation is within the circuit depends on the total power consumption and energy dissipated from the circuit. By the changes in the size and the frequency of the technologies, which is indicated in the nm factor, the sub-threshold value will be lower, which influences the performance within the circuit.

Borkar⁷ revised the switching component within the transistor circuit. By changing the leakage component within the transistor, the total energy will be reduced toward supply voltage. This in-turn produces the low voltage design but the drawback tends to be a reduction in the input power and lower energy. As from the study of the various proposed work, it is stated that higher the size of the circuit may increase the power and the energy of the devices. By designing the carry skip adder with the FinFET technology, power consumption can be reduced and energy consumption also reduces.



3 | ANALYZING ADDER TOPOLOGIES WITH THE FINFET TECHNOLOGY

3.1 | FinFET technology

In the parallel circuit, two terminals are represented as the source and the drain gate is represented together. FinFET was represented as the multigate device which is introduced by the researchers at the University of California in the year of 1999.⁷ Most of the designers made an interest in designing the circuit in FinFET technology. Many organizations, which include the IBM, Motorola, make use of FinFET technology. The main effect of the planar transistor is to design the reduced SCE, higher transconductance range, and lesser sub-threshold voltage.

3.2 | FinFET structure

FinFET that is the non-planar double gate transistor is constructed using silicon on insulator (SOI) substrate. The basic characteristic of the fin field effect transistor (FinFET) is the conduction channel binding using the thinner layer of silicon dioxide which is represented as a gate device. This channel length is determined by the width and the thickness of the fin formed. This is represented as the FinFET because of the thinner channel region which is similarly represented as the fin layer between the source and the drain regions within the transistor. The major extension of the gate is represented in the body with the three sides, whereas it reduces the SCE. The two terminals such as source and the drain are terminated together to lessen various effects that affect the performance of the transistor.

The second gate is added on the opposite side to represent the traditional gate of the transistor. But due to the lack of various problems arising in the front and back gates, the resistance value decreases in both the gates which is difficult to fabricate. The main reason to develop FinFET is to overcome the problems analyzed in DGFET. Double gates provided in the FinFET reduce the channel effect which in-turn increases the performance of the transistor. The basic structure of FinFET is shown in Figure 3A,B.

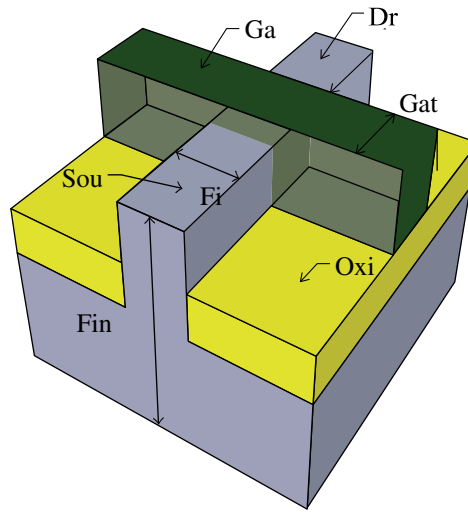
3.3 | Modes of operation

FinFET that is a three-terminal transistor works under the various modes of operation. FinFET consists of three methods, namely, shorted-gate (SG) mode, low power mode (LPM), and independent gate (IG) mode. The main architectural analysis depends upon the current dependence over the channel. As the FinFET operation depends on four modes, they can be detailed as follows.

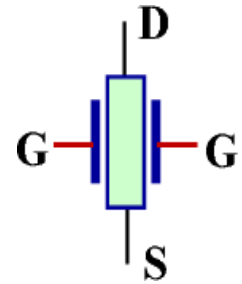
3.3.1 | Shorted-gate mode

When both the transistor tied together, it forms the three-terminal devices that are reacted as the replacement of conventional CMOS devices.

FIGURE 3 A, Basic structure of FinFET. B, Pin diagram [Color figure can be viewed at wileyonlinelibrary.com]



(A) Basic Structure of FinFET



(B) Pin Diagram

FIGURE 4 Shorted-gate (SG) mode FinFET

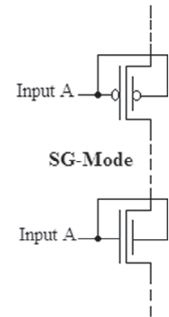


Figure 4 explains the SG mode of the transistor which has lesser power consumption and lesser leakage current.

3.3.2 | The independent-gate mode

The independency of the digital signals depends upon the device gates. One of the independent parts is the top gate which can be controlled separately by the processor. The IG mode includes various designing options based on different power consumptions, as shown in Figure 5.

They can be explained as the step by step process. By the initial processing, the current (I_{on}) will affect more in the transistor devices. The voltage level of the LP mode will be available at the range of -0.2 V for n-type transistors and 0.2 V for the p-type transistor.

3.3.3 | Low power mode

In this mode, the back gate of the transistor tends to increase the reverse bias voltage as well as the leakage power reduces. In the LPM, the back gate reduces the current which

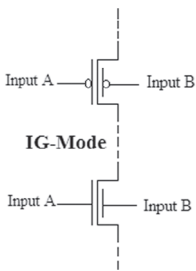


FIGURE 5 Independent-gate (IG) mode FinFET

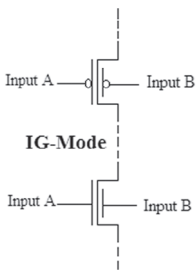


FIGURE 6 Independent-gate (IG) mode FinFET

is said to in the condition (I_{off}). The power supply tends to be -0.2 V which is n-type FinFET.

3.3.4 | Hybrid mode (IG/LP)

It involves the combination of two modes such as LP and IG modes. By various changes in the power supply, the mode of the transistors may vary which influences the performance of the processor. In various cases, FinFET considers having the front and back gates. The electrical properties are represented which tends to have low power and switch dependence. Figure 6 represents the IG mode that consists of two inputs A and B.

4 | FULL ADDER CIRCUIT USING DIFFERENT TOPOLOGIES

4.1 | FinFET based 1-bit transmission gate full adder

The full adder consists of various transmission gates (TGs) with a collection of 20 transistors. Transistors are made up of TGs, PMOS and NMOS logic within the system, which is represented in Figure 7. TGs are used in the circuit due to the increase in the speed and the decrease in the power dissipation within the transistor. The major factor affecting the circuit is the transistor count, intermediate nodes, and the lesser input range. This design is used in various applications due to its balanced generation of sum and output. The schematic of FinFET based 1-bit full adder circuit is shown in Figure 7.

FinFET technology has implemented with the shorted-gate (SG) FinFET and IG. The proposed methodology consists of SG FinFET technique, which would reduce the delay and the power consumption within the circuit. In the FinFET technology, two gates are connected with

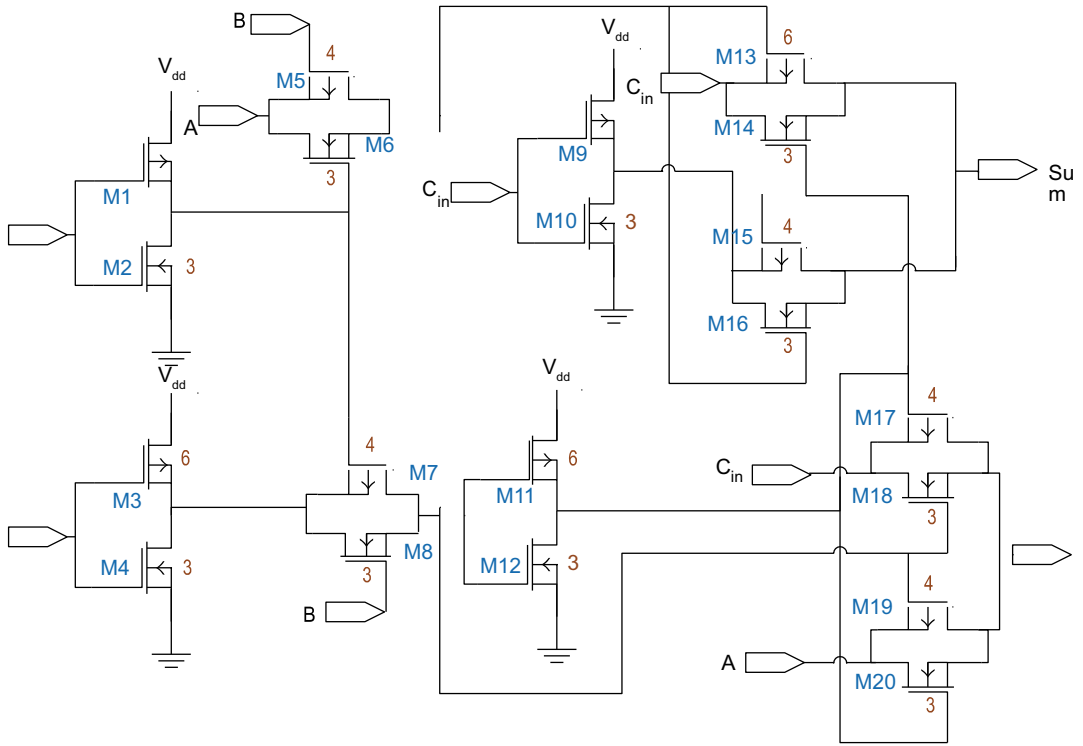


FIGURE 7 FinFET based 1-bit full adder circuit [Color figure can be viewed at wileyonlinelibrary.com]

the replacement of conventional carry skip CMOS devices. For SG mode, different kinds of load are applied and can be mode can suit all kinds of load values which do not affect the performance of the devices. The major task within the SG mode is the leakage voltage will be higher.

By the comparison with the LP mode, the leakage current is lesser and the switching capacitance will be reduced. But the performance of the mode will be slow due to the load and the area consumption. The main advantage of IG mode is to perform with the low area and the lesser capacitance. This designing mode comprises higher leakage due to the pull-up and pull-down mode. For IG/LP design mode, the advantages are low leakage, low switched capacitance, and low area.

5 | CONVENTIONAL CSKA STRUCTURE

The proposed work consists of the combination and incrementation techniques with the conventional-CSKA structure with the 15 nm FinFET technology. The structure implemented is denoted as the CI-CSKA. The basic carry skip logics have been used in the circuit. The designed structure consists of 2:1 multiplexers which are replaced by the AOI and OAI compound gates as shown in the figure. These gates include the lesser number of transistor circuits which affects the low delay and low area consumption and reduction in the power usage which is compared with the 2:1 multiplexer design. The complementation of the skip logic is the major usage in the proposed work. By the outcome in the even stage of the carry skip adder, the

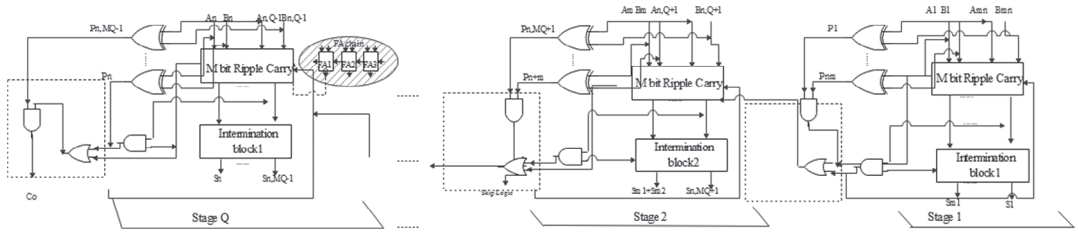


FIGURE 8 Proposed CI-CSKA structures

complementary form of carrying is produced. The main advantage of the implemented work is the lower propagation delay within the smaller area consumption as compared with the conventional logic.

The point to be concluded that the power consumption within the AOI (or OAI) gate is lesser as compared with the existing multiplexer. By increasing the number of gates, the power consumption within the circuit is slightly low when compared with the conventional logic. With the complicated wiring capacitance, the performance cannot be affected as they have no critical values as the load.

The proposed internal structure is shown in Figure 8, which is explained as follows. The adder which is implemented consists of N bits with two inputs A, B with Q stages. Each step is represented as a separate RCA block where the first block tends to be represented as Ci which tends to be zero. The first block is presented with the summing amount of input bits which act as an intermediate result.

The main reason for using the transistor logic such as AOI and OAI is due to the compound gate characteristics. These compound gate acts as skip logic in the carry skip adder by the changes of the gate into the inverting functions with the standard cell functions within the libraries.

The transistor logic acts as an inverted gate circuit. By considering inversion process, will reduce the power consumption and delay within the circuit. When the AOI acts as skip logic, the next logic is implemented using the OAI gate. The proposed skipping structure in the CI-CSKA decreases the delay within the circuit whereas the critical path increases.

5.1 | Proposed 8 T carry skip adder

The proposed work consists of designing of adder using an 8-T approximate carry skip adder with the help of FinFET technology. In the 15 nm FinFET, processing tends to be common, which has a higher performance based on the power and the efficiency of the processor. Due to this factor, these adders are used for higher commercial applications. The significance of using FinFET technology is lower power consumption and higher speed in terms of integrated chip processing. The proposed technique is implemented using the HSPICE and LTSPICE simulation tool at 15 nm FinFET technology. The schematic view of the FINFET technology-based 8 T carry skip adder at 15 nm is shown in Figure 9

By using the 8 T approximate adder power, the delay of the transistor decreases within the processing technology. The result also suits the 32-bit approximate adder but the delay of the adder will be increased. When the transistor count increases, power consumption will be reduced.

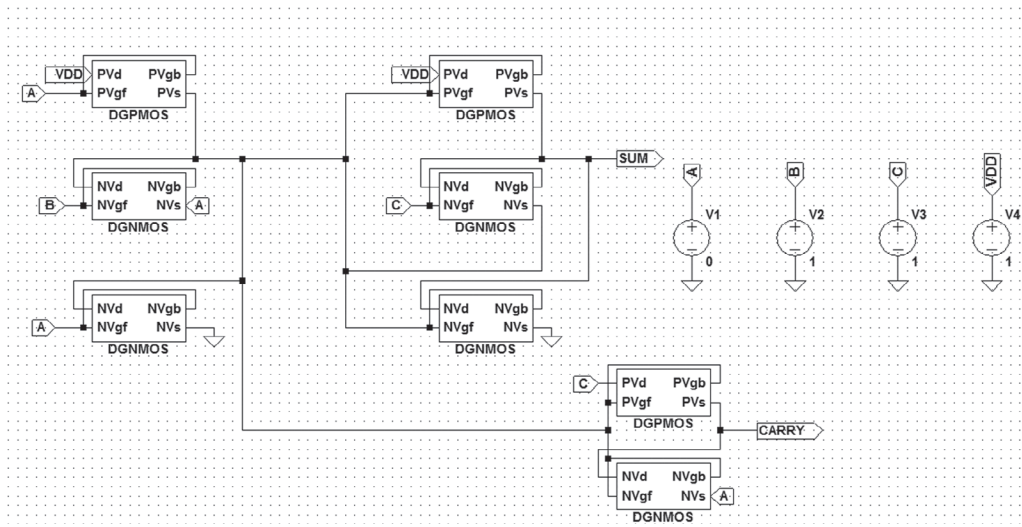


FIGURE 9 Schematic representation of 8 T adder

TABLE 1 Output for accurate and approximate adder

Inputs			Accurate Outputs		Approximate adder outputs		
A	B	C _{in}	s	C _{out}	S	C _{out}	ED
0	0	0	0	0	0	0	0
0	0	1	1	0	1	0	0
0	1	0	1	0	1	0	0
0	1	1	0	1	0	1	0
1	0	0	1	0	1	0	0
1	0	1	0	1	0	1	0
1	1	0	0	1	1	1	0
1	1	1	1	1	0	1	0

The implemented adder technique is used for image processing applications. The outcomes of the accurate and approximate adder are shown in Table 1.

The image processing applications consists of approximate adder which mainly focused on the time- based consumption and different power supply voltages. The value of the parameters may vary with the changes in the input voltage and the leakage current. Based on the implemented work, the density of the capacitance increases which is also implemented in mobile and RF applications.

Figure 10 explains the proposed output waveform of the 8T adder circuit. When the input voltage increases, the output, which represents the sum and the carry, decreases according to the voltage level. The major applications of the proposed work are image processing and speech recognition. The approximate adder circuit results in the multimedia imaging system whereas the output voltage consumed more power. This can be varying from the critical and non-critical data points.

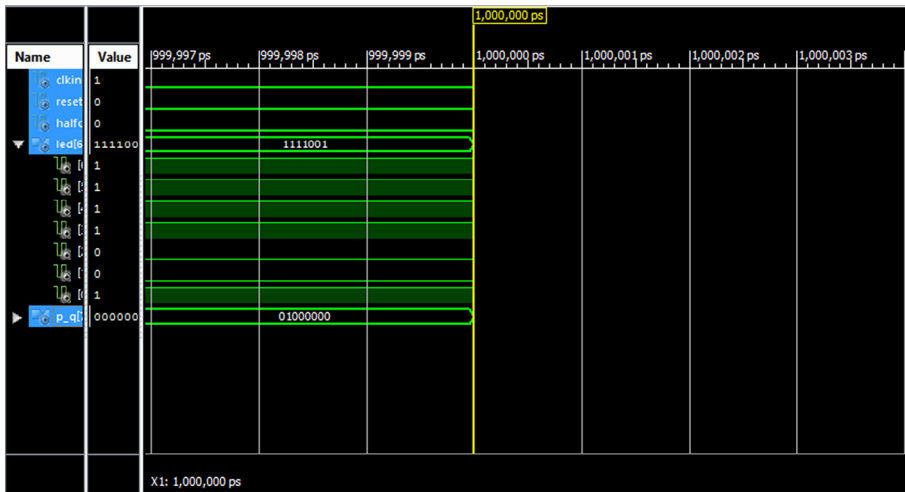


FIGURE 10 Simulated waveform for proposed 8-T carry skip adder [Color figure can be viewed at wileyonlinelibrary.com]

Parameter	Value
Fin height (H _{fin})	70 nm
Fin thickness (TSI)	15 nm
Oxide thickness (T _{ox})	1.1 nm
N-channel surface orientation	<105>
Length of gate (LG)	25 nm
Source to gate/drain underlap (LSD)	10 nm
Gate thickness (TG)	20 nm
Gate work function (Φ_G)	4.4 eV (n-type) 4.8 eV (p-type)
Mobility	560 cm ² /(V-s) (n-type) 200 cm ² /(V-s) (p-type)
Doping of fin body (N _{body})	1014 cm ⁻³
Drain/Source resistance (RSD)	180 Ω - μ m
Voltage supply (VDD)	1 V
Source/drain doping (NDS)	1020 cm ⁻³

TABLE 2 FinFET technology model

6 | EXPERIMENTAL RESULTS AND ANALYSIS

The proposed technique gives the detailed outcome of the FinFET technology with the 8T carry skip adder with the following parameters. The 15 nm length is set towards the FinFET technology which tends to be a next-generation process in the device performance. Table 2 represents the initial parameters of the proposed FinFET technology.

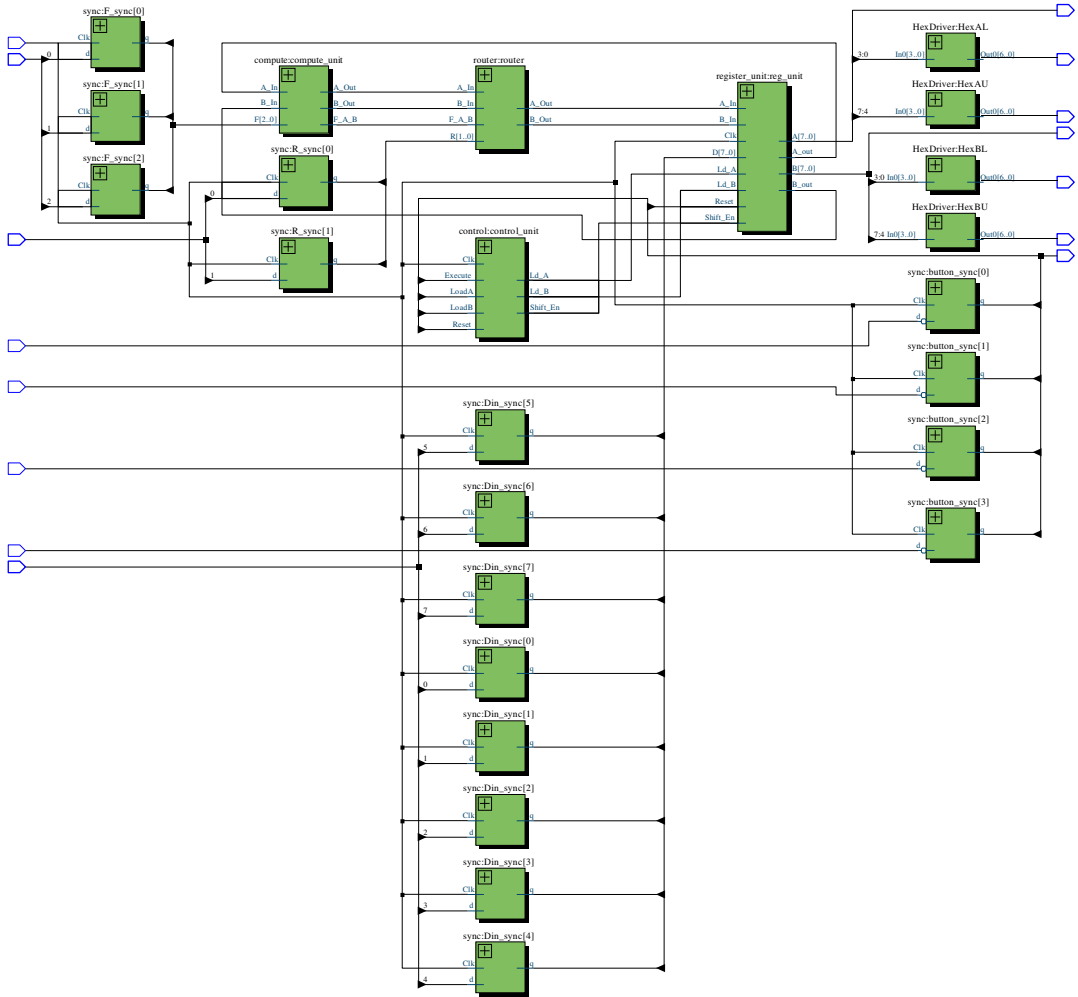


FIGURE 11 Schematic representation of 8-bit adder with the FinFET technology [Color figure can be viewed at wileyonlinelibrary.com]

The schematic representation of 8T adders with the FinFET technology is represented in Figure 11. Based on the designing structure, the channel width of the FinFET technology is represented as W_{eff} . Thus the FinFET technology width can be calculated with the following parametric calculations.

$$W_{eff} = NFIN \times (TFIN + 2HFIN). \tag{1}$$

In the above equation, NFIN is represented as the number of FIN transistors which is aligned in the parallel form, while the TFIN represents the thickness of the FinFET and the HFIN represents the height of the proposed technique.

The given schematic representation represents the 8T adder implementation in FinFET technology using the HSPICE simulation tool, as shown in Figure 12. The transistors simulated in the HSPICE tool which is used to optimized parameters. The width of the proposed method varies with the current flowing inside the drain terminal which is approximately at the range of 61.5 and 48 nA at both the types of transistor.

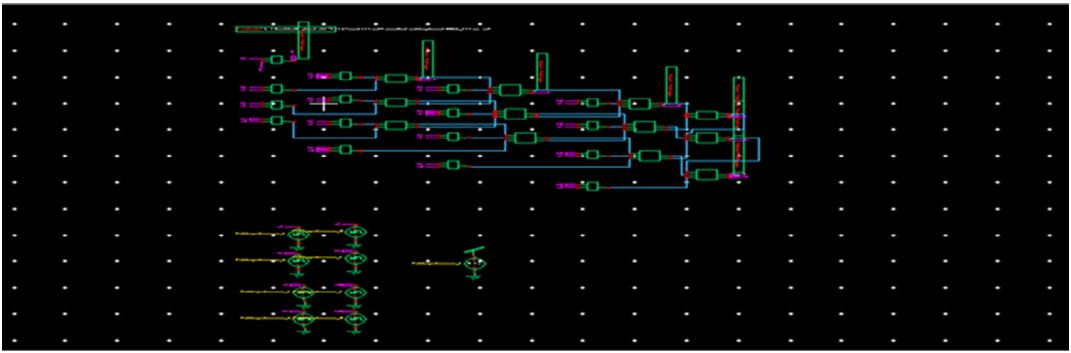


FIGURE 12 Schematic representation of 8 T carry skip adder with the FinFET technology [Color figure can be viewed at wileyonlinelibrary.com]

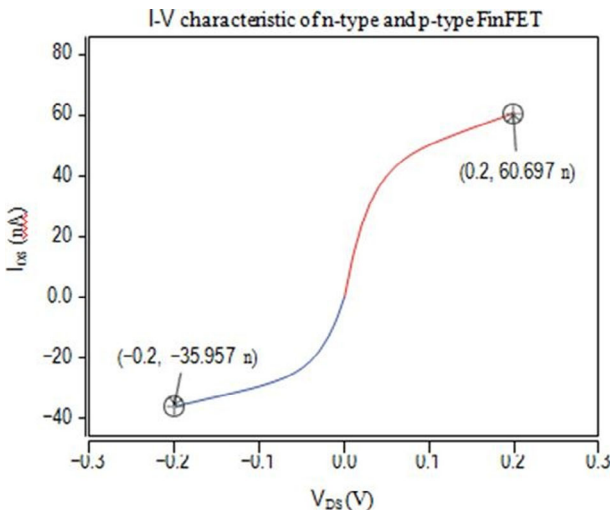


FIGURE 13 Graph of I_{DS} versus V_{DS} of FinFET [Color figure can be viewed at wileyonlinelibrary.com]

The plot of I_{DS} versus V_{DS} of FinFET technology is the same as that of the MOSFET. The flow of the voltage and the current depends upon the height of fin (TFIN), and the number of fins (NFIN) is chosen carefully to obtain a matching drain current of n-type and p-type FinFET against MOSFET. From our simulation, we suggest that the respective values of TFIN and HFIN for all n-type and p-type channel be kept consistent.

For the FinFET technology, input and the output waveform of the 8T adder circuit are illustrated in Figure 13, respectively. The output generated will have some of the glitches due to a large number of transistor counts. The output has the rising and fall due to the TG within the FinFET technology in the cell design.

Table 3 shows the drain current analysis of 8T carry skip adder with the comparison with the FinFET as well as MOSFET technology. As the height, thickness and transistor count changes the drain current within the processor changes. Figures 14 and 15 show the graphical analysis of 8T carry skip adder in FinFET technology and output waveforms of 8T carry skip adder in FinFET technology.

As the main advantage of the proposed work is the reduction in power consumption as compared with the existing system. By the decrease in the power consumption, the delay within the

TABLE 3 The values of the drain current of FinFET and MOSFET transistors

Number of transistors in series	MOSFET		FinFET			
	Width (nm)	Current (nA)	TFIN (nm)	HFIN (nm)	NFIN	Current (nA)
N-type						
1	16.00	61.49	10.00	10.00	1	65.79
2	32.00	97.08	10.00	10.00	2	131.57
3	48.00	166.23	10.00	10.00	3	197.36
4	64.00	235.19	10.00	10.00	4	263.14
8	128.00	510.75	10.00	10.00	8	526.29
10	160.00	648.18	10.00	10.00	10	657.86
P-type						
2	32.00	47.37	17.00	17.00	2	63.32
4	64.00	116.38	17.00	17.00	4	126.64
5	80.00	150.86	17.00	17.00	5	158.30
6	96.00	185.33	17.00	17.00	6	190.00
8	128.00	254.26	17.00	17.00	8	253.30
8/3	42.66	70.377	17.00	19.00	2	70.77
9	144.00	288.73	17.00	17.00	9	283.90
12	192.00	392.11	17.00	17.00	12	379.90

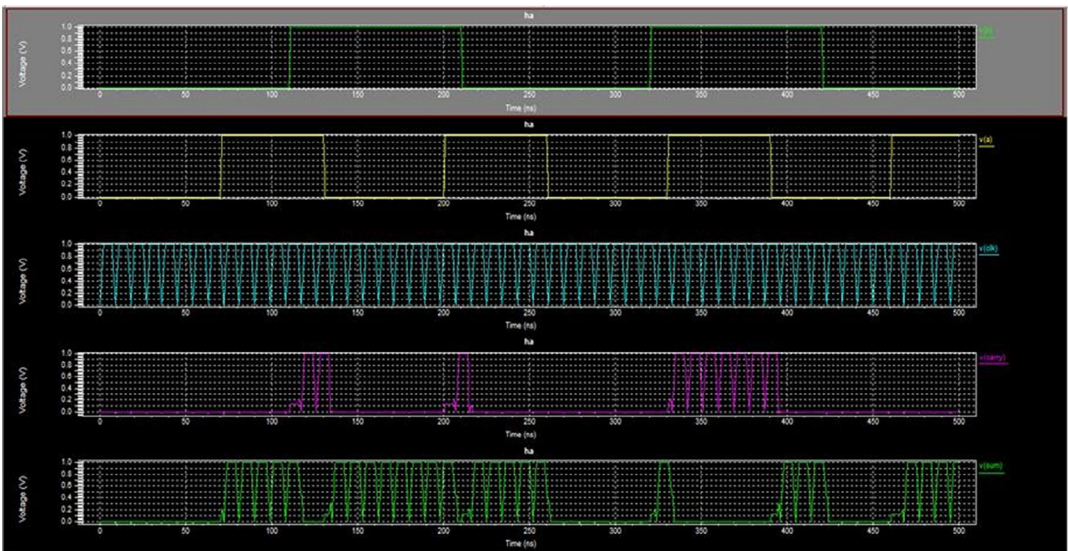


FIGURE 14 Graphical analysis of 8 T carry skip adder in FinFET technology [Color figure can be viewed at wileyonlinelibrary.com]

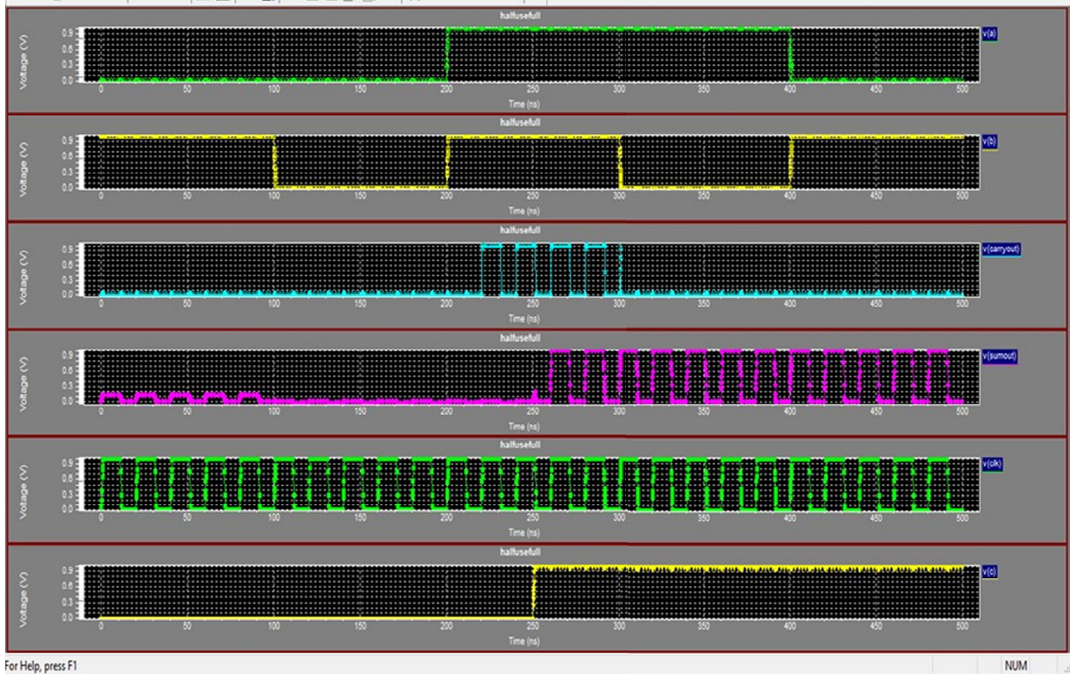


FIGURE 15 Output waveforms of 8 T carry skip adder in FinFET technology [Color figure can be viewed at wileyonlinelibrary.com]

processor decreases, whereas the speed of the system increases. The presence of multiple gates in the FinFET technology reduces the channel effects within the system. By the enhancement in the gate oxide thickness, the leakage current decreases, which, in turn, reduces the power dissipation. Figure 16 represents the power consumption and the power dissipation of the proposed system.

The cell design characteristic of FinFET technology is shown in Figure 17. This will indicate the rising and falling of the voltage concerning the time dependence.

The power delay can be measured with the calculation of energy consumed during the switching event. Energy delay is calculated using the energy dissipated during the switching time. The following equation indicates the delay calculation within the proposed system.

$$\text{Power delay} = \text{Propagation Delay} \times \text{Average Power Dissipation}$$

$$\text{Energy delay} = \text{Power Delay} \times \text{Propagation Delay}$$

Figure 18 represents the power delay and the energy delay within the proposed system.

Power delay and the energy delay are due to the various characteristic parameters, namely, higher amounts of speed and the swing operation with the full form. The speed of the full adder cell can be maximized with the switching operation which also increases the cost of the processor.



```

9.425000e-008 9.9998e-001 1.7016e-005 1.7016e-005 1.7016e-005 9.9998e-001 1.7519e-005 2.2553e-005 1.7003e-005
9.425000e-008 9.9998e-001 1.7016e-005 1.7016e-005 1.7016e-005 9.9998e-001 1.7519e-005 2.2553e-005 1.7003e-005
9.825000e-008 9.9998e-001 1.7016e-005 1.7016e-005 1.7016e-005 9.9998e-001 1.7819e-005 2.2533e-005 1.7003e-005
1.000000e-007 9.9998e-001 1.7016e-005 1.7016e-005 1.7016e-005 9.9998e-001 1.7519e-005 2.2553e-005 1.7003e-005

* BEGIN NON-GRAPHICAL DATA
Power Results
vdd gnd from time 0 to 1e-007
Average power consumed -> 4.842503e-004 watts
Max power 4.842503e-004 at time 1e-008
Min power 4.842503e-004 at time 8.6875e-009

* END NON-GRAPHICAL DATA
|
* Farsing                0.01 seconds
* Setup                  0.22 seconds
* DC operating point     1.00 seconds
* Transient Analysis     0.73 seconds
* Overhead               1.81 seconds
*-----
* Total                  3.77 seconds

* Simulation completed with 1 Warning
* End of T-Spice output file
    
```

(A)

```

4.882500e-007 8.6401e-001 5.5669e-003 1.2120e-003 3.9770e-004 4.8091e-004 3.3026e-004 1.5622e-004 1.4383e-004
4.899999e-007 8.6401e-001 5.5669e-003 1.2120e-003 3.9770e-004 4.8091e-004 3.3026e-004 1.5622e-004 1.4383e-004
4.902500e-007 8.6401e-001 5.5669e-003 1.2120e-003 3.9770e-004 4.8091e-004 3.3026e-004 1.5622e-004 1.4383e-004
4.922500e-007 8.6401e-001 5.5669e-003 1.2120e-003 3.9770e-004 4.8091e-004 3.3026e-004 1.5622e-004 1.4383e-004
4.942500e-007 8.6401e-001 5.5669e-003 1.2120e-003 3.9770e-004 4.8091e-004 3.3026e-004 1.5622e-004 1.4383e-004
4.962500e-007 8.6401e-001 5.5669e-003 1.2120e-003 3.9770e-004 4.8091e-004 3.3026e-004 1.5622e-004 1.4383e-004
4.982500e-007 8.6401e-001 5.5669e-003 1.2120e-003 3.9770e-004 4.8091e-004 3.3026e-004 1.5622e-004 1.4383e-004
5.000000e-007 8.6401e-001 5.5669e-003 1.2120e-003 3.9770e-004 4.8091e-004 3.3026e-004 1.5622e-004 1.4383e-004

* BEGIN NON-GRAPHICAL DATA
Power Results
vdd gnd from time 0 to 5e-007
Average power consumed -> 6.250000e-012 watts
Max power 6.250000e-012 at time 0
Min power 6.250000e-012 at time 0

* END NON-GRAPHICAL DATA
*
* Farsing                0.00 seconds
* Setup                  0.04 seconds
* DC operating point     0.01 seconds
* Transient Analysis     0.16 seconds
* Overhead               1.39 seconds
*-----
* Total                  1.60 seconds
    
```

(B)

FIGURE 16 A,B, Power consumption of proposed FinFET technology for various inputs

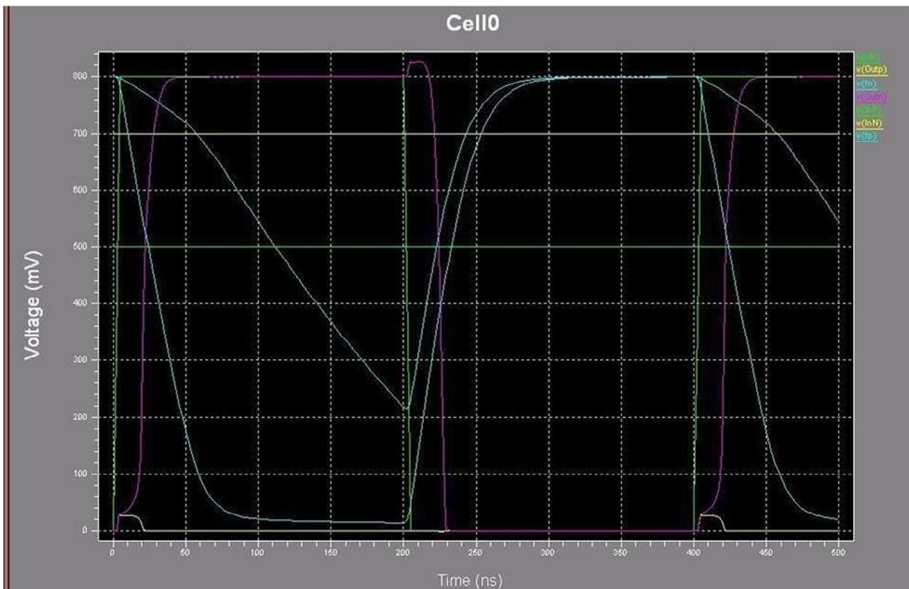


FIGURE 17 Cell design characteristic of the 15 nm FinFET technology [Color figure can be viewed at wileyonlinelibrary.com]

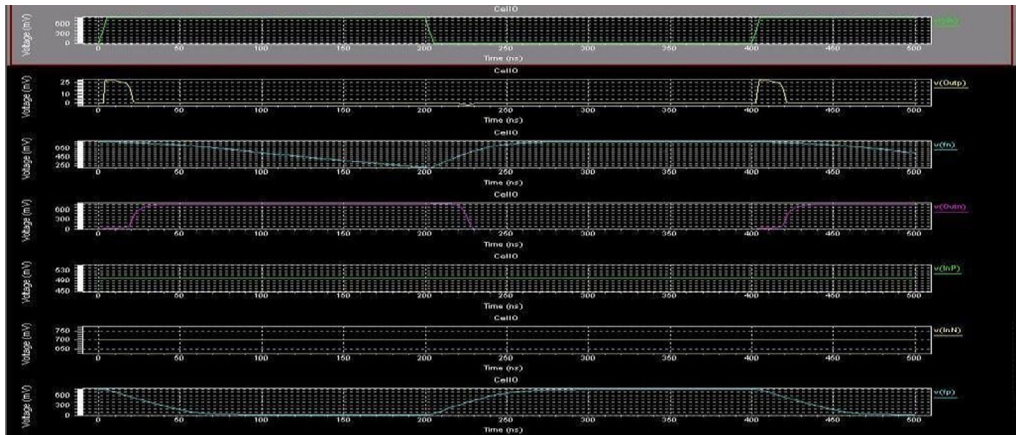


FIGURE 18 Power delay and energy delay of the proposed work [Color figure can be viewed at wileyonlinelibrary.com]

7 | CONCLUSION

This implemented work consists of 8 T carry skip adder which is derived from the Conv-CSKA. This discussed that adder consumes the total power up to 20%. The number of transistors used within the proposed technique is lesser than that of the existing methods. In the existing methods, the output tends to have a little impact on the performance of the circuit. From the proposed designing structure, we can able to design the 32-bit adder circuit which can be used in the DSP applications. The proposed technique is implemented in the HSPICE simulation tool which is analyzed using metrics such as propagation delay, power dissipation, power delay, and energy delay. Based on the findings of 8T FinFET technology, it is concluded that the proposed FinFET technology has lesser tradeoff as compared with the MOSFET adders.

DATA AVAILABILITY STATEMENT

Data openly available in a public repository that issues datasets with DOIs. The data that support the findings of this study are openly available in public websites. Data openly available in a public repository that does not issue DOIs. The data that support the findings of this study are openly available in UCI repository.

ORCID

N. Duraivel  <https://orcid.org/0000-0002-2592-1434>

REFERENCES

1. Hwang K. *Computer Arithmetic: Principles, Architecture, and Design*. New York, NY: Wiley; 1979.
2. Jang YJ, Shin Y, Hong MC, Wee JK, Lee S. Low-power 32 bit \times 32 bit multiplier design with pipelined block-wise shutdown. Paper presented at: 12th International Conference on High Performance Computing-HiPC 2005; Goa, India: Springer; Vol. 3769; 2005: 398-406.
3. Huang Z. High-Level Optimization Techniques for Low-Power Multiplier Design [Ph.D. thesis]. University of California. 2003.

4. Junming L, Yan S, Zhenghui L, Ling W. A novel 10-transistor low-power high-speed full adder cell. Paper presented at: 6th International Conference on Solid-State and Integrated-Circuit Technology; 2001:1155-1158.
5. Jiang Y, Al-Sheraidah A, Wang Y, Sha E, Chung J-G. A novel multiplexer-based low-power full adder. *IEEE Trans Circ Syst II: Exp Briefs*. 2004;51:345-348.
6. Jain S. A 280 mV-to-1.2 V wide-operating-range IA-32 processor in 32 Nm CMOS. Paper presented at: IEEE International Solid-State Circuits Conference. Digest of Technical Papers (ISSCC), Belgium: February, 2012: 66-68.
7. Borkar S. Designing reliable systems from unreliable components: the challenges of transistor variability and degradation. *IEEE Micro*. 2005;25(6):10-16.
8. Markovic D, Wang CC, Alarcon LP, Liu T-T, Rabaey JM. Ultralow-power design in near-threshold region. *Proc IEEE*. 2010;98(2):237-252.
9. Jiao X, Akhlaghi V, Jiang Y, Gupta RK. Energy-efficient neural networks using approximate computation reuse. Paper presented at: 2018 Design, Automation and Test in Europe Conference & Exhibition (DATE): Europe: IEEE; March, 2018:1223-1228.
10. Liu Y, Furber S. The design of an asynchronous carry-lookahead adder based on data characteristics. Paper presented at: 15th International Workshop on Power and Timing Modeling, Optimization and Simulation, PATMOS 2005; Integrated Circuit and System Design; Leuven, Belgium: Springer; Vol. 3728; 2005: 647-656.
11. Tiwari K, Khopade A, Jadhav P. Optimized carry look-ahead BCD adder using reversible logic. Paper presented at: First International Conference on Technology Systems and Management Communications in Computer and Information Science, ICTSM 2011; Mumbai, India: Springer; Vol. 45; 2011: 260-265.
12. Weinberger A, Smith JL. A logic for high speed addition. *Nat Bur Stand Circul*. 1958;591:3-12.
13. Kavehei O, Rahimi Azghadi M, Navi K, Mirbaha AP. Design of robust and high-performance 1-bit CMOS full adder for nanometer design. Paper presented at: IEEE Computer Society Annual Symposium on VLSI, VLSI 08; Montpellier, France; 2008:10-15.
14. Haghparast M, Navi K. A novel reversible BCD adder for nanotechnology based systems. *Am J Appl Sci*. 2008;5(3):282-288.
15. Gogoi A, Kumar V. Design of low Power, area efficient and high-speed approximate adders for inexact computing. *IEEE Trans Very Large Scale Integr Syst*. 2016;452-456.
16. Aguirre-Hernandez M, Linares-Aranda M. CMOS fulladders for energy-efficient arithmetic applications. *IEEE Trans Very Large Scale Integr Syst*. 2011;19(4):718-721.
17. Chang CH, Gu JM, Zhang M. A review of 0.18- μm full adder performances for tree structured arithmetic circuits. *IEEE Trans Very Large Scale Integr Syst*. 2005;13(6):686-695.
18. Gupta V, Mohapatra D, Raghunathan A, Roy K. Low power digital signal processing using approximate adders. *IEEE Trans Comput-Aided Design Integr Circuits Syst*. 2013;32(1):124-137.
19. Liang J, Han J, Lombardi F. New metrics for the reliability of approximate and probabilistic adders. *IEEE Trans Comput*. 2013;62(9):1760-1771.
20. Taur Y, Ning TH. *Fundamentals of Modern VLSI Devices*. New York, NY: Cambridge University Press; 1998.
21. Shrivastava M, Baghni MS, Sharma DK, Rao VR. A novel bottom spacer FinFET structure for improved short-channel, power delay, and thermal performance. *IEEE Trans Electr Devices*. 2010;57(6): 1287-1294.
22. Rostami M, Mohanram K. Dual-V_{th} independent-gate FinFETs for low power logic circuits. *IEEE Trans Comp Aided Des*. 2011;30(3):337-349.
23. Bhoj AN, Jha NK. Design of logic gates and flip-flops in high-performance FinFET technology. *IEEE Very Large Scale Integr Syst*. 2013;21(11):1975-1988.
24. Guo Z, Balasubramanian S, Zlatanovici R. FinFET based SRAM design. Paper presented at: IEEE Transaction on Proceedings of 2005 International Symposium on Low Power Electronics and Design, California, USA: August, 2005:2-7.
25. Guo Z, Balasubramanian S, Zlatanovici R, King TJ, Nikolić B. FinFET-based SRAM design. Paper presented at: Proceedings of the 2005 International Symposium on Low Power Electronics and Design, San Diego: ACM; August, 2005:2-7.



26. Stojanovic V, Oklobdzija VG. Comparative analysis of master-slave latches and flip-flops for high-performance and low-power systems. *IEEE J Solid State Circuits*. 1999;34(4):536-548.

How to cite this article: Duraivel N, Paulchamy B. Simulation and performance analysis of 15 Nm FinFET based carry skip adder. *Computational Intelligence*. 2020;1–20. <https://doi.org/10.1111/coin.12417>



Tumor Categorization Model (TCM) Using Soft Computing Techniques for Providing Efficient Medical Support in Brain Tumor Treatments

V. Vinoth Kumar^{1,*} and B. Paulchamy²

¹Research Scholar, Department of Electronics and Communication Engineering, Angel College of Engineering and Technology, Tirupur 641665, Tamilnadu, India

²Department of Electronics and Communication Engineering, Hindusthan Institute of Technology, Othakalmandapam 641032, Tamilnadu, India

Brain cancer identification and segmentation is a prolonged and difficult task in Medical Image Processing, which is most significant for providing appropriate treatment and increase patient's life span. With the advancements available in medical fields, soft computing techniques are incorporated to accurate detection and classification of brain tumors. Besides brain cancer detection, it is vital to categorize tumor stage based on their features. For that concern, this paper develops a Tumor Categorization Model (TCM) that includes image processing and soft computing techniques. Here, pre-processing is carried out using modified Gabor filter and segmentation process is performed with OTSU thresholding. Following segmentation, region growing is processed based on the pixel intensities of input MRI brain images. Further, Discrete Wavelet Transform is enforced for extracting image features as well as gray-level co-occurrence matrix features are also derived for appropriate classifications. Finally, the input MRI images are classified using Boosting Support Vector Machine (BSVM) with the benchmark dataset called DICOM and BraTS dataset. The experimental results demonstrate accurate brain tumor detection and categorization by the efficient incorporation of image processing and soft computing methodologies, provides efficient clinical support in providing treatments.

Keywords: Tumor Categorization Model (TCM), MRI Brain Images, Discrete Wavelet Transform (DWT), Segmentation, Boosting Support Vector Machine (BSVM).

1. INTRODUCTION

In current scenario of medical sciences and digital health care systems, several clinical services are provided to provide better treatment for patients and to make appropriate decisions on clinical practices. Among several medical services provided by e-health systems, automated tumor detection mechanisms are very much significant. There are several kinds of clinical data processing that includes inputs from CT scan, MRI, X-ray and so on [1]. MRI-Magnetic Resonance Imaging of the Human Brain is one of the techniques used to diagnose brain cancer, which is one of the most severe and life-threatening disorders. Moreover, the MRI scan denotes the elements of cerebrum of brain effectively in addition to the point to point image specifications. The MRI images portray the brain tissues structure, functions and metabolism in non-invasive manner [2]. Based on the statements of Central Brain Tumor Registry of the United States (CBTRUS), brain cancer is uppermost death causing diseases than other kind of cancers [3]. For avoiding that, earlier detection

of brain tumor is more significant and methodologies are to be determined accordingly.

In this paper, soft computing models are incorporated for the analytical computation and reasoning capabilities. Some of the majorly used soft computing techniques are Evolutionary algorithm, support vector machine, fuzzy based methods, neural networks, and so on. The general work process for clinical data processing in cancer diagnosis is presented in Figure 1 that incorporates image processing and soft computing techniques.

Based on the classification results provided by the defined technique, the treatment decisions can be taken by the health practitioners. Specifically, for tumors, the patients are advised to undergo radiation, chemotherapy or surgery based on the grade of the detected tumor. This appropriate or effective decision making enhances the survival rates of patients; even the earlier tumor diagnosis can reduce the patient sufferings in considerable manner [4]. Hence, the research related to brain tumors with image processing has gained significance in the department of medical sciences. With such a goal in mind, this study presents the Tumor Categorization Model (TCM), a model for classifying

*Author to whom correspondence should be addressed.

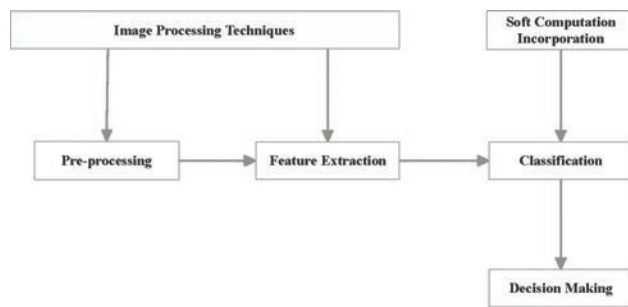


Fig. 1. Medical data processing for disease diagnosis.

cancer images according to their stages. Some of problems found in brain tumor diagnosis are listed below:

- As the size of the cancer tissues increases, it may completely damage the brain and other parts of the body too.
- The lesser number of training images would lead to reduced classification performance. Thus the required accuracy level can't be reached.

Here, the modality utilized for brain tumor detection is MRI images, since, it contains better image resolution. The acquired brain images are given for noise removal to the modified Gobar filter and OTSU thresholding is used for segmentation. For extracting significant features for appropriate classification, DWT and gray level occurrence matrix is employed and features are selected using Lion Optimization. Further, classification process is done through Boosting Support Vector Machine (BSVM).

2. RELATED STUDIES

The Ref. [5], Local Binary Patterns based image processing has been carried out for extracting the local features of the input images. Moreover, the original spectral and gabor features were extracted using two fusion techniques such as decision and feature level fusion techniques. In Ref. [6], a comparative evaluation has been carried out between the Cascade Architecture and Feed Forward Neural Networks based classifications. And, Principal Component Analysis (PCA) based feature extraction was incorporated. The dataset images were obtained from the Olivetti Research Lab database dataset for training and testing for the classification evaluations.

A hybrid model has been defined in Ref. [7] that used Fuzzy C-Means clustering and SVM for brain cancer diagnosis as well as classification. Moreover, image enhancement methods have been used to enhance the image features for appropriate results. Before applying classification model, feature extraction has been performed with the Grey level run length matrix. Further, an ensemble based classification technique has been presented in Ref. [8] to improve the accuracy of classification in brain cancer detection and classification.

Unsupervised learning models were used in Ref. [9] such as FCM for tumor image classification, specifically spatial FCM was used in the process. Active contour modelling was also been used for determining the cancer tissue border in precise manner [10]. The authors of Ref. [11] presented the tumor detection model with minimal processing time using the morphological functions. Additionally, it is to be stated that the computational cost of detection process is based on the storage and processing time [12].

Therefore, feature reduction process was presented in Ref. [13] for reducing the number of features that are chosen for classification process. Furthermore, in the work [14], the local features of MRI images such localization, frequency, was observed with the Gabor wavelet factors.

In some other papers, the feature extraction have been processed with GLCM, grey level run length matrix and first order statistical features [15]. In Ref. [16], combined classification model with BPNN in addition to SVM are employed to determine accurate MRI image categorization. In general, the NN based classification takes longer processing time, since it requires to process with training and testing process. The limitation can be effectively handled and overcome using support vector machine [16].

Automated brain tumor detection has been presented in Ref. [17], which used K-means clustering and morphological function based feature selection. Further, the authors of Ref. [18] used rapid Fourier transform for feature extortion of MRI images, to reduce the number of extracted features, minimal redundancy and maximal relevance model. The brain image contains both normal and abnormal cells that are to be segmented with effective models [19]. For accurate tumor image segmentation, the authors of Ref. [20] used the combination of FCM and seed growing methods. Wavelet transform related feature extortion to detect breast cancer was described in Ref. [21].

In the work [22], the outcomes of PCA and kernel functions were given to the SVM classification to detect the tumor appropriately [28]. And, in Ref. [23], Artificial Neural Network (ANN) based classification was used for MRI brain image classification. In a different manner, localized fuzzy clustering has been used for extracting the spatial data of images in Ref. [24]. Moreover, Jaccard Similarity measurement is employed to segment brain image depending on white, gray parts and cerebrospinal fluids.

Based on the image intensities, active contour based segmentation has been applied in Ref. [25] that support exact tumor diagnosis with enhanced image features using Gaussian Mixture method. Further, in the work [26], a hybrid model that combined PCA and ANN has been used for MRI brain tumor classifications. By analysing the works presented in this survey, a new idea is framed for implementing an efficient model for brain tumor diagnosis and classification that provides better accuracy than other models.

3. WORK PROCESS OF TUMOR CATEGORIZATION MODEL WITH EFFICIENT IMAGE PROCESSING AND SOFT COMPUTING METHODS

The proposed Tumor Categorization Model (TCM) acquires MRI brain images as input and processed with image processing and soft computing techniques for producing appropriate classification results. Further, the classified tumor images are categorized into specific stages for supporting medical practitioners for treatment decision making. The functions involved in the proposed mode are diagrammatically presented in Figure 2.

3.1. Image Acquisition

Here, Magnetic Resonance Imaging of Brain samples are given as the input for the proposed model. However, MRI inputs contain some noise that may cause incorrect classifications. Hence,

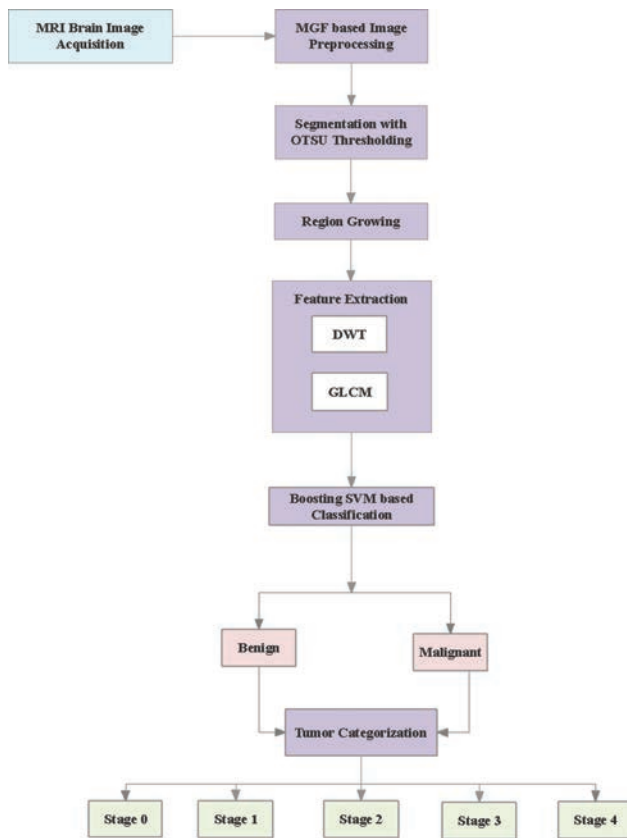


Fig. 2. Functions involved in proposed model.

input samples are processed and segmented for obtaining accurate brain tumor detection.

3.2. Pre-Processing with Modified Gabor Filter

The input brain samples are pre-processed here with Modified Gabor Filter, which is different from the gabor filter operations with minimal time consumption for processing. Moreover, the operations involved in the modified gabor filter based image processing are given as follows:

- Initially, the spatial aspect ratio are not considered, thereby, distortion of samples are reduced effectively.
- Instead, the spatial aspect ratio is taken directly at the kernel size.
- This reduces the noise level effectively and helps to obtain clear MRI samples for further processing.

Moreover, the mathematical computations involved in the Modified Gabor Filter Processing are described below:

$$f(x, y; \alpha, \theta, \gamma, \delta) = \exp \left[-\frac{1}{2} \left(\frac{x_1^2 + y_1^2}{\alpha^2} \right) \cos \cos \left(2\pi \left(\frac{x_1}{\delta} \right) + \gamma \right) + \sin \left(2\pi \left(\frac{y_1}{\delta} \right) + \gamma \right) \right] \quad (1)$$

Where $x_1 = 2(x \cos(\theta) + y \sin(\theta)) / (n - 1)$ and $y_1 = 2(-x \cos(\theta) + y \sin(\theta)) / (n - 1)$, 'n' stands the kernel size, finally, the obtained image after the application of the filter as mentioned,

$$M(x, y) = I(x, y) * f(x, y; \alpha, \theta, \gamma, \delta) \quad (2)$$

3.3. OTSU Thresholding Based Image Segmentation

In this section, the image samples are converted into binary image, in which the pixels are given as 0 and 1, represents two discrete states of images. Specifically, '1' represents the data in white color, whereas, '0' denotes the black color of images. For effective evaluation of cancer nodules in the image, the digital image is divided into several segments for exact identification. Here, segmentation is performed with OTSU thresholding model. Moreover, discrete states are considered here as the threshold rates, and, the pixel that are not in the range of the threshold states are removed. The binary image conversion provides number of benefits such as minimal storage usage, fast velocity dispensation and easier processing, since it requires only two states to be considered for computations. This kind of segmentation also helps in exact detection of Region of Interest (ROI) and that are to be given for tumor diagnosis process. After segmentation, Region Growing process is established and explained in the following section.

3.4. Region Growing

This is the process of combining pixels into some larger regions based on certain rules. For growing regions, 'seed' points are to be selected that are having similar properties for grouping. A set of points are considered as input in sample, objects are noted for segmentation. Area develops via considering the neighbour points of the defined region in iterative manner. Moreover, the pixel similarity is measured based on the pixel strength as well as mean determination of region. Neighbouring pixels that are having minimal difference are combined to frame the region, which are further to be given for feature extraction.

3.5. Feature Extortion

Feature extortion is the procedure that derives quantitative data from the segmented region like texture, shapes, color, and contrast. At this time, two kinds of feature extractions are performed through Discrete Wavelet Transform (DWT) as well as GLCM.

3.5.1. Wavelet Coefficient Extraction

This section defines the wavelet coefficient extraction process from MRI brain images using Discrete Wavelet Transforms. The wavelet points the frequency data of signal function that is significant for result evaluations. Moreover, the two dimensional wavelet transform is employed that produces four bands based on the two state of wavelet separation of ROI, such as,

- Low-Low
- Low-High
- High-Low
- High-High

First two states are used to denote the images with low frequency and the other two states are used to represent the higher frequency rate of images, respectively. Here, images with low states are used with (Low-Low) state of given sample and the image is further divided into second state. For better analysis of features of tumor cells, the samples are separated as spatial data that are obtained by minor sub-bands, further, the advanced frequency components are compared with the previous bands. The

variant frequency elements and each element was analyzed with scalar matching and it is mathematically given as,

$$\begin{aligned} \text{DWT}_T f(I) &= \{d_{x,y} = \sum f(I)H * i(I - 2xy)d_{x,y} \\ &= \sum f(I)L * i(I - 2xy) \end{aligned} \quad (3)$$

Where, the wavelet coefficients ‘ $d_{x,y}$ ’ denotes the element factor in image function $f(I)$, ‘ H ’ and ‘ L ’ denotes the high and low states of image frequencies, respectively. And, x and y are the wavelet scalar factors.

3.5.2. GLCM Based Feature Extraction

For enhancing the accuracy rate of classification results, the feature extraction is carried out using Gray-Level Co-occurrence Matrix. Based on the spatial information and relations between pixels, the statistical features of images are derived in this section. Moreover, it is determined with two dimensional histogram that has (x, y) element is the frequency of incidence of ‘ x ’ amid ‘ y .’

Here, the gray scales are termed as x and y , with distance function $D=1$ and computes the regularity of incidence with pixel strength x that occurs regarding y . Further, the textural features such as correlation, image contrast, energy, entropy and homogeneity are determined depending on lower as well as higher sub bands of wavelet computations. Calculations for textural feature determinations are presented below:

(i) Image Contrast (IC):

The difference between the pixel intensities of particular image is given as,

$$\text{IC} = \sum_{p=0}^{m-1} \sum_{q=0}^{n-1} (p-q)^2 f(p, q) \quad (4)$$

Where, p and q defines the pixel intensities of the given MRI image.

(ii) Correlation:

Correlation (CRR) can be defined as the measurement of dependencies between the spatial data of pixels in the image, which is mathematically presented as,

$$\text{CRR} = \frac{\sum_{p=0}^{m-1} \sum_{q=0}^{n-1} (p, q) f(p, q) - M_p M_q}{\sigma_p \sigma_q} \quad (5)$$

Where, σ_p and σ_q are the variances of p and q .

(iii) Energy (EY):

Determination of affinity in any image is given as Energy computations, which can be further defined as the measurable amount of recurring pixel pairs. The computation is presented as,

$$\text{EY} = \sqrt{\sum_{p=0}^{m-1} \sum_{q=0}^{n-1} f^2(p, q)} \quad (6)$$

(v) Entropy (EPY):

The designated intrusion of textural image is calculated as the entropy of the image, which is expressed as,

$$\text{EPY} = \sum_{p=0}^{m-1} \sum_{q=0}^{n-1} f(p, q) \log_2 f(p, q) \quad (7)$$

(v) Homogeneity (HY):

Local uniformity of MRI sample is termed as homogeneity computation that can differentiate textural and non-textural image properties.

$$\text{HY} = \sum_{p=0}^{m-1} \sum_{q=0}^{n-1} \frac{1}{1 + (p-q)^2} f(p, q) \quad (8)$$

The extorted features are finally provided to the Boosting SVM for classifications of MRI inputs under benign and malignant categories.

3.6. BSVM Based Classification

The soft computing technique incorporated here for classification is Boosting Support Vector Machine based classifications, denotes the operations of SVM is infused with the boosting mechanism for accurate classification of MRI images. Moreover, the signification features are extracted with the DWT and DLGM in the previous section, which are utilized for classification performance. The BSVM mechanism performs effectively when handling with large data and high dimensional medical data. Primary benefit of using BSVM classification method is that model decreases the computational complexities and processing time in efficient manner. The hypothesis of the incorporated classification technique is expressed based on the boosting technique, as hyperplane in feature space. Here, the coefficients are selected in such as manner to reduce the error rate on training data.

3.6.1. Size and Stage Description of Tumors for Classification

After processing the images with BSVM, the samples are evaluated for tumor size and cancer stages based on the following descriptions.

- Stage 0: the size of tumor is detected as very small and it can be named as Edema and categorized under Stage 0.
- Stage 1: when the diagnosed tumor size is ≤ 0.5 mm, then it is categorized under benign stage
- Stage 2: when the detected tumor size is ranges between (1 and 4 mm), it can be classified under stage 2 and denoted as Necrosis. This kind of tumour contains several abnormal cells.
- Stage 3: the size of tumor is ranges between 5 to 10 mm, then it comes under Stage 3 and may contains several dead and dividing tissues. And, that can be termed as Anaplastic Astrocytoma or Ependyoma clinically.
- Stage 4: When the tumor size ≥ 10 mm, then it is considered as the stage 4 and stated as Glioblastoma. This stage of tumors is to be critically treated.

4. RESULTS AND DISCUSSION

For evaluations, the input MRI brain samples are obtained from the DICOM [26] and BraTS [27]. BraTS 2020 employs pre-operative MRI scans from many institutions and concentrates on segmenting (Task 1) fundamentally diverse (in look, form, and histology) brain cancers, such as gliomas. In this work 80 MR brain images were utilized for evaluation. 80% of the images are used for training, while 20% are used for testing. MATLAB simulation is used to evaluate the suggested model. Also shown in Figures 3 and 4 are example images taken from aforementioned databases.

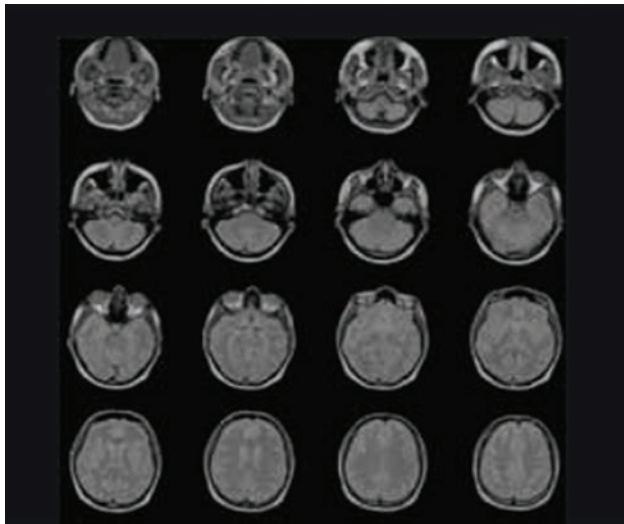


Fig. 3. Sample images from DICOM dataset.

From DICOM dataset, 18 images are taken for processing with the proposed Tumor Categorization Model. Among, 9 images are provided for training and left over samples are given for testing. From another benchmark database BraTS, 150 images are considered from processing, amongst, 75 have tumor images with benign state and the rest in malignant state.

The measures, such as the Peak Signal to Noise Ratio (PSNR) and Mean Square Error (MSE), are used to assess the effectiveness of the suggested model. The equations are expressed as follows,

$$MSE = \frac{1}{XY} \sum_{i=1}^X \sum_{j=1}^Y (a(i,j) - b(i,j))^2 \tag{9}$$

$$PSNR = 10 \log_{10} \frac{(2^m - 1)^2}{\sqrt{MSE}} \tag{10}$$

Where, $a(i,j)$ is actual sample, $b(i,j)$ -the modified sample, (i,j) is pixel position for $X * Y$. Further, Accuracy, Precision and Recall rates are calculated by the following expressions,

$$Accuracy = \frac{(True\ Positive + True\ Negative)}{(True\ Positive + True\ Negative + False\ Positive + False\ Negative)} \tag{11}$$

$$Precision = \frac{True\ Positive}{True\ Positive + False\ Positive} \tag{12}$$

$$Recall = \frac{True\ Positive}{True\ Positive + False\ Negative} \tag{13}$$

For pre-processing, modified Gabor filter is used, which reduces the additional noise in source MRI brain image. Subsequent to the application of MGF, enhanced image is presented in Figure 5 with respect to source MRI brain image with benign cancer and Figure 6 presents the results of MGF for malignant tumor, respectively.

Further, the filter image is given for OTSU based thresholding for segmentation. The obtained result over the malignant tumor image is portrayed in Figure 7. And region growing is determined for appropriate tumor tissue definition with precise borders. Following, the significant attributes are extorted from image for appropriate classifications. Depending on those attributes the classification model is trained and tested for evaluations. The finally segmented brain tumor image is given in Figure 8, which has to be provided for measuring the size and shape of the tumor for classification.

An image from BraTS dataset is processed with the Tumor Categorization Model with the operations in that for categorizing tumor stages. The results are presented in Figure 9, which acquires the input from benchmark brain tumor dataset and given for pre-processing, segmentation and region growing. The segmented image is further utilized for feature extraction with DWT

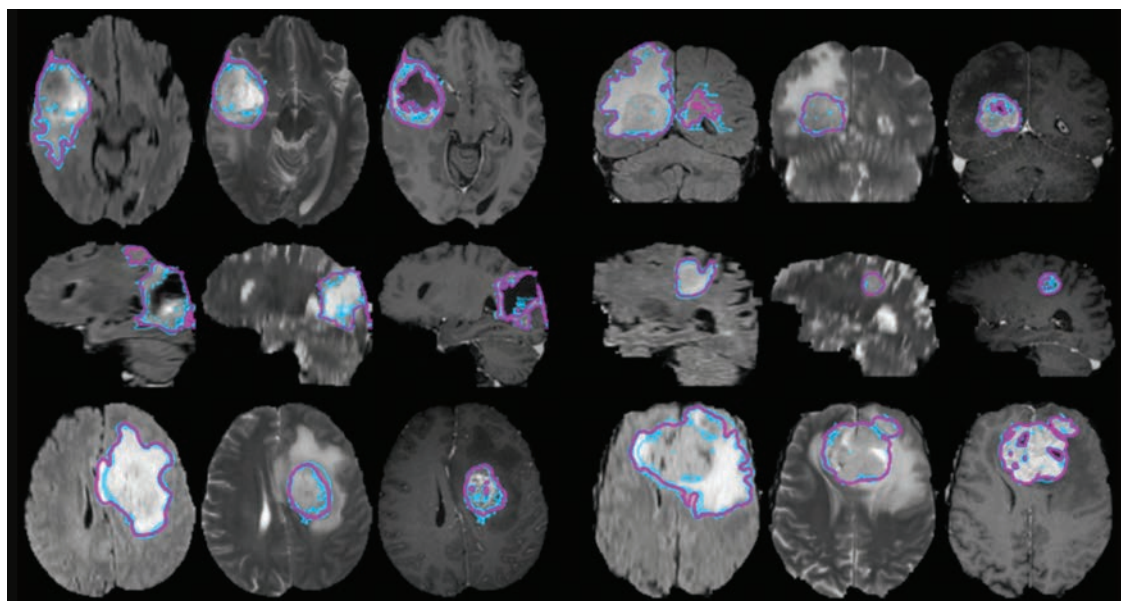


Fig. 4. MRI brain samples from BraTS dataset.

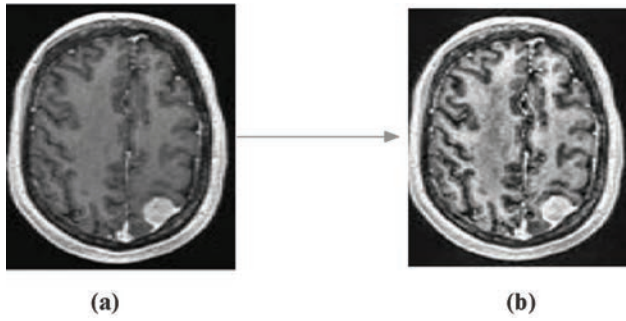


Fig. 5. (a) Original input (b) after the application of MGF.

and GLCM. Then, BSVM based classification is carried out for separating images under benign and malignant classes. When TCM comes into act, the size and shape of the segmented tumor image is measured. Specifically, in the given example, the size of the segmented image is measured as 5.6 mm. Based on that, the brain tumor comes under the categorization of Stage 3. Following, the appropriate treatment suggestions are provided to the medical practitioners for providing better treatments.

The suggested model’s performance will be assessed in order to demonstrate its efficacy. The specificity, sensitivity, accuracy, precision, as well as recall of the findings are used to evaluate them. Additionally, comparative evaluations are made with the existing models such as SVM [9] and ANN [23]. The evaluated results based on the performance factors are portrayed in the Figure 10. The suggested framework produces a higher level of precision and accuracy than the comparative works, according to the research.

The Figure 11 displays the results of accuracy rates with respect to the compared works. Because of the effective utilization of image processing and soft computing techniques, higher

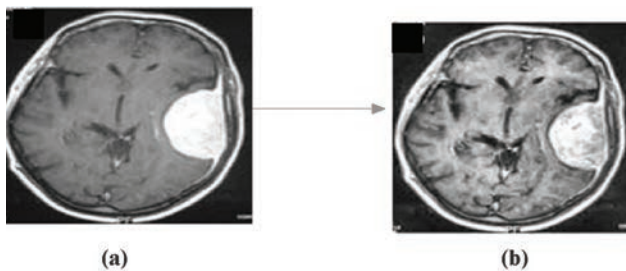


Fig. 6. (a) Original malignant tumor sample (b) filtered image.

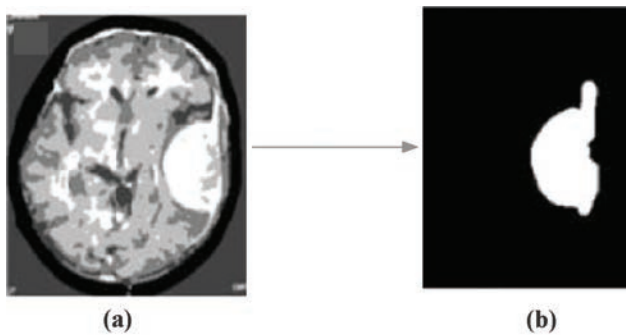


Fig. 7. (a) Malignant tumor image (b) image after segmentation.



Fig. 8. Segmented brain tumor cells after region growing.

rate accuracy in tumor image classification and categorization is achieved in the proposed model. The proposed TCM attains 96.8% of accuracy in average with the effective accumulation of image enhancement and segmentation process.

While designing a tumor classification model, the processing time is to be significantly evaluated. Here, the BSVM classification model is used, in which the model reduced the computational complexities and processing time for training and testing

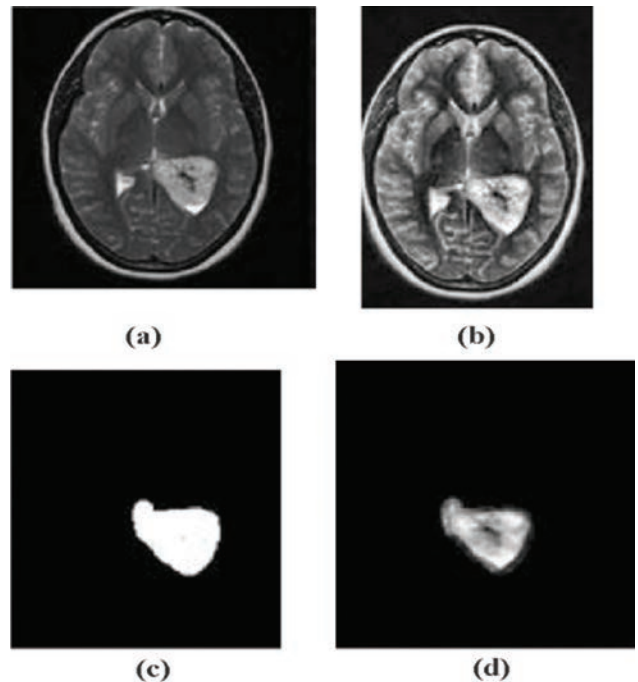


Fig. 9. Processing with BraTS brain image sample (a) source raw image (b) filtered image (c) segmented image (d) refined image.

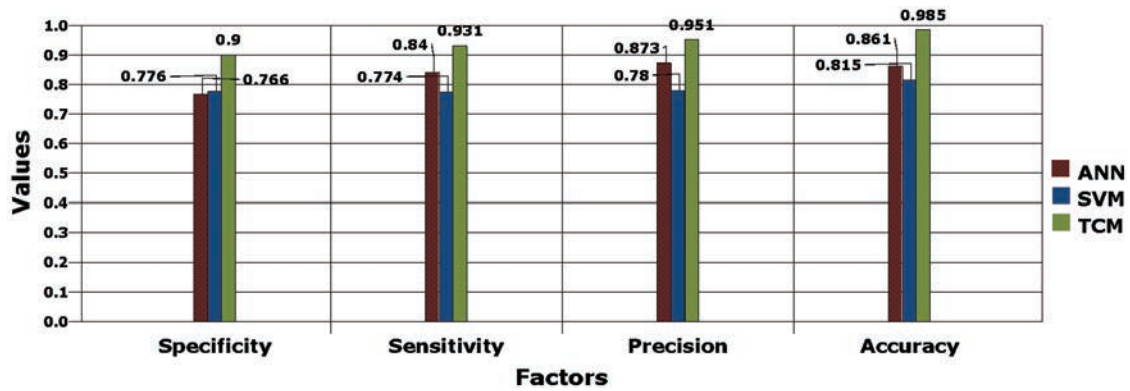


Fig. 10. Performance comparison based comparative evaluations.

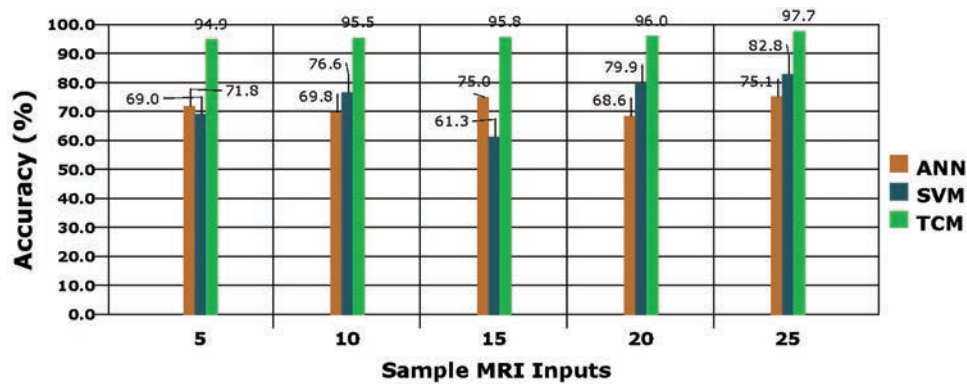


Fig. 11. Accuracy rate comparisons between models.

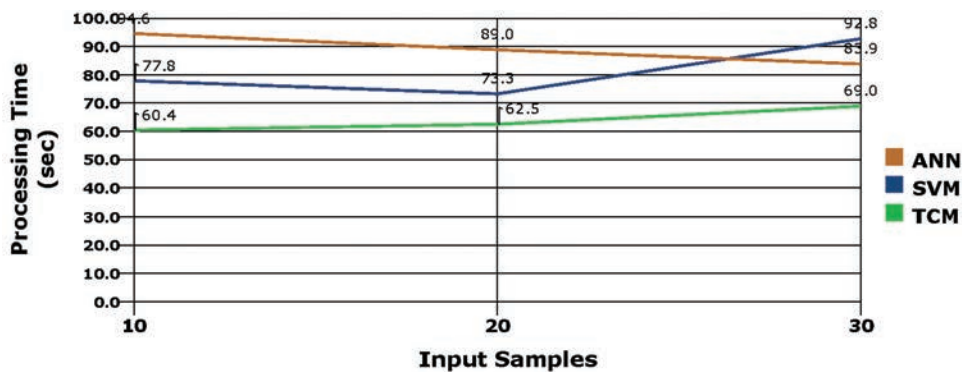


Fig. 12. Analysis with processing time.

brain samples in an effective manner. The evaluation results are plotted against the input samples, where the model takes more time when the number of samples to be processed is becoming higher. Comparably, the proposed model acquires minimal processing time than compared works as displayed in the Figure 12.

Here performance analyses of the proposed and existing methodologies are given based on processing time parameter. This investigation shows that the suggested TCM technique requires less processing time for brain cancer identification, whereas SVM and ANN require greater processing time.

5. CONCLUSION AND FUTURE WORK

In addition to the appropriate Brian Tumor Diagnosis and Classifications, the category of tumor or appropriate tumor state are also known to the medical practitioner for providing better services to save people lives. For that, a Tumor Categorization Model (TCM) with the effective incorporation of image processing and soft computing techniques is developed and evaluated in this paper. The model utilizes the Modified Gabor filter for removing additional noise. OTSU thresholding and region growing methods are used for exact segmentation of tumor tissue with appropriate marginal definitions. Further, feature extraction is carried out with two techniques called DET and GLCM

for deriving significant features for tumor image classification, which is processed with the BSVM based model. Additionally, the classified images are further given for measuring its size and shapes, to identify about the stages of tumor. Further, the model is evaluated using the images from two different benchmark datasets called DICOM and BraTS datasets and acquired solutions are contrasted with the present classification models. Based on comparisons, proposed TCM provides better rate of accuracy with lower processing time. The proposed TCM attains 96.8% of accuracy in average with the effective accumulation of image enhancement and segmentation process. In future, the work can be developed further by developing models for processing hyperspectral images with soft computing methodologies for forwarding the image processing research to the next levels in disease diagnosis.

DECLARATIONS

Ethical Complaints

Necessary ethical standards were maintained in this research study. All procedures were carried out in line with applicable laws and regulations.

Funding Statement

For such a research, the author(s) did not receive any specific funding.

Conflicts of Interest

The researchers assured that they also have no competing interests to declare in this work.

Acknowledgments: We thank the anonymous referees for their useful suggestions.

References and Notes

- Borole, V.Y., Nimbhore, S.S. and Kawthekar, D.S.S., 2015. Image processing techniques for brain tumor detection: A review. *International Journal of Emerging Trends & Technology in Computer Science (IJETTCS)*, 4(5), pp.28–32.
- Landini, L., Positano, V. and Santarelli, M., 2018. *Advanced Image Processing in Magnetic Resonance Imaging*. Boca Raton, CRC Press, pp.1–632.
- Arber, A., Faithfull, S., Plaskota, M., Lucas, C. and De Vries, K., 2010. A study of patients with a primary malignant brain tumour and their carers: Symptoms and access to services. *International Journal of Palliative Nursing*, 16(1), pp.24–30.
- Coatrieux, G., Huang, H., Shu, H., Luo, L. and Roux, C., 2013. A watermarking-based medical image integrity control system and an image moment signature for tampering characterization. *IEEE Journal of Biomedical and Health Informatics*, 17(6), pp.1057–1067.
- Li, W., Chen, C., Su, H. and Du, Q., 2015. Local binary patterns and extreme learning machine for hyperspectral imagery classification. *IEEE Transactions on Geoscience and Remote Sensing*, 53(7), pp.3681–3693.
- Dhanaseely, A.J., Himavathi, S. and Srinivasan, E., 2012. Performance Comparison of Cascade and Feed Forward Neural Network for Face Recognition System. *International Conference on Software Engineering and Mobile Application Modelling and Development*, pp.1–6.
- Singh, A., 2015. Detection of Brain Tumor in MRI Images, Using Combination of Fuzzy c-Means and SVM. *IEEE International Conference on Signal Processing and Integrated Networks (SPIN)*, pp.98–102.
- Amasyali, M.F. and Ersoy, O.K., 2011. Comparison of Single and Ensemble Classifiers in Terms of Accuracy and Execution Time. *International Symposium on Innovations in Intelligent Systems and Applications*, IEEE. pp.470–474.
- Natteshan, N.V.S. and Jothi, J.A.A., 2015. Automatic classification of brain MRI images using SVM and neural network classifiers. in *Advances in Intelligent Informatics, Advances in Intelligent Systems and Computing*, Springer International Publishing Switzerland. Vol. 320, pp.19–30.
- Dandil, E., Çakıroğlu, M. and Ekşi, Z., 2014. Computer-Aided Diagnosis of Malign and Benign Brain Tumors on MR Images. *International Conference on ICT Innovations*, pp.157–166.
- Yazdani, S., Yusof, R., Karimian, A., Riazi, A.H. and Bennamoun, M., 2015. A unified framework for brain segmentation in MR images. *Computational and Mathematical Methods in Medicine*, 2015(829893), pp.1–18.
- El-Dahshan, E.S.A., Mohsen, H.M., Revett, K. and Salem, A.B.M., 2014. Computer-aided diagnosis of human brain tumor through MRI: A survey and a new algorithm. *Expert Systems with Applications*, 41(11), pp.5526–5545.
- Hemanth, D.J. and Anitha, J., 2012. Image Pre-Processing and Feature Extraction Techniques for Magnetic Resonance Brain Image Analysis. *International Conference on Future Generation Communication and Networking*, pp.349–356.
- Nabizadeh, N. and Kubat, M., 2015. Brain tumors detection and segmentation in MR images: Gabor wavelet vs. statistical features. *Computers & Electrical Engineering*, 45, pp.286–301.
- Shanthakumar, P. and Ganesh Kumar, P., 2015. Computer aided brain tumor detection system using watershed segmentation techniques. *International Journal of Imaging Systems and Technology*, 25(4), pp.297–301.
- Kharat, K.D., Kulkarni, P.P. and Nagori, M.B., 2012. Brain tumor classification using neural network based methods. *International Journal of Computer Science and Informatics*, 1(4), pp.2231–5292.
- Joseph, R.P., Singh, C.S. and Manikandan, M., 2014. Brain tumor MRI image segmentation and detection in image processing. *International Journal of Research in Engineering and Technology*, 3(1), pp.1–5.
- Alfonse, M. and Salem, A.B.M., 2016. An automatic classification of brain tumors through MRI using support vector machine. *Egyptian Computer Science Journal*, 40(3), pp.11–21.
- Coatrieux, G., Huang, H., Shu, H., Luo, L. and Roux, C., 2013. A watermarking-based medical image integrity control system and an image moment signature for tampering characterization. *IEEE Journal of Biomedical and Health Informatics*, 17(6), pp.1057–1067.
- Zanaty, E.A., 2012. Determination of gray matter (GM) and white matter (WM) volume in brain magnetic resonance images (MRI). *International Journal of Computer Applications*, 45(3), pp.16–22.
- Yao, J., Chen, J. and Chow, C., 2009. Breast tumor analysis in dynamic contrast enhanced MRI using texture features and wavelet transform. *IEEE Journal of Selected Topics in Signal Processing*, 3(1), pp.94–100.
- Kumar, P. and Vijayakumar, B., 2015. Brain tumour Mr image segmentation and classification using by PCA and RBF kernel based support vector machine. *Middle-East Journal of Scientific Research*, 23(9), pp.2106–2116.
- Sharma, N., Ray, A.K., Sharma, S., Shukla, K.K., Pradhan, S. and Aggarwal, L.M., 2008. Segmentation and classification of medical images using texture-primitive features: Application of BAM-type artificial neural network. *Journal of Medical Physics/Association of Medical Physicists of India*, 33(3), pp.119–126.
- Cui, W., Wang, Y., Fan, Y., Feng, Y. and Lei, T., 2013. Localized FCM clustering with spatial information for medical image segmentation and bias field estimation. *International Journal of Biomedical Imaging*, 2013(13), pp.1–9.
- Chaddad, A., 2015. Automated feature extraction in brain tumor by magnetic resonance imaging using Gaussian mixture models. *International Journal of Biomedical Imaging*, 2015(8), pp.1–12.
- Sachdeva, J., Kumar, V., Gupta, I., Khandelwal, N. and Ahuja, C.K., 2013. Segmentation, feature extraction and multiclass brain tumor classification. *Journal of Digital Imaging*, 26(6), pp.1141–1150.
- Menze, B.H., Jakab, A., Bauer, S., Kalpathy-Cramer, J., Farahani, K., Kirby, J. and Van Leemput, K., 2014. The multimodal brain tumor image segmentation benchmark (BRATS). *IEEE Transactions on Medical Imaging*, 34(10), pp.1993–2024.
- Yuvaraj, N. and Vivekanandan, P., 2013. An Efficient SVM Based Tumor Classification with Symmetry non-Negative Matrix Factorization Using Gene Expression Data. *International Conference on Information Communication and Embedded Systems (Icices)*, pp.761–768.

Received: 14 June 2021. Accepted: 21 July 2021.

Effect of thickness on the physical properties and gas sensing application: anatase titanium dioxide nanofilms by automated nebulizer spray pyrolysis (ANSP)

V. Gopala Krishnan^{1,2} · A. Purushothaman² · P. Elango¹

Received: 20 February 2017 / Accepted: 10 April 2017
© Springer Science+Business Media New York 2017

Abstract In this work, effects of thickness towards volume proportion of TiO₂ nanofilms were deposited on a glass substrate at 500 °C by using ANSP method. The optical profilometer shows the coated films thicknesses were increased (186, 234, 311, 397 and 433 nm) by increasing the volume proportion. Based on the thickness, The XRD reveals a polycrystalline tetragonal anatase phase with decreased particle sizes. The topographical study (AFM) of 3D surface view shows the incremented average roughness (R_a) values. The surface morphological variations with decremented particle size were examined by FESEM. The maximum transmittance ~78.5% ($\lambda = 612.8$ nm) is obtained to 186 nm thickness and further increment of thickness shows the decremented value of transmittance with an absorption edge shifted from lower to higher wavelength (blue shift) and the calculated band gap value $E_g = 3.65$ – 3.26 eV. The gas sensing performances of films was studied by using a various sensing parameters, obviously C₂H₆O gas shows highest response ($S_m = 13\%$ as 397 nm) at 300 °C for 150 ppm gas concentration against other gasses (NH₃, CH₄O, C₃H₈O and C₃H₆O).

1 Introduction

The improvement of nanoscience and nanotechnology plays an effective role to reduce several global environmental

problems such as the greenhouse effect and the ozone hole. These problems are related to the release of pollutant gasses in the atmosphere, therefore their exposure and demolitions are the hot global priority. As mentioned in the literature, the semiconducting metal oxide of solid-state (SnO₂, TiO₂, ZnO) gas sensors is widely preferred due to a sequence of specific advantages [1]. Particularly, *n*-type metal oxide semiconductor of titanium dioxide (TiO₂) is an effective material for the different new applications such as solar cell [2], purifier of environmental pollutants [3], photocatalysis [4], gas sensors [5], corrosion-protection [6] and microelectronics [7, 8] applications, due to its properties of non-toxicity in aqua, reasonable cost, powerful oxidation potential and high chemical inertness TiO₂ is an attractive material owing to their notable ability to change the electrical resistance (conductance) in response to oxidizing and reducing gasses, and the electronic structure of TiO₂ and its consequences as far as the gas sensing performance is concerned immensely.

TiO₂ defined with three polymorphic forms such as anatase, brookite, and rutile. The Rutile (D_{4h} , ¹⁴P4₂/mm, symmetry) and anatase (D_{4h} , ¹⁹I4₁/amd, symmetry) make a tetragonal phase and they were developed commercially, but the orthorhombic phase of brookite (Pcab, lower symmetry) is very difficult to prepare but naturally present in a solitary crystal form. Brookite and anatase may be turned to rutile phase by the subject of higher temperature, usually at ~750 to ~1000 °C respectively [9]. A rutile phase is usually the dominant phase in TiO₂, but some work has been synthesizing an anatase phase because of their importance in practical engineering applications in sensors [10]. The fabrication of the anatase and rutile phases strongly depends on the temperature and deposition method [11]. Attentively many techniques are used to prepare the stabilized anatase TiO₂ thin films namely, sol–gel [12], chemical

✉ P. Elango
yuvagopal@yahoo.in

¹ Department of Physics, Government Arts College, Coimbatore 641018, India

² Department of Physics, Sree Sakthi Engineering College, Coimbatore 641104, India

vapor deposition [13], pulsed laser deposition [14], electrochemical [15], RF-magnetron sputtering and spray pyrolysis deposition [16]. Among them, the spray pyrolysis is one of the significant methods which may effectively open new routes to nanotechnology. This process importantly has a very safety, less expensive, no need in vacuum arrangement and sustaining homogeneity in large area of film coating [17] behaviors.

Significantly, the effect of thickness plays an important role in controlling the phase stability and film properties, which is one of the critical parameters to achieve a desired structural and functional property [18]. As our knowledge, only a few works have been studied by using acetylacetonone stabilized Ti-alkoxide precursors, whereas the phase stability was not maintained on their works also [19–21]. Particularly no systematic study of structural and optical characterization of the anatase phase TiO₂ films deposited by spray pyrolysis technique from the source of acetylacetonone stabilized Ti-isopropoxide have been performed. Predominantly, the automated nebulizer sprayed anatase phase stabilized and gas sensing performances of TiO₂ film have not been studied so far. The aim of this work is to deposit TiO₂ nanofilms on preheated glass substrate at 500 °C with different volume proportions by the method of automated nebulizer spray pyrolysis and exemplify the effect thickness on structural, optical, topography, morphological and gas sensing performance of TiO₂ nanofilms.

2 Experimental details

TiO₂ nanofilms array with nominal volume proportions (x) of 2.5, 5.0, 7.5, 10.0 and 12.5 ml is taken and prepared by using automated nebulizer spray pyrolysis technique (ANSP) in an air atmosphere. The experimental setup, procedure and advantages of ANSP were explained [9] elsewhere and the observed basic parameters were mentioned in Table 1. The primary stock solution was prepared with 0.1 M/l of titanium tetra-isopropoxide (TTIP) [Ti[OCH(CH₃)₂]₄] dissolved in 50 ml mixed solution of ethanol (EtOH) (C₂H₅OH) solvent with acetylacetonone (AcAc) [CH₃COCH₂COCH₃] stabilizer in the ratio of (4:1) and stirred for 15 min by using magnetic stirrer. The obtained transparent pale yellow solution with different above mentioned volume proportions was sprayed on the ultrasonically cleaned glass substrate at 500 °C.

Various volume proportions of coated films may bring into being a various thickness of the films and their characterization is analyzed by the following study. The structural properties of TiO₂ films were entirely studied by X-ray diffraction (Bruker D8 advance X-ray diffractometer) with Cu K α radiation ($\lambda=0.15418$ nm). Surface morphology of the films was characterized via atomic force microscope

Table 1 Optimized spray parameter for TiO₂ nanofilms with thickness variation

Particulars	Parameter
Spray type	Nebulizer
Air blast	Atomizer
Carrier gas pressure	30 Pa
Solution flow rate	0.10 ml/min
Distance from substrate to spray nozzle	5 cm
Substrate type	Glass
Solvent	Ethanol and acetyl acetone
Precursor	Titanium isopropoxide
Concentration	0.1 mol/l
Deposition variation	2.50, 5.00, 7.50, 10.00, 12.50 ml
Deposition temperature	500 °C

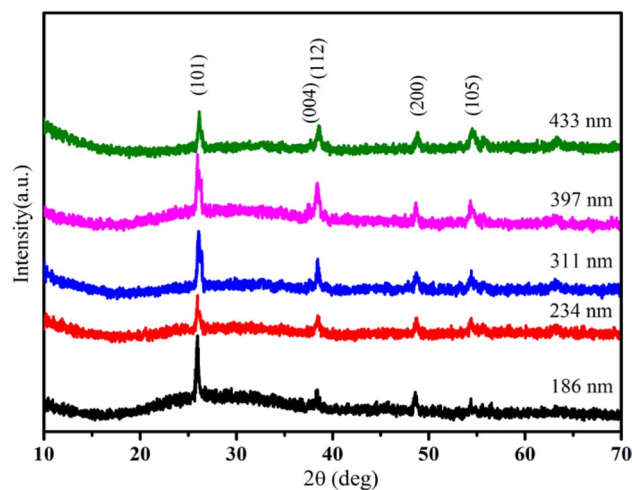


Fig. 1 XRD study on various thickness of TiO₂ nanofilms

(AFM, Model-Nanoscope E) and field emission scanning electron microscopy (FESEM, Quanta-250 FEG) applying an operating voltage 30.0 kV. An optical study of the films was done by Ultra Violet–Visible–Near Infrared (UV–Vis–NIR) spectrophotometer (Model JASCO-V-500) in the range from 250 to 980 nm and thickness of the films was determined by using surface profilometer (SJ-301 Mitutoyo). Finally, the gas sensing performances were studied by LCR meter (GW Instek LCR-821).

3 Results and discussion

XRD study of thickness varied (186, 234, 311, 397, 433 nm) nanofilms of TiO₂ are shown in Fig. 1. The coated films were generally polycrystalline with stabilized anatase form of tetragonal phase with prominent diffraction peaks

at $2\theta = 25.51, 38.31, 48.66$ and 55.44° corresponding to (101), (112), (200) and (105) reflection planes were well fitted with standard JCPDS data, card no. 89-4921. Mean-time, this film was not detected other two remaining phases (brookite, rutile) because the preparation method and raw materials were maintain the phase stability [22]. The crystallite size ‘D’ is calculated using Scherrer formula [23],

$$D = \frac{0.9 \times \lambda}{(\beta \times \cos \theta)} \quad (1)$$

$$d = \frac{n\lambda}{(2 \sin \theta)} \quad (2)$$

where D is the crystalline size, λ is the wavelength of X-rays, β is the broadening of diffraction line measured at half its maximum intensity in radius, d is interplaner spacing value and θ is the angle of diffraction. The average crystallite size and d-spacing value were found to decrease with increase in thickness and their intensity of TiO₂ films varied with respect to thickness. The lattice constants determined from the present data are $a = 3.788$ and $c = 9.549 \text{ \AA}$. The dislocation density and microstrain were calculated by using equations (3) and (4) for TiO₂ films [9].

$$\delta = \frac{1}{D^2} \quad (3)$$

$$\epsilon = \frac{\lambda}{D \sin \theta} - \frac{\beta}{\tan \theta} \quad (4)$$

The variation of dislocation density and microstrain with different thickness of TiO₂ was listed in Table 2. It has been confirmed that the calculated average crystalline size, d-spacing value, lattice parameter, dislocation density and microstrain of the obtained films values corresponded to that of the bulk TiO₂ anatase phase structure [24].

Atomic force microscope (AFM) allows us to get microscopic information on the surface structure and to plot topographies representing the surface relief. This technique offers digital images which allow quantitative measurements of surface features, such as root mean square roughness R_q , or average roughness R_a , and the analysis of images from different perspectives, including three-dimensional simulation. The topography view of $2 \mu\text{m} \times 2 \mu\text{m}$ sized three-dimensional AFM images of TiO₂ nanofilms with different thickness (186, 234, 311, 397, 433 nm) is shown in Fig. 2a–e. In sample with the lowest thickness, particles rather are isolated from each other (Fig. 2a, b) while in Fig. 2c–e are continually in distribution these changes in surface morphology might lead to degradation in the crystalline quality of the film [25]. This suggests that the particles seen at the surface of the film are clusters of crystallites. The AFM analyses of average roughness parameters were listed in Table 2. It can be seen from the figure, the surface roughness and coating thickness of

the films is increased with respect to thickness. This variation shows the fine correspondence with crystalline size and d-spacing value of XRD study. Figure 2f–j shows the surface morphological characterisation of TiO₂ nanofilms and it is analysed by using field emission scanning electron microscope (FESEM). The smaller thickness of the coated films (186 nm) depicts the spherical shape structures and for the thickness of 234, 311, 397, 433 nm shows the micro spherical structures. The observed particle sizes were decreased by increase in thickness, which is in good agreement with structural and topography study.

The optical transmittance spectra of TiO₂ nanofilms over the spectral range of 250 nm to 980 nm are shown in Fig. 3. The oscillating nature of average transmittance is enhanced up to 78.4% (at $\lambda = 616 \text{ nm}$) for the coated film of 186 nm thickness. The transmittance values of all coated films were decreased by increase in thickness. This decrement is caused by the fundamental absorption of light may increase the quality of defect less films immensely [26]. The UV region of sharp absorption edges was shift from shorter to longer wavelength (Blue-shift) due to the thickness (186, 234, 311, 397, 433 nm) variations, since the improvement in crystal quality of the films along with a reduction in porosity [27]. The band gap energy was calculated by using the Tauc’s relation [28].

$$\alpha(h\nu) = A(h\nu - E_g)^{1/2} \quad (5)$$

where E_g is the optical band gap of the sample and A is constant. Optical band gap (E_g) energy of TiO₂ film is carried out by extrapolating linear region spectrum $(\alpha h\nu)^2$ versus $(h\nu)$ as shown in Fig. 4. The obtained band gap energy ($E_g = 3.26\text{--}3.65$) is decreased from higher to lower with respect to increasing thickness because of an improvement in film quality may reduce the structural defect. The standard band gap energy of anatase phase TiO₂ is 3.20 eV is finely coinciding with a coated thickness of 397 nm, hence the film was currently matched with XRD study.

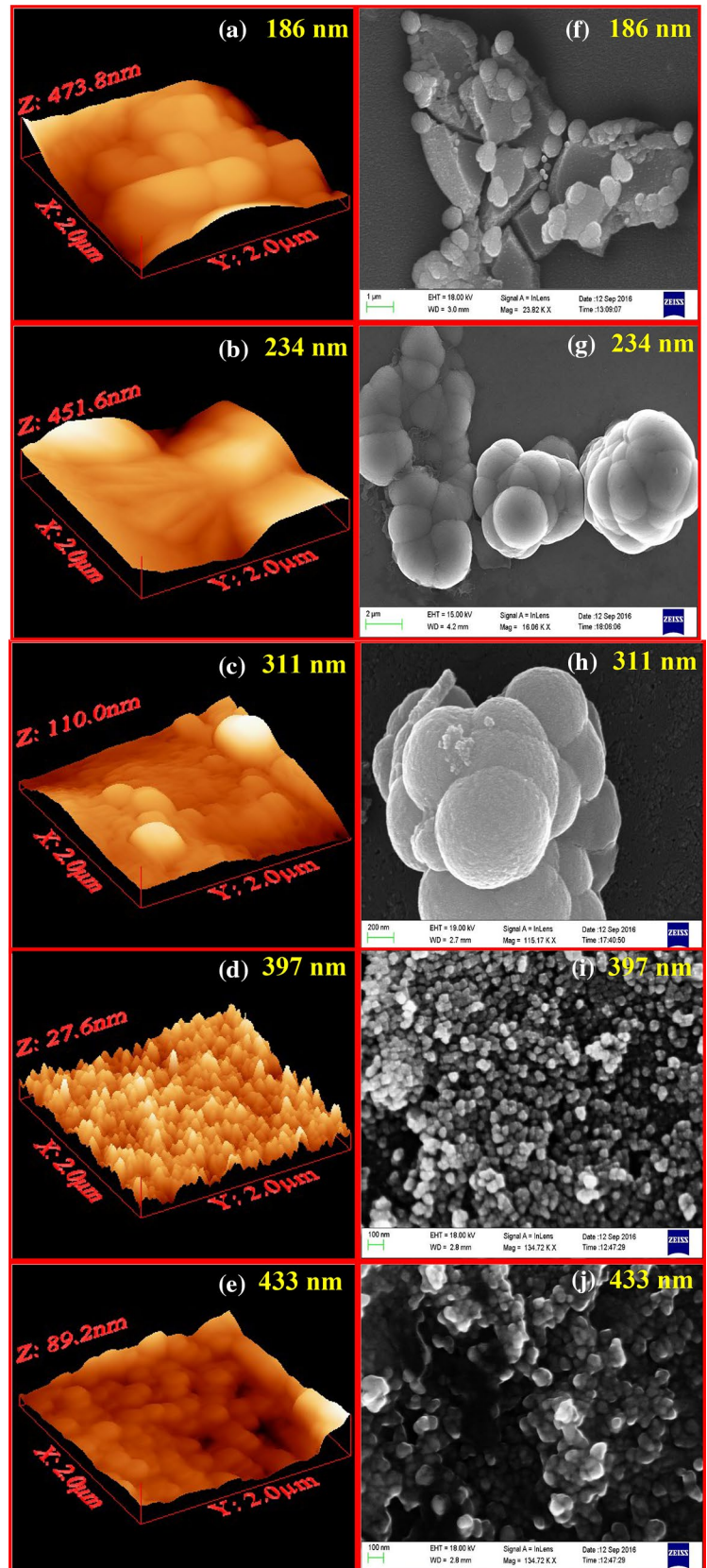
3.1 Gas sensing behavior of TiO₂ nanofilms

The schematic diagram of the gas sensor setup was represented in Fig. 5. As we can be seen, the cylindrical stainless steel testing chamber inbuilt with a nichrome-heating element and a chromel–alumel thermocouple is fixed at bottom of the testing chamber and it is well connected with a temperature controller for adjusting the temperature (~up to 500 °C). The sensing measurements were proceeded by a static process: a specified amount of the test gas such as C₂H₆O, NH₃, CH₄O, C₃H₈O, and C₃H₆O was injected into a testing chamber and mixed with air. A mass flow controller (MFCs) was used to control the concentration of the test gasses. The sensor films were electrically connected to a

Table 2 Obtained values of structural parameters, average roughness and coating thickness of the TiO₂ films

Volume (ml)	Peak position 2θ (deg)	FWHM value (deg)	(h k l)			"D" partical size (nm)	"g" dislocation ×10 ¹⁴ (linmet ⁻²)	"g" strain ×10 ⁴ (lin ⁻² met ⁻⁴)	"d spacing" value ×10 ⁻¹⁰ m	Stacking fault	Average roughness (nm)	Thickness (nm)
			h	k	l							
2.50	25.930	0.1673	1	0	1	50.94	3.854	7.114	3.436	0.088	1.781	186
	38.313	0.2007	0	0	4	43.80	5.212	8.272	2.349	0.086		
	48.621	0.2676	2	0	0	34.05	8.624	10.641	1.873	0.101		
	54.364	0.8029	1	0	5	11.63	73.973	31.164	1.688	0.283		
	25.832	0.1673	1	0	1	50.93	3.856	7.115	3.449	0.088	2.061	234
5.00	38.454	0.4015	0	0	4	21.90	20.841	16.542	2.341	0.172		
	48.130	0.2676	2	0	0	33.99	8.657	10.661	1.891	0.101		
	54.400	0.4015	1	0	5	23.25	18.492	15.581	1.687	0.142		
	25.703	0.2007	1	0	1	42.44	5.552	8.538	3.466	0.106	2.683	311
	38.459	0.3346	0	0	4	26.28	14.474	13.785	2.341	0.143		
10.00	48.458	0.3346	2	0	0	27.22	13.501	13.314	1.879	0.126		
	54.153	0.5353	1	0	5	17.42	32.943	20.797	1.694	0.189		
	25.387	0.2676	1	0	1	31.81	9.883	11.391	3.508	0.143	2.815	397
	37.872	0.2342	0	0	4	37.49	7.116	9.666	2.376	0.101		
	48.146	0.4725	2	0	0	19.25	26.988	18.824	1.890	0.179		
12.50	53.153	0.4015	1	0	5	23.13	18.697	15.668	1.723	0.144		
	25.197	0.2007	1	0	1	42.40	5.563	8.546	3.534	0.107	3.104	433
	37.912	0.4684	0	0	4	18.75	28.458	19.329	2.373	0.202		
	48.082	0.3346	2	0	0	27.18	13.541	13.333	1.892	0.127		
	53.225	0.6022	1	0	5	15.42	42.035	23.492	1.721	0.215		

Fig. 2 a–j Topography view of AFM and surface morphology of FESEM for TiO₂ thin films



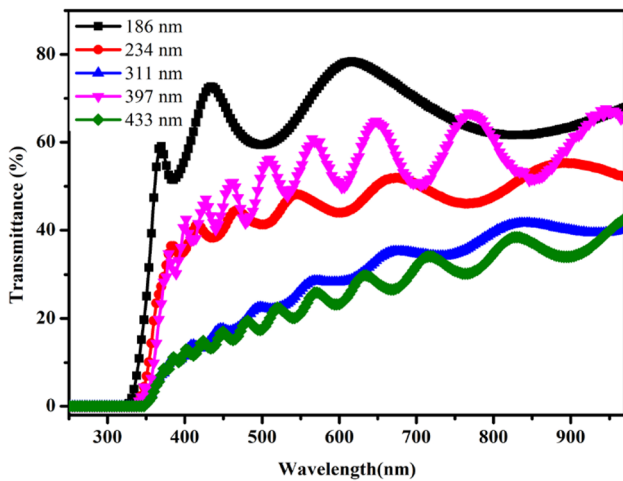


Fig. 3 Variation of transmittance as a function of wavelength for TiO_2 nanofilms

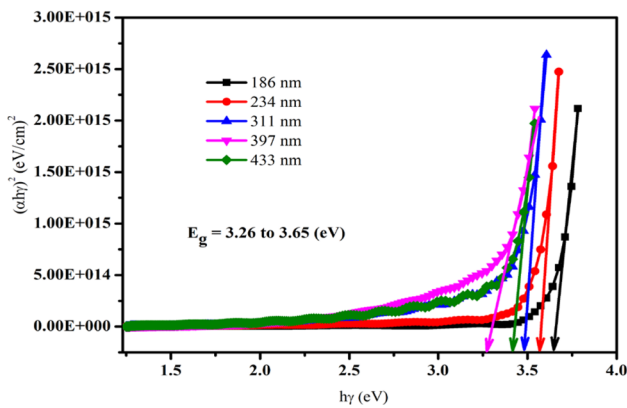


Fig. 4 Plot of $(\alpha h\nu)^2$ versus $h\nu$ for TiO_2 films sprayed at 773 K

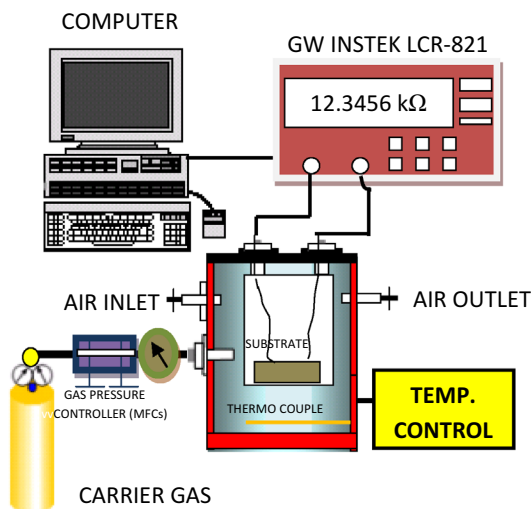


Fig. 5 Schematic diagram of gas sensor setup

two-probe setup for measure the resistance variation (GW Instek LCR-821) and hence calculate the sensing response. The gas sensitivity response (S) factor of TiO_2 nanofilms was calculated by using the relation of resistance in the air (R_{air}) and resistance in reducing gasses (R_{gas}), which was expressed as [29].

$$S = \frac{R_{\text{air}} - R_{\text{gas}}}{R_{\text{gas}}} = \frac{\Delta R}{R_{\text{gas}}} \sim \frac{R_{\text{air}}}{R_{\text{gas}}} \quad (6)$$

Based on that, various parameters such as crystallite size, film thickness, porosity, amount and nature of dopant, catalysts and surface states are known to be important in enhance the gas sensitivity of the sensors element [30]. The main emphasis of this letter is to study the chemiresistors (metal oxide) gas sensing surface phenomenon of adsorbed oxygen and different gases (CH_3OH , NH_3 , $\text{C}_3\text{H}_8\text{O}$, $\text{C}_2\text{H}_6\text{O}$ and $\text{C}_3\text{H}_6\text{O}$) with various parameters of sensitivity, selectivity, response and recovery times with respect to the function of temperature ($^\circ\text{C}$) and gas concentration (ppm) of pure titanium oxide nanofilms were prepared by using automated nebulizer spray pyrolysis method. The sensing nature of pure TiO_2 films significantly relates with operating temperature [31]. Accordingly, the gas sensing response behaviour of various coated thickness (186, 234 nm, 311, 397, 433 nm) of TiO_2 nanofilms were represented with a function of temperature ($50\text{--}350^\circ\text{C}$) at an constant gas concentration (150 ppm) of $\text{C}_2\text{H}_6\text{O}$ reducing gas is shown in Fig. 6(left). As we can be seen, the gas response of all the films increased with respect to operating temperature, the sensor element (TiO_2) of the various coated thickness of the films reaches the maximum gas response ($S_m = 13\%$ as 397 nm) at 300°C and then falls with further increase in operating temperature is due to the mechanism of gas adsorption and desorption of chemiresistors (metal oxide) [1]. Similarly, Fig. 6(right) denote the various reducing gas sensing response of 397 nm thickness of TiO_2 with a function of temperature ($50\text{--}350^\circ\text{C}$) at a constant gas concentration (150 ppm). Among the various reducing gas, the $\text{C}_2\text{H}_6\text{O}$ reducing gas reveals the highest gas response ($S_m = 13\%$) may be due to the surface phenomenon of adsorbed oxygen, nanocrystalline nature of films and higher surface to volume ratio [32].

The dependence of sensitivity towards different thickness of (186, 234, 311, 397, 433 nm) TiO_2 on the $\text{C}_2\text{H}_6\text{O}$ gas concentration at an operating temperature of 300°C is shown in Fig. 7(left). It is observed that the sensitivity increases linearly as the $\text{C}_2\text{H}_6\text{O}$ concentration increases from 30 to 150 ppm and then decreases with further increase in the $\text{C}_2\text{H}_6\text{O}$ gas concentration. The linear relationship between the sensitivity and the $\text{C}_2\text{H}_6\text{O}$ gas concentration at low concentrations may be attributed to the availability of a sufficient number of sensing sites on the

film to act upon the C_2H_6O . The lower and higher gas concentration involves a lower and higher surface coverage of gas molecules, resulting in a lower and higher surface reaction between the surface adsorbed oxygen species and the gas molecules. Further increase in gas concentration the surface reaction will be gradual and reached saturation of the surface coverage of gas molecules. Thus, the maximum sensitivity was obtained at an operating temperature of $300^\circ C$ for the exposure of 150 ppm of C_2H_6O reducing gas.

Fig. 6 Sensitivity response of ethanol gas with the function of temperature for various coated thickness, sensitivity response to 397 nm thickness with an functions of temperature (right)

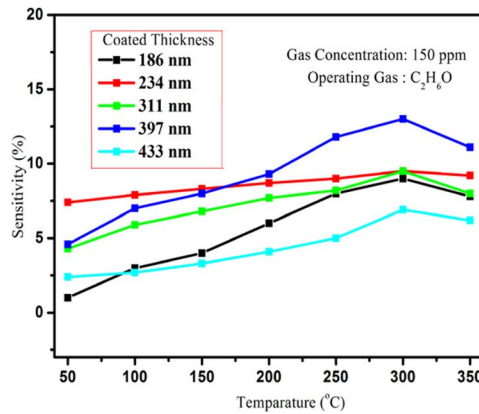


Figure 7(right) shows the various reducing gas response to 397 nm thickness of TiO_2 films at $300^\circ C$ operating temperature for different gas concentration. Which is shows the C_2H_6O gas exposes highest sensitivity response when compared with other reducing gasses.

Figure 8(left) shows the sensitivity response to different thickness (186, 234, 311, 397, 433 nm) of various reducing gasses at $300^\circ C$ operating temperature with constant gas concentration (150 ppm). Among all gasses, the C_2H_6O

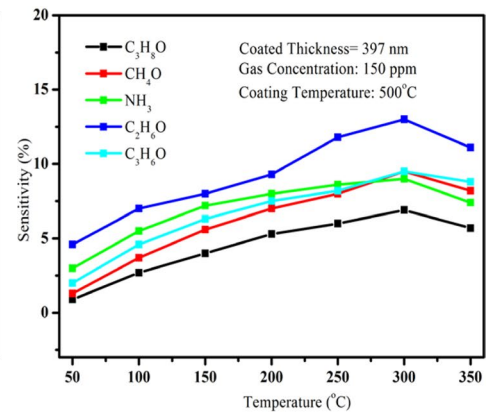


Fig. 7 Sensitivity response of ethanol gas with the function of gas concentration for various coated thickness (left), sensitivity response to 397 nm thickness with an functions of gas concentration (right)

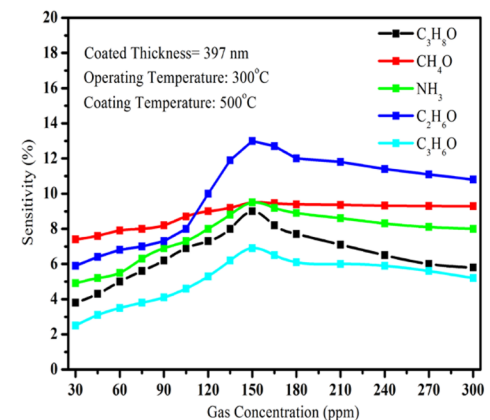
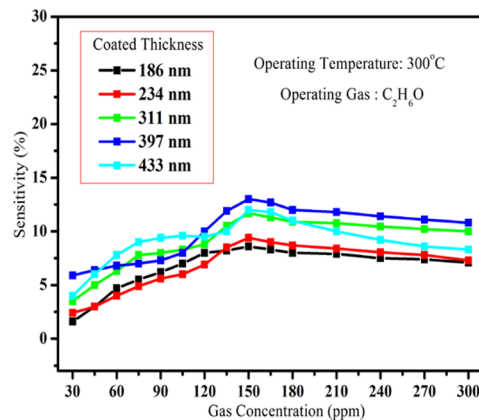
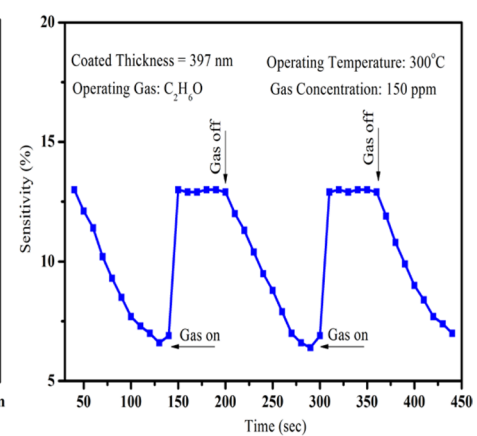
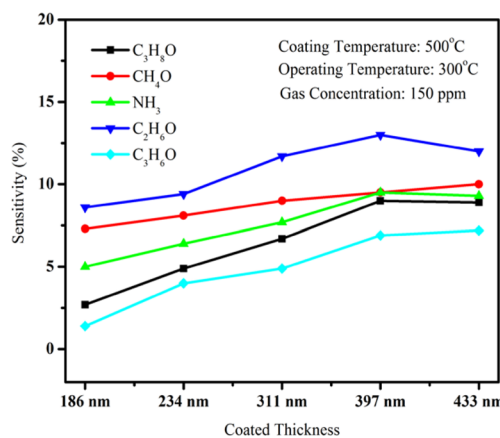


Fig. 8 Sensitivity response of various gases with the function of coated thickness (left side), sensitivity response and recovery time to 397 nm coated film of TiO_2 (right side)



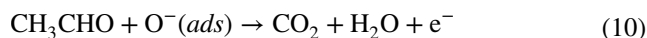
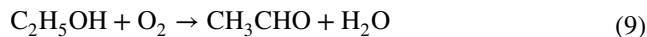
gas reveals the high sensitivity response for the respective parameter. The effective of these sensors is very fast as it can be observed; that the gas response and gas recovery times are defined as the times of conductance takes to reach 90% of $(R_f - R_0)$ when the gas is introduced and to recover 30% of $(R_f - R_0)$ when the flux of the air is restored. Figure 8(right) says the response and recovery time for C_2H_6O are about 20 and 90 s respectively. The quick response C_2H_6O gas may due to faster oxidation, which shows their good sensing ability and their time to the sensitivity response of the sensor element has approximately constant in every cycle, which is indicating the repeatability of the sensor.

3.2 Gas sensing mechanism

The fast response and quick recovery of C_2H_6O reducing gas having a most important feature of the present investigation are high gas response, high selectivity to against other gasses (NH_3 , CH_4O , C_3H_8O , and C_3H_6O). The enhanced response could be attributed to nanocrystalline nature of the films. It is known that the high sensitivity performances were sustained with a metal oxide, which absorbs oxygen species of O^{-2} , O^{-} or O^{2-} from the surrounding and also control the increment of conductivity due to electron capture by oxidizing gas [33] were as,



The presence of chemically adsorbed oxygen could cause electron depletion in the thin film surface and be building up of Schottky surface barrier; consequently, the electrical conduction of thin film decreased to a minimum. When a surface of the material exposed to the reducing gas, the interaction with the chemisorbed oxygen can take place in a various way. Here, the maximum sensitivity of surface reactions can be written to the reducing gas of ethanol as the follows [34]:



with this reaction, many electrons could be released to a thin film surface. This could make the Schottky surface barrier decrease; with the depletion layer thinner; consequently, the electrical conductance of the thin film increases. More gas would be absorbed by the thin film surface; thus, the gas sensitivity was enhanced. An increase in operating temperature causes oxidation of a large number of C_2H_6O molecules, thus producing a very large number of electrons. Therefore, conductivity increases largely. This is the reason why the gas sensitivity increases with operating temperature. However, the sensitivity decreases at

higher operating temperature, as the oxygen adsorbents are desorbed from the surface of the sensor [35]. In addition, at a higher temperature, the carrier concentration increases due to intrinsic thermal excitation and the Debye length decreases. This may be one of the reasons for decreases gas sensitivity at higher temperature [36].

4 Conclusion

Based on the structural, compositional, topography, surface morphology, optical and gas sensing performance of our samples were emerge out the following points: (i) different thickness of the TiO_2 films were examined by using optical profilometer and the obtained thickness are 186, 234, 311, 397, 433 nm with respect to volume proportion (ii) all samples exhibits a polycrystalline anatase phase of tetragonal structure with strong plane orientation (101), and the observed crystalline size were decreased with increase in thickness. (iii) AFM shown the average roughness value were increased by increase the thickness and the morphological behavior of micro spherical structure with reduced particle sizes as revealed in the study of FESEM. (iv). The optical transmittance values were decreased with an blue shift of absorption edge; the band values were decreased with increase in thickness due to the improvement of defect-free quality films was determined by optical measurement. (v). Finally, the gas sensing performance of TiO_2 nanofilms shows their sensitivity response (%) with respect to operating temperature, coated thickness and gas concentration of various gasses. The reducing gas of C_2H_6O exhibits a greatest sensitivity response ($S=13\%$) against other gasses at $300^{\circ}C$ for 150 ppm of gas concentration.

Acknowledgements One of the authors (V. Gopala Krishnan) gratefully acknowledges to Dr. T. Shripathi, Dr. U. P. Deshpande and Er. Mohan Gangrade from the UGC—DAE CSR, Indore Centre, Khandwa Road, India for their scientific advice and for providing the necessary laboratory facilities such XPS and AFM measurements for carry out this investigation.

References

1. D. Mardare, N. Iftimie, D. Luca, J. Non-Cryst. Solids **354**, 4396–4400 (2008)
2. I. Vaiciulis, M. Girtan, et al., Proc. Rom. Acad. Seri. A **13**(4), 335–342 (2012)
3. H. Ichiura, T. Kitaoka, H. Tanaka, Chemosphere **50**(1), 79–83 (2003)
4. M.O. Abou-Helal, W.T. Seeber, Appl. Surf. Sci. **195**, 53 (2002)
5. N.E. Stankova, I.G. Dimitrov, et al., Appl. Surf. Sci. **254**, 1268 (2007)
6. I. Poullos, P. Spathis, et al., J. Environ. Sci. Health. A, **34**(7), 1455–1471 (1999)
7. G.P. Burns, J. Appl. Phys. **65**, 2095 (1989)

8. H.G. Choi, S. Yong, D.K. Kim, Kor. J. Mater. Res. **22**(7), 352–357 (2012)
9. V. Gopala Krishnan, P. Elango, et al., Optik-Int. Light Electron Optics **127**, 11102–11110 (2016)
10. H. Tang, K. Prasad, et al., Sens. Actuators B Chem. **26–27**(1–3), 71–75 (1995)
11. K.L. Choy, B. Su, J. Mater. Sci. Lett. **18**, 943–945 (1999)
12. M. Bockmeyer, B. Herbig, et al., Thin Solid Film **517**, 1596–1600 (2009)
13. N. Rausch, E.P. Burte, J. Electrochem. Soc. **140**(1), 145–149 (1993)
14. J-C Orlianges, et al., J. Appl. Surf. Sci. **263**, 111–114 (2012)
15. M. Bouaicha, N. Ghrairi, Nanoscale Res. Lett. **7**, 357 (2012)
16. A.I. Martinez, et al., J. Phys. **16**(22), S2335–S2344 (2004)
17. R. Mariappan, V. Ponnuswamy, et al., Mater. Sci. Semicond. Process. **16**, 1328–1335 (2013)
18. L. Wei, O. Caiwen, P. Huang, et al., Int. J. Electrochem. Sci. **8**, 8213–8226 (2013)
19. I. Oja, A. Mere, M. Krunks, et al., Thin Solid Film **515**, 674–677 (2006)
20. F.D. Duminica, F. Maury, et al., Thin Solid Film **515**, 7732–7739 (2007)
21. H. Zabova, V. Cirkva, J. Chem. Technol. Biotechnol. **84**, 1624–1630 (2009)
22. W. Niu, G. Wang, et al., Int. J. Electrochem. Sci. **10**, 2613–2620 (2015)
23. B.D. Cullity, *Elements of X-ray Diffraction*, 2nd edn. (Addison-Wesley Publishing Company Inc, Toronto, 1978)
24. S.K. Joung, T. Amemiya, et al., Chem. Eur. J. **12**, 5526–5534 (2006)
25. M.A. Martynez, C. Guillen, J. Herrero, J. Appl. Surf. Sci. **136**, 8 (1998)
26. D. Mardare, M. Tasca, M. Delibas, et al, J. Appl. Surf. Sci. **156**, 200–206 (2000)
27. N.M. Ganesan, T.S. Senthil, et al., Int. J. Chem. Tech. Res. **6**(5), 3078–3082 (2014)
28. K.Y. Rajpure, C.D. Lokhande, et al., Mater. Res. Bull. **34**, 1079–1087 (1999)
29. A.A. Haidrya, J. Puskelova, et al., Appl. Surf. Sci. **259**, 270–275 (2012)
30. C.H. Han, D.W. Hong, et al., Sens Actuators B Chem. **128**, 320–325 (2007)
31. L.A. Patil, D.N. Suryawanshi, et al., Bull. Mater. Sci. **37**(3), 425–432 (2014)
32. C. Garzella, E. Comini, et al., Sens Actuators B Chem. **68**, 189–196 (2000)
33. P. Shailesh, C. Manik, et al., J. Sensor Technol. **1**, 9–16 (2011)
34. M.R. Vaezi, S.K. Sadrnezhad, Mater. Sci. Eng. B **140**, 73–80 (2007)
35. H. Windichamann, P. Mark, J. Electrochem. Soc. **126**(4), 627–633 (1979)
36. J. Mizsei, Sens Actuators B Chem. **23**, 173–176 (1995)

A study of the physical properties and gas-sensing performance of TiO₂ nanofilms: Automated nebulizer spray pyrolysis method (ANSP)

Vijayan Gopala Krishnan^{1,2}, Annadurai Purushothaman³, and Palaniappan Elango^{*1}

¹ Department of Physics, Government Arts College, Coimbatore 641018, India

² Department of Physics, Sree Sakthi Engineering College, Coimbatore 641104, India

³ Department of ECE, Sree Sakthi Engineering College, Coimbatore 641104, India

Received 13 January 2017, revised 23 April 2017, accepted 2 May 2017

Published online 30 May 2017

Keywords automated nebulizer spray pyrolysis, FESEM study, UV study and gas sensing behavior, XRD study

* Corresponding author: email yuvagopal@yahoo.in, Phone: +914222215212; +918056455006, Fax: +914222217572

Automated nebulizer-sprayed TiO₂ nanofilms were deposited on the glass substrate by using different temperature (300, 350, 400, 450, and 500 °C). The effect of temperature on the structural study by XRD and AFM reveals that the amorphous nature turns to stabilized anatase tetragonal phase with an enhancement of the preferred orientation (101), particle size, average roughness of the topographical view and thickness (238, 279, 304, 362, and 397 nm) of the coated films. The morphological study by the FESEM method shows a crack and a void free micro grain particle due to the effect of temperature.

An optical study shows that the transmittances of all the samples gradually decreased and the redshift of the absorption edges with decreased bandgap (3.67–3.35 eV) value is observed by the influence of temperature. The n-type semiconducting nature of TiO₂ nanofilms shows the voltage drop across the sensor element on exposure to the reducing gas. Among the various gases (CH₄O, C₃H₈O, NH₃, C₃H₆O) the reducing gas C₂H₆O exhibits a better response for a 500 °C coating temperature at an optimal operating temperature of 300 °C with a 150 ppm gas concentration.

© 2017 WILEY-VCH Verlag GmbH & Co. KGaA, Weinheim

1 Introduction Generally, an electronic nose (e-nose) is a sensor device that is used to sense the physical conditions of chemical compounds. The gas constituents were analyzed by using assorted methods but an e-nose detects the specific patterns or fingerprints of the gas mixture. The chemical sensor of the e-nose is most commonly used in conductivity sensors (metal oxide semiconductor, conducting polymer), piezoelectric sensors, MOSFET sensor, and optical sensors [1–3]. Among these, the conductivity sensor of a chemiresistor (metal oxide semiconductor) emphasizes the nature of surface sites and the surface reaction of gas, the electron-acceptor/donor properties of the gas, and adsorption and desorption of the gases. Currently, many researchers around the world are focused on studying the various metal oxide sensors (MOS). As is known, TiO₂ is considered as a prime candidate due to its numerous peculiar properties in diverse applications such as photochemical and photoconductive

devices in LEDs and gas discharge displays [3], transparent conductive electrodes for solar cells [4], microelectronics [5], and gas-sensing materials for gas-sensor devices [6].

Naturally, TiO₂ occurs in three polymorphic forms: anatase (D_{4h}, ¹⁹I₄/amd-symmetry, tetragonal), rutile (D_{4h}, ¹⁴P₄/mnm-symmetry, tetragonal), and brookite (P_{cab}-lower symmetry, orthorhombic). Among the three phases, the anatase is a metastable phase and has a bandgap (3.2 eV) higher than the others. The tetragonal anatase crystal structure is made up of a chain of distorted TiO₆ octahedra, which results in a unit cell containing four Ti atoms (at positions [0, 0, 0], [0, 1/2, 1/4], and [1/2, 0, 3/4]) and eight O atoms. Moreover, the anatase phase is the most suitable candidate for gas-sensor applications due to its biological and chemical inertness, strong oxidizing power, nontoxicity and long-term stabilization against photo- and chemical corrosion, and superior charge transport [7].

Stabilization of anatase phase has been shown to be very challenging in recent research. Since the effect of the temperature and the preparation method is one of the key features that ensures phase stability, the automated nebulizer spray pyrolysis is used to ensure the prolonged anatase phase. To our knowledge, only a few studies have been carried out using acetylacetone-stabilized Ti-alkoxide precursors, whereas the phase stability was not maintained in these studies [8–10]. In particular, no systematic study of structural and optical characterization of the anatase phase TiO₂ films deposited by a spray pyrolysis technique from the catalyst of acetylacetone stabilized Ti-isopropoxide has been performed. Predominantly, the automated nebulizer sprayed anatase phase stabilized and gas-sensing performances of TiO₂ film have not been studied so far. The aim of this work is to deposit the TiO₂ nanofilms on preheated glass substrate by using different temperature (300, 350, 400, 450, and 500 °C) through automated nebulizer spray pyrolysis and exemplify the structural, optical, topography, morphological, and gas-sensing performance of the TiO₂ nanofilms.

2 Experimental

2.1 Materials deposition TiO₂ nanofilms were prepared by using an automated nebulizer spray pyrolysis technique (ANSP) with various temperatures (300, 350, 400, 450, and 500 °C) in an air atmosphere. The experimental setup, procedure and advantages of ANSP were explained [11, 12] elsewhere and Fig. 1 with optimized parameters are mentioned in Table 1. The primary stock solution was prepared with 0.1 mol l⁻¹ of titanium tetra-isopropoxide (TTIP) [Ti[OCH(CH₃)₂]₄] dissolved in 50 ml of a mixed solution of ethanol (EtOH) (C₂H₆O) solvent with acetylacetone (AcAc)

Table 1 Optimized spray parameter for TiO₂ nanofilms.

particulars	parameter
spray type	nebulizer
air blast	atomizer
carrier gas pressure	30 Pa
solution flow rate	0.10 ml min ⁻¹
distance from substrate to spray nozzle	5 cm
substrate type	glass
solvent	ethanol and acetyl acetone
precursor	titanium isopropoxide
concentration	0.1 mol l ⁻¹
deposition temperature	300, 350, 400, 450, and 500 °C

[CH₃COCH₂COCH₃] stabilizer in the ratio of (4:1), stirred for 15 min by using a magnetic stirrer, and finally turns into a pale yellow transparent solution. The obtained transparent pale yellow solution was poured into nebulizer container and sprayed on the ultrasonically cleaned glass substrate at various temperatures.

2.2 Characterization techniques The effect of temperature and their characterization were analyzed by the following means. The structural, compositional properties of TiO₂ films were entirely studied by X-ray diffraction (Bruker D8 advance X-ray diffractometer) with Cu K_α radiation ($\lambda = 0.15418$ nm) and X-ray photoelectron spectroscope (XPS). The study of surface morphology was characterized via an atomic force microscope (AFM, Model-Nanoscope E) and a field emission scanning electron microscope (FESEM, Quanta-250 FEG) applying an

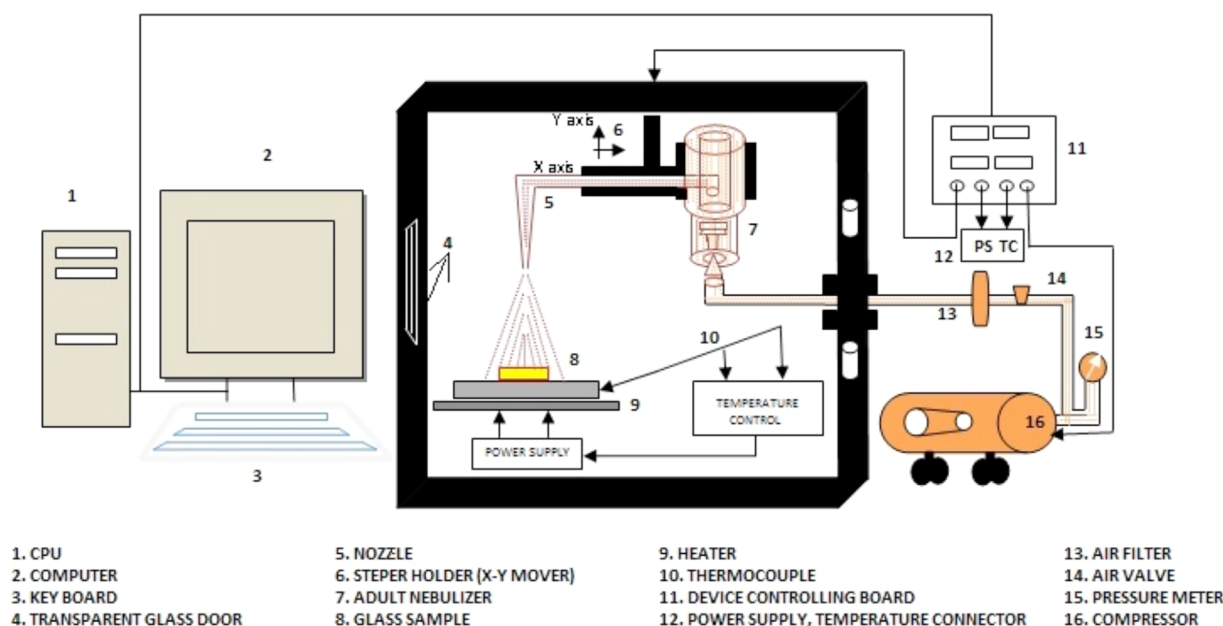


Figure 1 Schematic diagram of automated spray pyrolysis system.

operating voltage of 30.0 kV. An optical study of the films was done by an ultraviolet-visible-near-infrared (UV-Vis-NIR) spectrophotometer (Model JASCO-V-500) in the range from 250 to 970 nm, and the thicknesses of the films were determined by using surface profilometer (SJ-301 Mitutoyo). Finally, the gas-sensing performances were studied by the method of two probes with an LCR meter (GW Instek LCR – 821).

2.3 Gas-sensing measurements The schematic diagram of the gas-sensor setup is shown in Fig. 2. As can be seen, the cylindrical stainless steel testing chamber inbuilt with a nichrome-heating element and a chromel-alumel thermocouple is fixed at the bottom of the testing chamber and it is well connected with a temperature controller for adjusting the temperature (~up to 500 °C). The sensing measurements were proceeded by a static process: a specified amount of the test gas such as C₂H₆O, NH₃, CH₄O, C₃H₈O, and C₃H₆O was injected into a testing chamber and mixed with air. A mass flow controller (MFCs) was used to control the concentration of the test gases. The sensor films were electrically connected to a two-probe setup for measurement of the resistance variation (GW Instek LCR – 821) and hence, the sensing response was calculated. The gas sensitivity response (*S*) factor of TiO₂ nanofilms was calculated by using the relation of resistance in the air (*R*_{air}) and resistance in reducing gases (*R*_{gas}), which was expressed as [13]:

$$S = \frac{R_{\text{air}} - R_{\text{gas}}}{R_{\text{gas}}} = \frac{\Delta R}{R_{\text{gas}}} \sim \frac{R_{\text{air}}}{R_{\text{gas}}}. \quad (1)$$

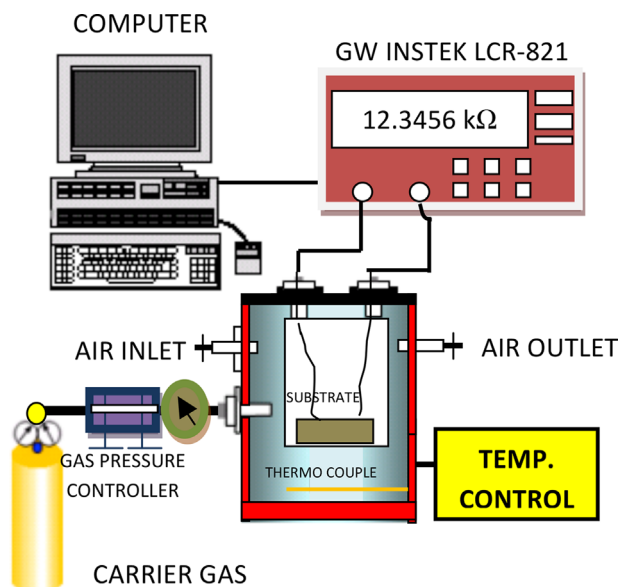


Figure 2 Schematic diagram of gas sensor setup.

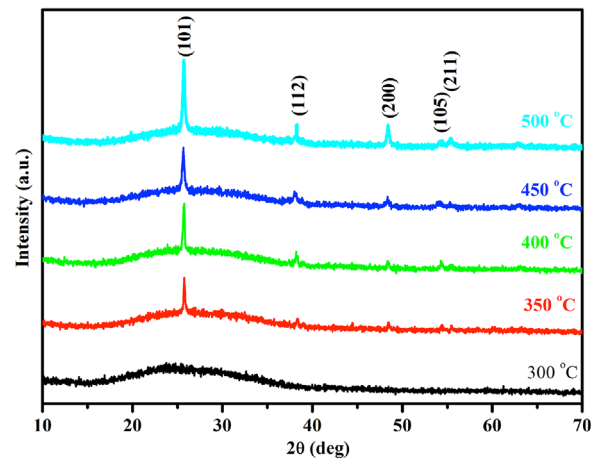


Figure 3 XRD patterns for TiO₂ thin films.

3 Results and discussion The XRD (X-ray diffraction) patterns of TiO₂ films at different temperatures are shown in Fig. 3. The obtained diffraction patterns show a predominant diffraction peak at 25.35° that can be assigned to the (101) plane of anatase TiO₂ is found to begin at approximately 350 °C. At 500 °C, a very sharp exothermic peak ($2\theta = 25.39, 38.62, 48.19, 54.22, \text{ and } 55.14^\circ$) is observed in the XRD pattern and all corresponding reflected planes (101), (112), (200), (105), and (211) were well fitted with a standard JCPDS data, card no. 89-4921. The film at 300 °C depicts an amorphous nature. This is caused by the improving crystallinity of the films. The grain size “*D*” is calculated using the Scherrer formula [14],

$$D = \frac{0.9 \times \lambda}{(\beta \times \cos\theta)} \quad (2)$$

$$d = \frac{n\lambda}{(2\sin\theta)}, \quad (3)$$

where *D* is the particle size, λ is the wavelength of the X-rays, β is the broadening of the diffraction line measured at half its maximum intensity in radians, *d* is the interplanar spacing value, and θ is the angle of diffraction. The obtained grain sizes of the films were increased with increasing temperature from 350 to 500 °C. This trend was confirmed by many authors [15, 16]. The lattice constants determined from the present data are $a = 3.791 \text{ \AA}$ and $c = 9.503 \text{ \AA}$. The dislocation density and microstrain were calculated by using Eqs. (4) and (5) for TiO₂ films [11].

$$\delta = \frac{1}{D^2} \quad (4)$$

$$\varepsilon = \frac{\lambda}{D \sin\theta} - \frac{\beta}{\tan\theta}. \quad (5)$$

Table 2 Obtained values of structural parameters, average roughness and coating thickness of the TiO₂ films.

temp (°C)	peak position 2θ (deg)	FWHM value (deg)	<i>(h, k, l)</i> value			“D” particle size (nm)	“δ” dislocation ×10 ¹⁴ (linmet ⁻²)	“ε” strain ×10 ⁴ (lin ⁻² met ⁴)	“d spacing” value ×10 ⁻¹⁰ m	stacking fault	average roughness (nm)	thickness (nm)
			<i>h</i>	<i>k</i>	<i>l</i>							
300			amorphous nature								0.062	238
350	25.3582	0.1673	1	0	1	50.88	3.863	7.122	3.512	0.089	1.481	279
	38.6382	0.2007	1	1	2	43.85	5.202	8.264	2.330	0.086		
	48.1888	0.2676	2	0	0	33.99	8.654	10.659	1.888	0.101		
400	25.3106	0.2004	1	0	1	42.47	5.544	8.532	3.519	0.107	1.933	304
	38.6386	0.1673	1	1	2	52.60	3.615	6.889	2.330	0.071		
	48.1192	0.2676	2	0	0	33.98	8.658	10.662	1.891	0.101		
450	25.3445	0.1337	1	0	1	63.66	2.467	5.692	3.514	0.071	2.269	362
	38.6546	0.2015	1	1	2	43.67	5.243	8.297	2.329	0.086		
	48.1851	0.2676	2	0	0	33.99	8.654	10.659	1.889	0.101		
500	25.3715	0.1171	1	0	1	72.69	1.893	4.985	3.511	0.062	2.815	397
	38.6440	0.4015	1	1	2	21.92	20.817	16.532	2.330	0.172		
	48.1296	0.1673	2	0	0	54.36	3.384	6.665	1.891	0.063		

The calculated values are given in Table 2. It is clear that when the coating temperature is increased, the strain of the coated films increased considerably. This type of micro-strain changes may be due to the predominant recrystallization process in the polycrystalline thin films.

XPS (X-ray photoemission spectroscopy) is a straightforward and nondestructive technique for the investigation of the chemical and electronic structure of materials. An important advantage of XPS is its ability to characterize the variation in the binding energies of the core level or chemical shifts of the samples. Figure 4a shows the broad emission spectrum of TiO₂ thin films in the binding energy range 0–1300 eV. Only three elements are detected on the surface of the film, titanium, oxygen and also some carbon, showing the photoelectron peaks Ti 3p, Ti 3s, Ti 2p, Ti 2s for titanium, O 1s, O 2s for oxygen, and C 1s for carbon. The high-resolution scanning images at 500 °C of TiO₂ are shown in Fig. 4b–e. In that order, separate analysis elements of core levels C 1s, O 1s, and Ti 2p_{3/2}, Ti 2p_{1/2} indicated the binding energies at 286.14 eV, 530.90 eV and 458.43 eV, 465.24 eV, respectively. These calculations led to the conclusion that these titania anatase phase thin films have 7.65% of carbon, 45.16% of oxygen, 46.93% of Ti⁴⁺ and the presence of this prime element and carbon is probably due to the use of organic precursors and the contamination caused by sample handling [17]. The standard anatase titania (Ti⁴⁺) phase was well fitted with the prepared film of TiO₂ [18].

The topographical view of a 2 × 2 μm² sized three-dimensional AFM image of TiO₂ thin films using different temperatures (300, 350, 400, 450, and 500 °C) is presented in Fig. 5a–e. In the sample with the lowest temperature (300,

350, and 400 °C), the particles are rather isolated from each other (Fig. 5a–c), while those in Fig. 5d and e are widely distributed. These changes in the surface morphology might lead to a reduced crystalline quality of the films [19]. This suggests that the particles seen at the surface of the film are clusters of crystallites. The calculated values of AFM roughness parameters are listed in Table 2. This shows that the coating temperature increased with increase in the root mean square surface roughness and the coating thickness of the films, which shows the fine correspondence with XRD study of the average crystalline size and intensity. The influence of thickness significantly plays a role to control the film properties and phase stability; which is one of the important parameters to achieve the desired structural and functional properties [20]. Optical profilometer (SJ – 301 Mitutoyo) Alpha-step instruments were used to measure the coating thickness of TiO₂. The novel nebulizer spray pyrolysis method provides a uniform coating over a wide area [9] hence, the prepared films thicknesses are in the range of 238–397 nm.

The field emission scanning electron microscope (FESEM) is used to examine the morphological features such as grain morphology, thickness, grain-size distribution, and grain size of the films. The irregular granular shape of the agglomerated grain particles with dispersed large voids appeared at 300 °C (Fig. 5f) and close-packed (without pinholes) granular particles appeared at 350 °C (Fig. 5g). The cluster-like domain structure increased on increasing the coating temperature with cracks, void-free micrograin particles being revealed at 400, 450, and 500 °C.

As can be seen, the higher coating temperature can create the crystal quality and uniformity of the nanofilms,

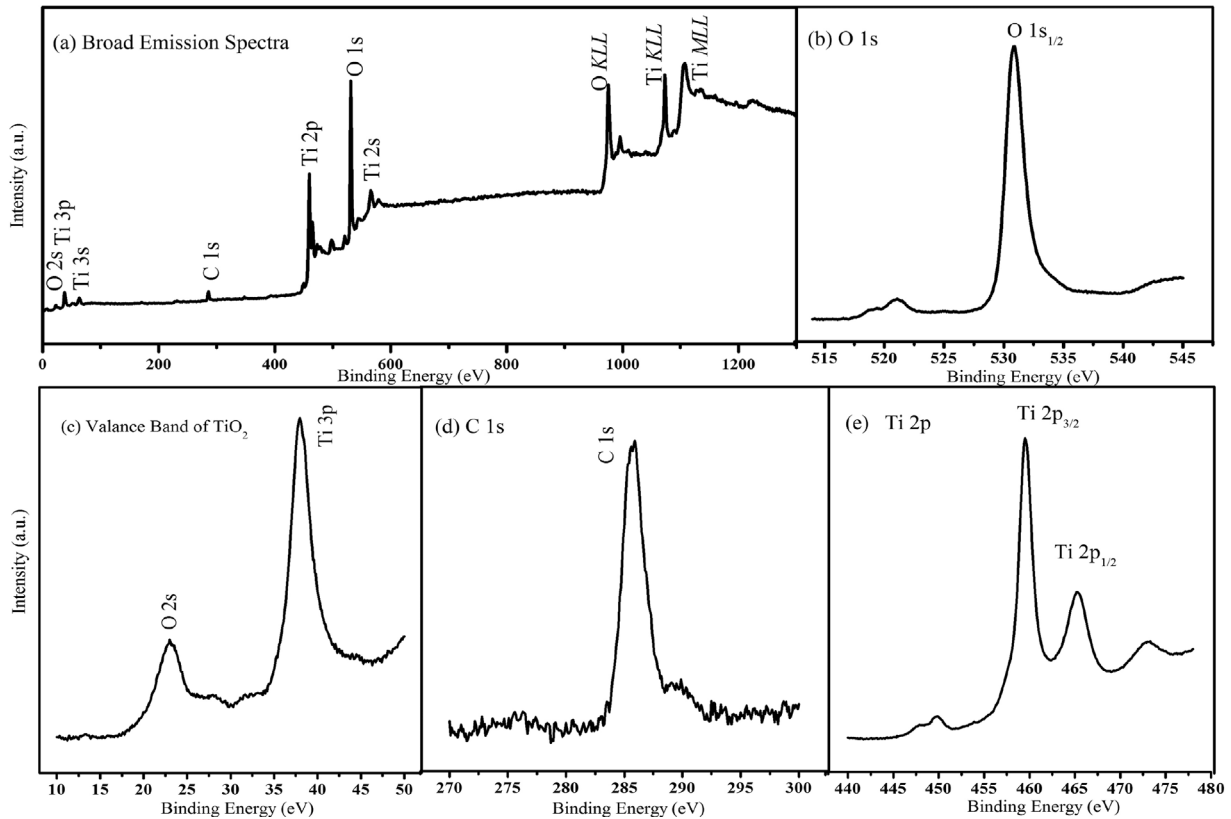


Figure 4 Survey scan XPS analysis of ($T = 500^\circ\text{C}$) TiO_2 films on narrow and broad emission spectra.

which is in good agreement with the structural (XRD) and topography (AFM) study.

Optical transmittance spectra of TiO_2 films were measured in the wavelength range from 250 to 980 nm. Figure 6 shows the oscillating nature transmittance curves of TiO_2 films of different temperature (300, 350, 400, 450, and 500°C) and the observed oscillating nature of the transmittance is due to the interference effect from the reflection at the coated films and substrates [21]. The maximum transmittance value of 102.9% (at $\lambda = 612$ nm) at 300°C is shown in the figure, and the transmittance of all the films was decreased with increasing temperature, due to an increase in film thickness and an increase in the scattering of photons by crystal defects [22]. The calculated thickness of the coated films has been explained with the help of the following relation,

$$I = I_0 e^{-\alpha d}, \quad (6)$$

where α is the absorption coefficient and d is the films thickness. The optical absorption coefficient (α) is calculated by using [23],

$$\alpha = \frac{1}{d} \ln\left(\frac{1}{T}\right), \quad (7)$$

where T is the transmittance and d is the thickness of film. Likewise, the UV region of sharp absorption edges reveals that the redshift is due to the temperature and thickness (238, 279, 304, 362, and 397 nm). The improvement in crystal quality of the films along with a reduction in porosity [24] and their structural change is revealed by XRD measurement. For the allowed direct transition, the variation of α with photon energy ($h\nu$) obeys Tauc's plot [23],

$$(\alpha h\nu)^2 = A(h\nu - E_g), \quad (8)$$

where E_g is the optical bandgap, h is Planck's constant, α is the absorption coefficient, and A is a constant having values between 1×10^5 and $1 \times 10^6 \text{ cm}^{-1} \text{ eV}^{-1}$ [25]. Figure 7 shows the Tauc plot as a function of temperature in TiO_2 films. The obtained bandgap values increased from 3.22 to 3.65 eV with a decrease in the temperature. The increase in the optical bandgap with decrease in film temperature is due to the variation in lattice defects and stress [26, 27].

4 Gas-sensing behavior of TiO_2 nanofilms The sensor element of TiO_2 nanofilms exhibit typical n-type semiconducting behavior, as there is a voltage drop across the sensor element on exposure to the reducing gas. Accordingly, the gas-sensing response of TiO_2 chemiresistors (metal oxide) with different coating temperature (300, 350, 400, 450, and 500°C) toward various gases like

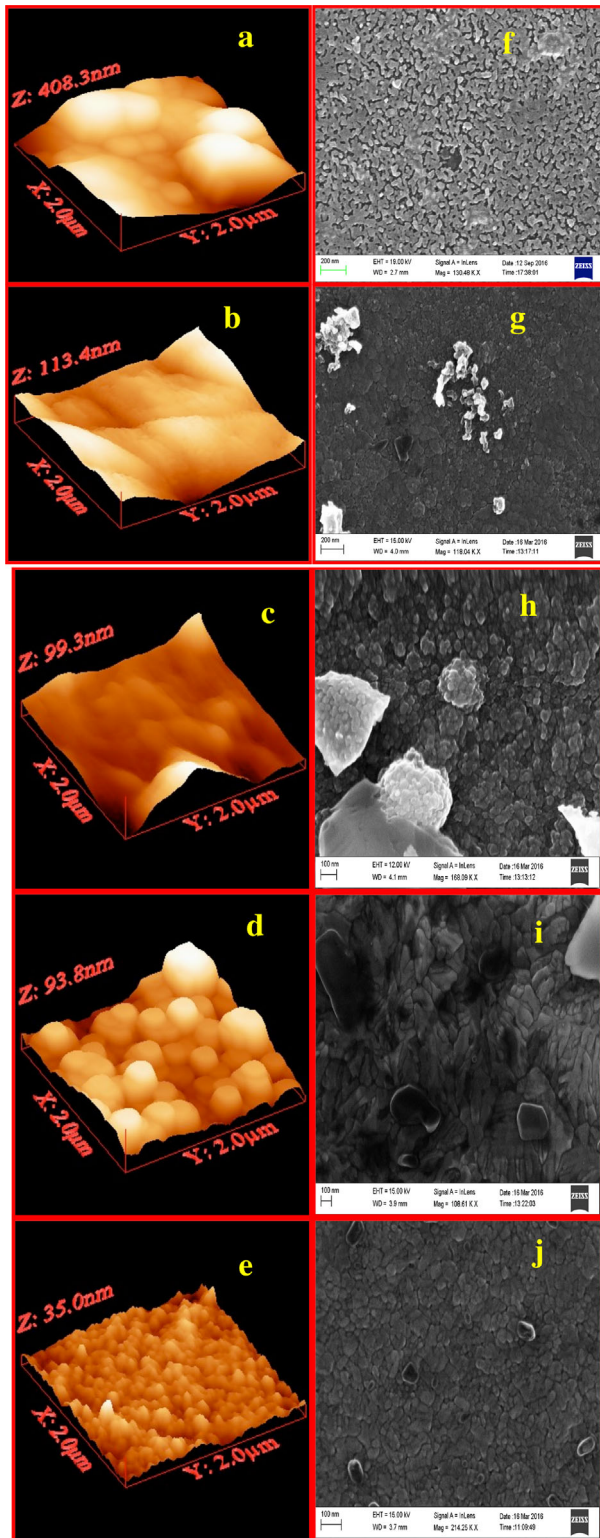


Figure 5 (a–e) Topography view of AFM and (f–j) and surface morphology of FESEM for TiO₂ thin films ($T = 300, 350, 400, 450,$ and $500\text{ }^{\circ}\text{C}$).

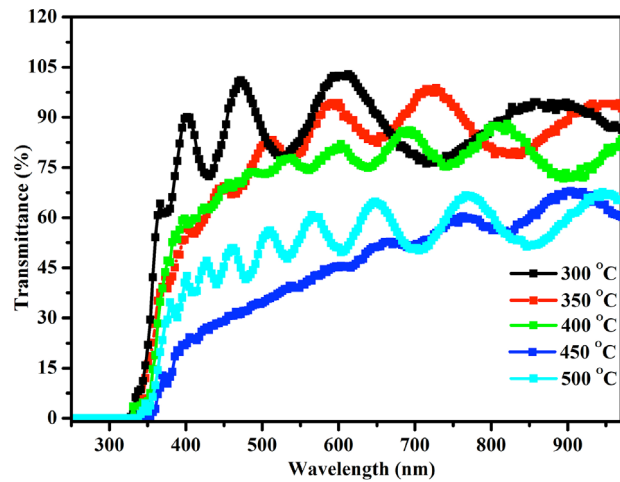


Figure 6 Optical transmittance spectra of TiO₂ films at various temperatures.

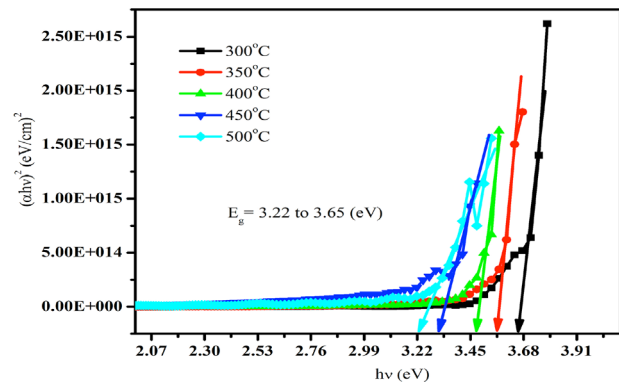


Figure 7 Plot of $(\alpha hv)^2$ vs. hv for TiO₂ films sprayed using various temperatures.

methanol (CH₄O), ammonia (NH₃), isopropyl alcohol (C₃H₈O), ethanol (C₂H₆O), and acetone (C₃H₆O) reducing gas as a function of constant temperature (300 °C) and gas concentration (150 ppm) is presented in the bar chart selectivity graph of Fig. 8a. Here, the gas-sensing characteristics indicate that the sensor element exhibits the maximum sensing response to C₂H₆O reducing gas and a minimum sensing response to C₃H₈O reducing gas.

The effect of temperature on TiO₂ nanofilms when exposed to C₂H₆O reducing gas at 150 ppm constant gas concentration is presented in Fig. 8b. Hence, the various coating temperatures (300, 350, 400, 450, and 500 °C) of the sensor elements reveal the adsorption and desorption in the gas sensor by using different operating temperatures, because the sensitivity of the response increased with increasing temperature up to 300 °C, and then decreased with increasing temperature. This is due to the activation energy at a particular temperature (300 °C) being high enough to complete the chemical reaction and this temperature is called the optimal temperature. Hence, coating temperature of 500 °C exhibits the greatest possible

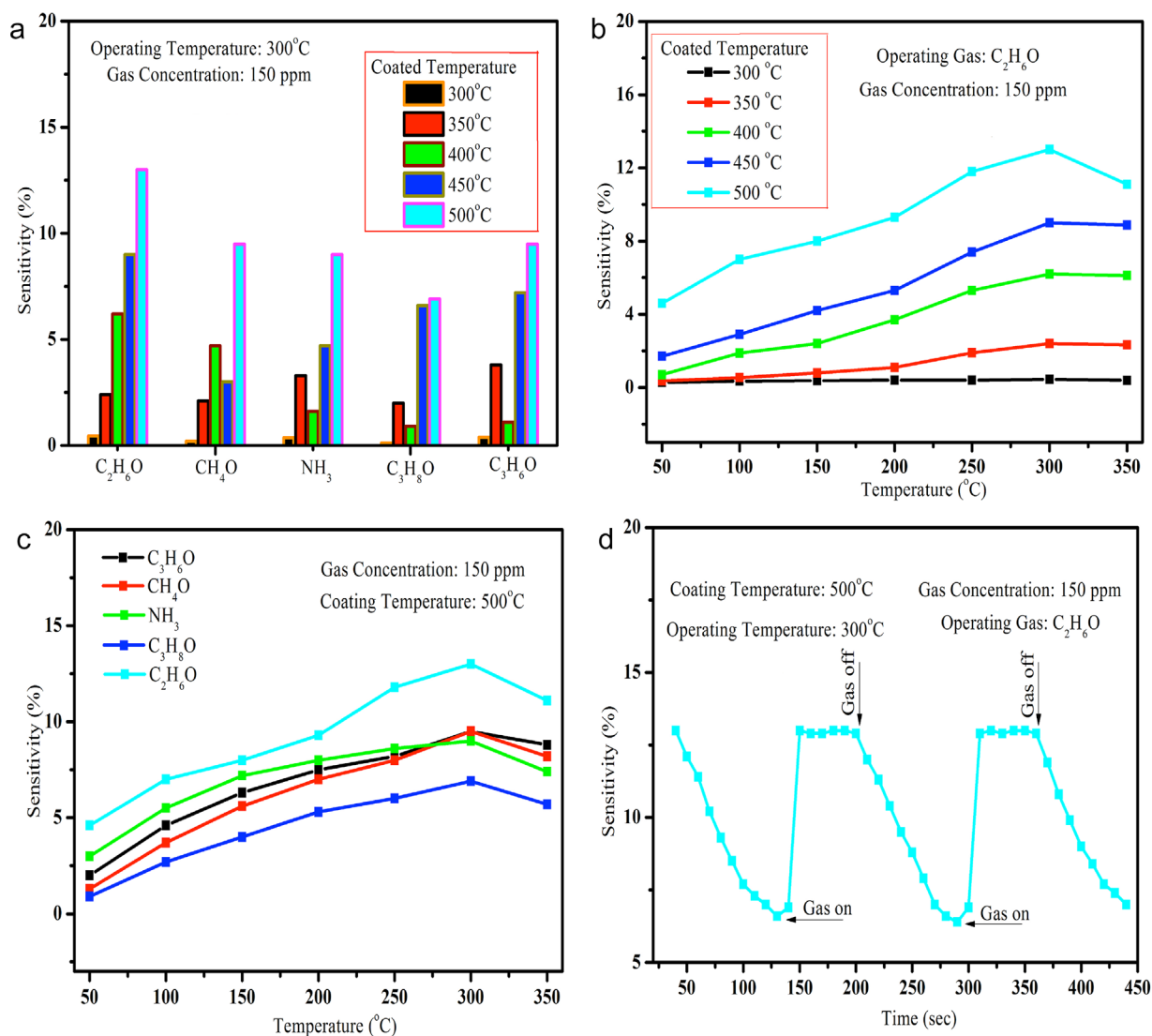
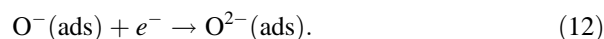
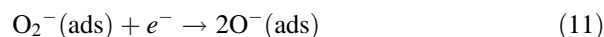
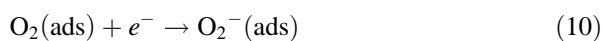


Figure 8 (a) Sensitivity of various reducing gases with constant temperature (300 °C) and concentration (150 ppm); (b) sensitivity of ethanol reducing gas at constant gas concentration (150 ppm) as a function of temperature; (c) sensitivity of various reducing gas with different operating temperature on 500 °C coated film; (d) response and recovery time of TiO₂ nanofilms.

detection to C₂H₆O reducing gas as a function of operating temperature.

The sensitivity of a chemiresistor (metal oxide) sensor is examined by the interaction of the target gas and the sensor surface. The surface-controlled process is responsible for the gas sensitivity of the metal oxide [28]. It is well known that the surfaces of metal oxides enable absorption of the oxygen species of O₂⁻, O⁻, or O²⁻ from the surroundings, which also control the increment of conductivity due to electron capture by the oxidizing gas at various operating temperature [29, 30] as follows,

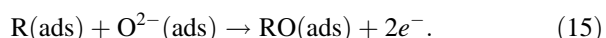
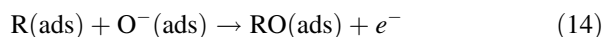


Oxygen may be either physisorbed as uncharged molecules (9) or chemisorbed as charged species (10–12) on the n-type semiconducting oxide surface. The physisorbed oxygen will not affect the surface states, whereas the chemisorbed oxygen species act as surface acceptors and capture the electrons from the conduction band of materials. The change of resistance is dependent on the species and chemisorbed oxygen on the surface. The surface of a TiO₂ sensor can adsorb oxygen because of the electron depletion, and the resistance of the sensor increases. The reducing

gases (R) may be adsorbed on the surface of the sensor materials according to:



The reaction between the adsorbed gases and the adsorbed oxygen species, for example, $O^-(\text{ads})$ and $O^{2-}(\text{ads})$, will then proceed as follows:



The reducing gas (R) readily reacts with the surface chemisorbed oxygen and thereby releases electrons back to the conduction band of TiO_2 , leading to a decrease in the electrical resistance of the semiconductor metal-oxide material (TiO_2). This change of the electrical resistance determines the response of TiO_2 -based sensor to reducing gases. Finally, desorption of the resulting product will take place as:



An enhanced response would be expected if a sufficient amount of target gas is adsorbed and subsequently the reaction between the adsorbed reducing gas and the oxygen species is more favorable. The gas response is directly related to the adsorbed oxygen species on the surface of the sensing layer. At higher operating temperature ($>300^\circ\text{C}$), adsorbed oxygen starts to desorb. Desorption would thus reduce the oxygen species from the surface, which in turn decreases the gas response. Thus, there exists the optimum operating temperature (300°C) at which the gas response is higher to the sensor element of TiO_2 .

Various gas-sensing responses to different gases may be due to differences in the adsorption and the reaction processes. The response of TiO_2 toward various tested reducing gases as a function of operating temperature is exhibited in Fig. 8c. From this figure, we may conclude that a sensor element based on a 500°C coating temperature could detect well and has a poor selectivity of C_2H_6O and C_3H_8O reducing gas respectively. When a surface of the material is exposed to the reducing gas, the interaction with the chemisorbed oxygen can take place in various ways. Here, the maximum sensitivity of surface reactions can be written to C_2H_6O reducing gas as follows [31]:



The dynamic response for ethanol reducing gas at 300°C of optimal temperature with 150 ppm of gas concentration ($S_{\text{max}} = 12.91\%$ for 500°C) is shown in Fig. 8d. The response (τ_{res}) and recovery (τ_{rec}) times are defined as the time it takes to decrease the maximum

resistance of 90% ($R_g - R_f$) up on exposure to the target gas and then to recover the maximum resistance back to 30% when the reference gas is restored [32]. The evaluated average response (~ 10 s) and recovery time (~ 80 s) is noted, respectively. In summary, all the coated films exhibit a relatively small response to ethanol (C_2H_6O) reducing gas against others (CH_4O , C_3H_8O , NH_3 , C_3H_6O) at 300°C with 150 ppm gas concentration. The sensitivity percentage increased with increase in the coating temperature with respect to constant ethanol concentration (150 ppm), which is due to the observable fact of receptor function (surface phenomenon) [33] and their coated thickness [34].

5 Conclusions This study investigated the synthesis of titanium dioxide (TiO_2) anatase phase nanosized crystallites and high surface areas of the films by using an automated nebulizer spray pyrolysis method. The structural study by XRD shows that the amorphous nature turns to anatase phase with better plane orientation (101) and particle size. The compositional analysis of XPS confirms Ti^{4+} in the pure anatase phase and the topographical view (AFM) of roughness and coated thickness were enhanced on increasing the temperature. FESEM shows the agglomerated grains were changed to void-free micrograin particles and the optical study shows the decremented transmittance and redshift of absorption edges with reduced bandgap (3.67–3.35 eV). The optimal temperature of 300°C at 150 ppm of ethanol reducing gas shows the better response of the 500°C coated films among the others (300, 350, 400, and 450°C).

Acknowledgements One of the authors (V. Gopala Krishnan) gratefully acknowledges Dr. T. Shripathi, Dr. U. P. Deshpande, and Er. Mohan Gangrade from the UGC – DAE CSR, Indore center, Khandwa Road, India for their scientific advice and for providing the necessary laboratory facilities to carry out this investigation.

References

- [1] K. Madhusudan Reddy, L. Satyanarayana, S. V. Manorama, and R. D. K. Misra, *Mater. Res. Bull.* **39**, 1491–1498 (2004).
- [2] M. Sugimoto, *J. Am. Ceram. Soc.* **82**, 269–280 (1999).
- [3] B. Bharti, S. Kumar, H.-N. Lee, and R. Kumar, *Sci. Rep.* **6**, 32355 (2016).
- [4] I. Vaiciulis, M. Girtan, A. Stanculescu, L. Leontie, F. Habelhames, and S. Antohe, *Proc. Rom. Acad. Seri. A* **13**(4), 335–342 (2012).
- [5] G. P. Burns, *J. Appl. Phys.* **65**, 2095–2097 (1989).
- [6] H. Tang, K. Prasad, R. Sanjinés, and F. Lévy, *Sens. Actuators B: Chem.* **26–27**, 71–75 (1995).
- [7] M. Epifani, A. Helwig, J. Arbiol, R. Díaz, L. Francioso, P. Siciliano, G. Mueller, and J. R. Morante, *Sens. Actuators B: Chem.* **130**, 599–608 (2008).
- [8] A. Oja, M. Mere, M. Krunk, R. Nisumaa, C.-H. Solterbeck, and M. Es-Souni, *Thin Solid Films* **515**, 674–677 (2006).
- [9] F. D. Duminica, F. Maury, and S. Abisset, *Thin Solid Films* **515**, 7732–7739 (2007).
- [10] H. Zabova and V. Cirkva, *J. Chem. Technol. Biotechnol.* **84**, 1624–1630 (2009).

- [11] V. Gopala Krishnan, P. Elango, V. Ganesan, and P. Sathish, *Optik* **127**, 11102–11110 (2016).
- [12] V. Gopala Krishnan, P. Elango, M. Ragavendar, P. Sathish, and G. Gowrisankar, *Mater. Res. Express* **4**(036401), 1–10 (2017).
- [13] A. A. Haidrya, J. Puskelova, T. Plecenik, P. Durina, J. Gregus, M. Truchly, T. Roch, M. Zahoran, M. Vargova, P. Kus, A. Plecenik, and G. Plesch, *Appl. Surf. Sci.* **259**, 270–275 (2012).
- [14] B. D. Cullity, *Elements of X-Ray Diffraction* (2nd edition) (Addison-Wesley Publishing Company, Inc., Reading, Massachusetts – Menlo Park, California London – Amsterdam – Don Mills, Ontario – Sydney, 1978).
- [15] Ya-Qi Hou, Da-Ming Zhuang, G. Zhang, M. Zhao, and M.-S. Wu, *Appl. Surf. Sci.* **218**, 98–106 (2003).
- [16] J. YuU, X. Zhao, and Q. Zhao, *Thin Solid Films* **379**, 7–14 (2000).
- [17] R. Ayouchi, C. Casteleiro, R. Schwarz, J. R. Barrado, and F. Martín, *Phys. Status Solidi C* **7**(No. 3–4), 933–936 (2010).
- [18] S. K. Joung, T. Amemiya, M. Murabayashi, and K. Itoh, *Chem. Eur. J.* **12**, 5526–5534 (2006).
- [19] M. A. Martynez, C. Guillen, and J. Herrero, *J. Appl. Surf. Sci.* **136**, 8–16 (1998).
- [20] Y. S. Lim, J. S. Jeong, J. Bang, and J. Kim, *Solid State Commun.* **150**, 428–430 (2010).
- [21] M. P. Bole and D. S. Patil, *J. Phys. Chem. Solids* **70**, 466–471 (2009).
- [22] H. Bensouyad, D. Adnane, and H. Dehdouh, *J. Sol Gel Sci. Technol.* **59**(3), 546–552 (2011).
- [23] A. E. Jimenez-Gonzalez, J. A. S. Urueta, and R. Suárez-Parra, *J. Cryst. Growth* **192**, 430–438 (1998).
- [24] N. M. Ganesan, T. S. Senthil, N. Muthukumarasamy, and R. Balasundaraprabhu, *Int. J. ChemTech Res.* **6**(5), 3078–3082 (2014).
- [25] E. A. Davis and N. F. Mott, *Philos. Mag.* **22**, 903–922 (1970).
- [26] Y. C. Lin, B. L. Wang, W. T. Yen, C. T. Ha, and C. Peng, *Thin Solid Films* **518**, 4928–4934 (2010).
- [27] R. Ghosh, D. Basak, and S. Fujihara, *J. Appl. Phys.* **96**, 2689–2692 (2004).
- [28] F. Chu, X. Q. Liu, and G. Y. Meng, *Mater. Sci. Eng. B* **64**, 60–63 (1999).
- [29] A. A. Haidrya, J. Puskelova, T. Plecenik, P. Durina, J. Gregus, M. Truchly, T. Roch, M. Zahoran, M. Vargova, P. Kus, A. Plecenik, and G. Plesch, *Appl. Surf. Sci.* **259**, 270–275 (2012).
- [30] K. Zakrzewska, *Titanium Dioxide Thin Films for Gas Sensors and Photonic Applications* (AGH Ucelniane Wydawnictwa Naukowo-Dydaktyczne, Krakow, 2003).
- [31] M. R. Vaezi and S. K. Sadrezaad, *Mater. Sci. Eng., B* **140**, 73–80 (2007).
- [32] Y. Li and W. Wlodarski, *Sens Actuators B Chem.* **83**, 160–163 (2002).
- [33] S. Shukla and S. Seal, *Encyclopedia of Nanoscience and Nanotechnology* (Stevenson Ranc, American Scientific Publishers, CA, 2003).
- [34] V. Y. Young, F. C. Chang, and K. L. Cheng, *Appl. Spectrosc.* **1**(1), 994–1000 (1987).